VLF IMAGING OF LIGHTNING-INDUCED IONOSPHERIC DISTURBANCES

A DISSERTATION

SUBMITTED TO THE DEPARTMENT OF ELECTRICAL ENGINEERING

AND THE COMMITTEE ON GRADUATE STUDIES

OF STANFORD UNIVERSITY

IN PARTIAL FULFILLMENT OF THE REQUIREMENTS

FOR THE DEGREE OF

DOCTOR OF PHILOSOPHY

Michael Paul Johnson

September 2000

I certify that I have read this dissertation and that in my opinion it is fully adequate, in scope and quality, as a dissertation for the degree of Doctor of Philosophy.

_____

Umran S. Inan
(Principal Advisor)

I certify that I have read this dissertation and that in my opinion it is fully adequate, in scope and quality, as a dissertation for the degree of Doctor of Philosophy.

_____

Timothy F. Bell

I certify that I have read this dissertation and that in my opinion it is fully adequate, in scope and quality, as a dissertation for the degree of Doctor of Philosophy.

_____

Dwight G. Nishimura

Approved for the University Committee on Graduate Studies:

_____

To my mother, father, and brother

Linda Mele, Robert Paul, and James Allen Johnson

and my wife

Rachel Stewart Johnson

Abstract

Very Low Frequency (VLF) probing has recently emerged as a powerful tool for remote sensing of transient D region ionospheric disturbances. During nighttime, when relatively low electron densities make the D region inaccessible to probing with radar and ionosonds, VLF transmitter signals propagating in the Earth-ionosphere waveguide are sensitive even to slight (10%) conductivity changes at $\sim$85 km altitudes. Past studies have revealed VLF signal perturbations associated with some lightning discharges, indicating both direct and indirect energetic coupling mechanisms between the troposphere and ionosphere. However, the assessment of the geophysical and global significance of these processes requires the determination of their spatial distribution and frequency of occurrence. A new VLF receiver system has been designed for this goal, incorporating PC based real-time DSP, GPS timing, Internet remote control, and automated data transfer. The Holographic Array for Ionospheric/Lightning research (HAIL) consists of nine of these receivers deployed in the Midwest and operating year-around. Resulting multi-station data from the HAIL array has shed light on both types of coupling interactions.

"Early/fast" VLF signal perturbations, so called because they occur immediately after a lightning discharge ($<$20 ms delay, i.e., "early") and exhibit a rapid onset ($<$20 ms, i.e., "fast"), are associated with ionospheric disturbances located above the causative lightning discharge. These direct-coupling disturbances are observed with forward scattering patterns which exhibit 15 dB beamwidths of less than 30°, shown to be consistent with horizontal extents of 90$\pm$30 km when compared with a three-dimensional model of VLF wave propagation. However, early/fast VLF events are

found to be only observed in association with a small fraction of the frequent lightning discharges in North America. In terms of the global significance of this phenomenon, observations now show that only those lightning discharges with an unusually long duration intracloud component are associated with the direct coupling events.

Lightning-Induced Electron Precipitation (LEP) VLF events are known to be caused by an indirect lightning-ionosphere interaction. A fraction of the energy radiated by a lightning discharge escapes into the magnetosphere and propagates as a whistler-mode wave where it changes the pitch angle of trapped radiation belt electrons, causing those close to the loss cone to precipitate into the lower ionosphere. These high energy electrons cause secondary ionization, modifying the ionospheric conductivity which in turn is manifested as amplitude and phase perturbations in subionospheric VLF signals. Previous work on the LEP phenomena has mostly emphasized interactions with ducted whistler waves, which are constrained to propagate in field-aligned ducts of enhanced ionization in the magnetosphere. The first two-dimensional images of these indirect conductivity disturbances, however, now show that the LEP phenomenon does occur under more general conditions, without the existence of magnetospheric ducts. Concerning several predictions of a recent theoretical study of electron precipitation caused by obliquely propagating (nonducted) whistlers, spatial size, location, and intensity of precipitation, are here shown to be quantitatively consistent with empirical observations with the HAIL array in conjunction with two-dimensional earth ionosphere propagation modeling. Results suggest that the lightning-induced electron precipitation process is likely to be an important contributor to the loss of radiation belt electrons on a global scale, since oblique whistler waves are naturally excited under a broad range of magnetospheric conditions, and continuously populate large regions of the magnetosphere.

Acknowledgements

I would like to begin with thanks to my advisor, Umran Inan, for his inspiring enthusiasm in leading the VLF group. I appreciate the time that he has spent assisting with the development of this experiment, and have enjoyed the many rich discussions that we have had regarding the analysis and interpretation of the results. I would also like to extend my gratitude to my associate advisor Tim Bell. Tim has always been very approachable, and he is happy to discuss any topic from VLF engineering to wilderness adventures. I have also been very fortunate as a member of the VLF group to work with esteemed scholars Robert Helliwell, Don Carpenter, and Martin Walt, and I am grateful for their frequent words of wisdom and encouragement. I would like to thank Professor James Gibbons for being the chairman of my defense committee, and Professor Dwight Nishimura who was on both my defense and reading committees.

The work presented in this thesis could not have been completed without the help of the teachers and staff at the high schools and colleges that graciously hosted our experiment. Although our deployment was often during the summers when classes were not in session, these people greeted me enthusiastically and often helped in the installation and management of our instruments. Their eagerness to learn about this research effort and to involve their students in active participation was inspirational, and subsequently led to my giving a number of talks to students and proudly learning of several student science projects that used data from our experiment.

I would like to thank Shaolan Min for her administrative help (particularly during the busy construction phase of the experiment), her friendly greetings, and her

and 4.

My time at Stanford was also greatly enriched by the friendships that I developed with other Stanford students. I shared an apartment with Travis Bryson my first year on campus and found him to not only be an ideal roommate, but a great friend as well. In that first year, we met Peter Catrysse (also a new engineering graduate student), who began the slow process of teaching us about fine European culture. We met our multi-talented friend Rob Batchko soon thereafter, and have all enjoyed many entertaining barbecues together. Peter, Travis, and I later moved to "The Ranch" in Woodside with another friend, Gena Imeshev. There we continued our tradition with some all-out historic barbecue events, most notably The Beast '98.

During a summer internship after my junior undergraduate year, I met Albert Jerng, who was at the time an undergraduate at Stanford. When I asked Al about Stanford's engineering faculty, he was the one who told me about Professor Inan. The following summer, Al and I coincidentally accepted positions at another job together. We went on to work together on our master's degree coursework at Stanford and have become very good friends.

I owe much to my friend Dave Sigurdson, whom I met in my first undergraduate year. Having all of the same pre-engineering math and science classes, Dave and I partnered up to study together. During those times, I learned from Dave's maturity and good study habits (and skillfully won about 40% of our occasional matches of trash-can basketball). We've been close friends over the past ten years, and I am honored to be the godfather of Dave's first son.

My friend Sergio Keusayan and I met in third grade. From swimming lessons to midnight skateboarding expeditions to hanging out after the senior prom (our poor dates!) to unorthodox fishing ventures to our trip across the country, Sergio and I have had some of the best possible times, and I am better for having known him.

I owe much of who I am and what I have accomplished to my parents Linda and Robert Johnson. I would like to thank my father for the many gifts he has given me over the years; he has been a model of integrity and kindness. My mom is

inspirational with her wisdom and cheer, and I thank her for the unflagging support and affirmation she has given me. I'm also grateful to my parents for making me such a nice brother, James. "Little Bro" and I were inseparable for years as we grew up, and are now the closest of brothers. I would like to thank him for being my Best Man, and for all the good times that we've had and will have in the future.

The most fortunate day in my life was the day that I met my wife, Rachel Stewart Johnson. Rachel and I have had some wonderful experiences together at Stanford. Even when one of us was traveling for research, we've been very close — I remember anxiously awaiting my weekly 15-minute satellite-patched phone call to Rachel while I was stationed at Palmer Station, Antarctica. If anything could have made Antarctica more beautiful, it was Rachel's voice. I would like to thank Rachel for all of her support with this work, and I am looking forward to sharing my life with her.

<div align="right">Michael P. Johnson</div>

Stanford, California
September 20, 2000

Contents

List of Tables

List of Figures

Chapter 1

Introduction

Very Low Frequency (VLF) radio waves ($\sim$3 to 30 kHz) are guided by the spherical waveguide (hereafter referred to as the Earth-ionosphere waveguide) formed between the Earth's surface and the lower edge of the ionized portion of the atmosphere (i.e., the lower ionosphere), and can efficiently propagate across long distances. The amplitude and phase of the signals received at any point depend on the electrical conductivity of the ionosphere as well as the ground. Under the right circumstances, the observed properties of VLF signals can be used to determine the spatial and temporal structure of localized disturbances in the lower ionosphere — a technique referred to as VLF remote sensing.

Such localized conductivity disturbances in the lower ionosphere occur both directly and indirectly as a result of electromagnetic radiation emitted by lightning discharges [e.g., *Inan et al.*, 1996a, and references therein]. Application of VLF remote sensing to image localized ionospheric disturbances induced by lightning discharges is the primary subject of this dissertation. The potential importance of lightning effects in the ionosphere is underscored by the fact that lightning discharges individually radiate $\sim 10^6$ J as electromagnetic energy [*Uman*, 1987; pp. 322–323], with $\sim$1800 thunderstorms occurring on the Earth at any given time [*Brooks*, 1925], producing a total of $\sim$37 discharges every second [*Christian et al.*, 1996].

We begin this chapter with a brief description in Section 1.1 of the composition of the Earth's nearby plasma environment. We then discuss VLF propagation in the

Earth-ionosphere waveguide in Section 1.2 and introduce the VLF propagation and scattering models used in this thesis. VLF remote sensing is employed in this work to study two varieties of lightning-induced ionospheric disturbances. These two types of disturbances are introduced, and examples are provided in Section 1.3. We conclude with a summary of the contributions of this work.

1.1 The Earth's Plasma Environment

In this section, we introduce the two primary ionized regions of the Earth's nearby plasma environment: the ionosphere and the magnetosphere.

1.1.1 The Ionosphere

The term "ionosphere" refers to that portion of the atmosphere with sufficient ionization to affect the propagation of radio waves. First postulated at the end of the nineteenth century by observations of diurnal variations in the Earth's magnetic field, its existence was confirmed by a series of radio experiments, beginning with the famous trans-Atlantic communication by Marconi in 1901 [*Tascione*, 1994; p. 89].

The ionosphere consists of several electrically neutral ionized layers, commonly referred to as the D, E, and F regions, which are produced because of the different rates of attachment and recombination processes at different ionospheric altitudes. The effectiveness of these processes varies from daytime to nighttime, when production is maintained by scattered solar radiation and non-solar sources. Typical ionospheric electron density profiles are shown for both day and nighttime conditions in Figure 1.1. The D layer, primarily produced by hard X-rays and Lyman-α radiation, is typically said to extend from $\sim$70 km to $\sim$90 km. Ionization density increases to $\sim$10^5 electrons/cm^3 in the daytime E layer, primarily caused by soft X-rays. The sun's extreme ultraviolet radiation increases the ionization by another order of magnitude in the F layer. Above the F layer, the electron density decreases monotonically up to magnetospheric boundaries which lie at much higher altitudes (see Section 1.1.2).
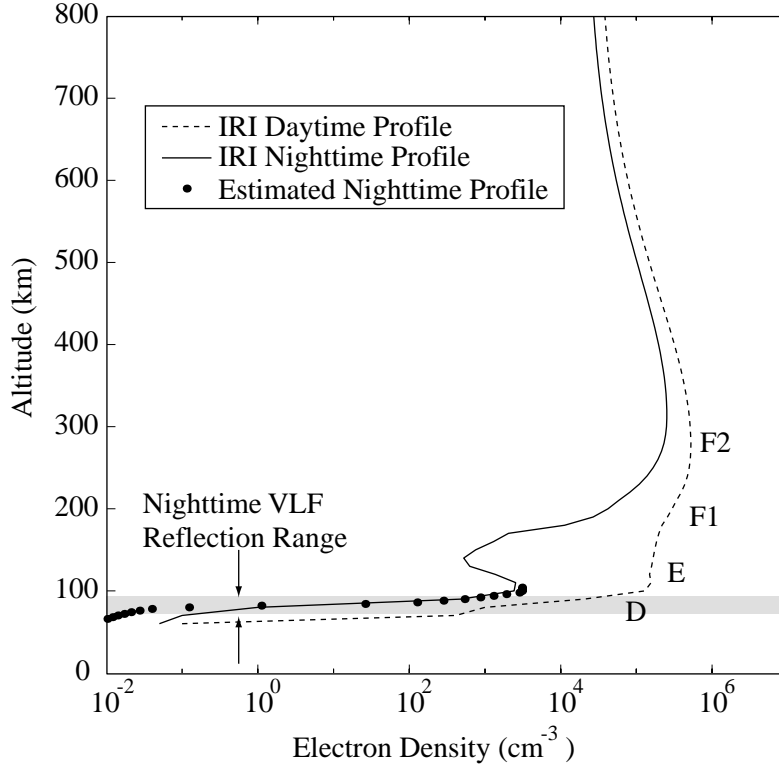
Figure 1.1: Ionospheric electron density profiles. Daytime and nighttime electron density differs by orders of magnitude, particularly in the D and E regions. The solid lines are profiles taken from the International Reference Ionosphere [*Rawer et al.*, 1978], while the points are an estimate of the D region density taken from Section 4.4.2.

An overview of the production and loss processes at different altitudes is given by *Rishbeth and Garriott* [1969, pp. 87–125].

In this thesis, we restrict our attention to the measurement of direct and indirect effects of lightning discharges on the lowest altitudes of the ionosphere, specifically the altitude range below ∼100 km in the D region. Furthermore, we primarily consider ionospheric disturbances which occur during nighttime, when the ambient ionization levels are substantially lower (Figure 1.1). A two-parameter analytical expression for the altitude dependence of the D region electron density was given by *Wait and Spies* [1964] as: $N_e(h) = 1.43 \times 10^{13} \exp(-0.15h') \exp([(\beta - 0.15)(h - h')]$, where N_e is electron density in electrons/cm^3, h is the height in km, and h' and β are model parameters having units of km and km^{-1}, respectively. The h' parameter

was shown to be a good representation of the approximate height at which VLF reflections occur, while the β parameter describes the sharpness of the profile. The *Wait and Spies* [1964] model has been successfully used in previous comparisons of VLF measurements and theory [e.g., *Cummer et al.*, 1998], and is used in a modified form in this work (see Section 4.4.2).

For radiowave propagation below the F region, the effective electron-neutral collision frequency profile, largely determined by the relatively stable neutral density, is important in addition to electron density. In this work, we exclusively employ an exponential collision frequency profile given by $\nu_e(h) = 1.86 \times 10^{11} e^{-0.15h}$, where h is height in km, and ν_e is the collision frequency in s^{-1} [*Wait and Spies*, 1964] .

1.1.2 The Magnetosphere

The term "magnetosphere" refers to that portion of the atmosphere in which the motion of charged particles is dominated by the Earth's magnetic field. Beyond the magnetosphere, an interplanetary magnetic field dominates, and a stream of energetic plasma known as the solar wind flows away from the Sun [*Tascione*, 1994; pp. 31–42]. The magnetosphere is in the form of a bullet-shaped cavity in the solar plasma, with its outer boundary extending about ten Earth radii towards the Sun, and more than 60 Earth radii away from the Sun [*Tascione*, 1994; pp. 57–78]. While the outer regions of the Earth's magnetic field are significantly distorted by the solar wind, the field is dipolar in configuration within a region extending out to several Earth radii[1]. The "plasmasphere" occupies this inner region, in which a population of ions and electrons with energies of $\sim$1 eV is maintained by means of a diffusive equilibrium [*Angerami and Thomas*, 1964]. This "cold plasma" co-rotates with the Earth due to frictional coupling, and exists with densities ranging from 10^4 cm^{-3} at an altitude of 1000 km to 10–100 cm^{-3} near the outer edge [*Tascione*, 1994; p. 68]. The electron density drops sharply by two orders of magnitude at the outer edge of the plasmasphere, at

---

[1]A parameter used to identify magnetic field lines is the L value, which corresponds to the distance, measured in Earth radii, from the center of the Earth to the point at which the magnetic field line crosses the magnetic equatorial plane.

a boundary known as the "plasmapause" [*Carpenter*, 1970].

In addition to the background cold plasma, an abundance of trapped energetic electrons and ions was discovered to be present in the inner magnetosphere by Van Allen in 1958 with the Explorer I satellite [*Van Allen*, 1983]. These energetic electrons and ions, making up the Earth's so-called Radiation Belts, exhibit three classes of motion in their trapped orbits [*Walt*, 1994, pp. 36–54]: (i) gyromotion around the ambient magnetic field with time scale of milliseconds, (ii) mirrored reflections from conjugate hemispheres with time scales of tenths of seconds, and (iii) longitudinal drifts around the Earth with time scales of tens of minutes. Radiation belt electrons are injected by a variety of mechanisms, such as the decay of cosmic ray albedo neutrons, the solar wind, the ionosphere, and anomalous cosmic rays [*Walt*, 1996]. Although their loss rates within ∼0.3 Earth radii are consistent with losses from atmospheric collisions [*Walt*, 1964], resonant wave-particle interactions are thought to be the dominant mechanism for the loss of trapped particles on field lines that extend farther from the Earth [*Walt*, 1996]. In these interactions, electromagnetic waves propagating relatively slowly (phase velocities on the order of ∼1% to ∼10% of the speed of light in free space) through the background cold plasma can resonantly interact with the energetic particles, changing their momentum, and causing them to precipitate out of their trapped orbits onto the lower ionosphere [*Schulz and Lanzerotti*, 1974, pp. 60–62; *Inan et al.*, 1978]. An important source of such electromagnetic waves at mid to low latitudes are lightning discharges; precipitation of energetic electrons by waves originating in lightning is one of the subjects studied in this thesis (see Chapter 4).

1.2 VLF Propagation and Scattering in the Earth-Ionosphere Waveguide

The subject of this thesis is VLF remote sensing of ionospheric disturbances induced directly or indirectly by lightning discharges, using measurements of VLF signals

propagating in the Earth-ionosphere waveguide. Accordingly, we now provide a brief background on VLF propagation and scattering in the waveguide formed by the conducting boundaries of the Earth and the lower ionosphere.

Electromagnetic waves reflect when incident upon conducting boundaries, and can be guided along partially enclosed conducting structures. At VLF, the surface of the Earth and the lower edge of the ionosphere act as good electrical conductors. The skin depth of the Earth's surface at 10 kHz is ~2.5 m for seawater ($\epsilon_r = 81, \sigma = 4$ S/m), and ~500 m for dry earth ($\epsilon_r = 3, \sigma = 10^{-4}$ S/m) [*Inan and Inan*, 1999; p. 56]. While this skin depth is much less than the free space wavelength of 30 km, it is sufficient to facilitate sub-surface reception, such as for submarine communication. The upper boundary of the Earth-ionosphere waveguide consists of the lower ionosphere, which is a weakly ionized gas in which the motion of ions and neutral molecules is often neglected [*Budden*, 1985; p. 55], and the rate of electron collisions with the neutral air molecules is determined by the electron and neutral temperatures [*Chapman and Cowling*, 1970; p. 188]. "Magnetoionic" theory specifies the refractive index for uniform plane wave propagation in this region, in terms of the vector magnetic field, wave frequency, local plasma frequency $\omega_p = N_e q_e^2 / m_e \epsilon_0$, electron gyrofrequency $\omega_h = q_e |\mathbf{B}|_\perp / m$, and electron-neutral collision frequency ν_e. Because the collision frequency is much larger than the plasma frequency and gyrofrequency for a distance of several VLF wavelengths above the earth's surface, the index of refraction is approximately unity, resulting in essentially free space propagation. In the lower D region, the refractive index changes rapidly (due to a sharp increase in free electron density N_e over the distance of a wavelength) resulting in substantial reflection. For VLF propagation, this region is lossy due to electron-neutral collisions, and is anisotropic due to electron gyromotion influenced by the Earth's magnetic field[2].

There are two methods often used to study VLF waveguide propagation. In the ray optics approach [*Morfitt and Shellman*, 1976], propagation of the signal between transmitter and receiver locations is analyzed in terms of an infinite number of rays

---

[2]One interesting consequence of this anisotropy is the larger attenuation for east-to-west paths than for west-to-east ones [*Round et al.*, 1925; *Snyder*, 1968].

which satisfy the boundary conditions at all points along the propagation path. Those rays that propagate with an increased angle with respect to the waveguide axis suffer increased attenuation due to a larger number of lossy reflections and the increased propagation path length. The ray optics approach is not suited for determination of the signal characteristics at large ($>\sim$500 km) distances from the source, due to the need to consider an unreasonably large number of discrete ray paths. This method is also impractical in cases where the field intensity needs to be calculated at multiple points along the path, since an entirely new set of ray paths must be recalculated for each receiver point.

Alternatively, the signal propagating in the waveguide can be represented by a superposition of discrete waveguide modes. For waveguides with perfectly conducting walls, modes are generally classified as transverse electric (TE) or transverse magnetic (TM), depending on whether the wave electric or magnetic field is entirely transverse to the direction of propagation. The eigenvalues that determine the phase constants for individual waveguide modes are determined from a condition of planar phase front coherence specifying that component uniform plane waves which constitute the mode and which reflect from one boundary and then the other must have advanced in phase by $2\pi m$ radians, where m is an integer [*Inan and Inan*, 2000; p. 269]. The waveguide modes are identified by a mode number that is defined by the number of maxima and minima in the transverse field pattern. For perfectly conducting boundaries, mode theory yields simple analytical expressions for the steady state electric and magnetic fields.

More generally, when the upper and lower boundaries may consist of lossy and/or anisotropic material such as in the case of the Earth-ionosphere waveguide, the eigenvalues (from which the wave phase constant can be derived) of individual modes can once again be calculated via the planar phase front coherence condition, which in general reduces to the solution of the eigenangles of $det[\mathbf{I} - \mathbf{R}_L(\theta)\mathbf{R}_U(\theta)] = 0$, where $\mathbf{I}$ is the identity matrix, $\mathbf{R}_L$ is the reflection matrix for the lower boundary, $\mathbf{R}_U$ is the reflection matrix for the upper boundary, and θ is the angle of the plane wave

with respect to the boundary [*Budden*, 1961; pp. 115–117]. With the entries of the reflection coefficient matrices being complex for the ground, and both complex and anisotropic for the ionosphere, the determination of the eigenangles must be carried out numerically. The Earth-ionosphere waveguide propagation theory developed by *Budden* [1962] takes into account the Earth's curvature, geomagnetic field, altitude profiles of electron-neutral collision frequency and electron density, and serves as the basis for the numerical modeling codes utilized in this thesis.

In general, higher order waveguide modes have a larger spatial attenuation rate [*Wait*, 1957] and are less efficiently radiated from transmitting structures equivalent to vertical monopoles above ground [*Jordan and Balmain*, 1968; pp. 641–644; *Poulsen*, 1991; p. 48], thus limiting the number of modes needed for simulation. According to *Morfitt and Shellman* [1976], for simulation of VLF propagation in the Earth-ionosphere waveguide, only a single mode is required for frequencies below 3 kHz, about 10 to 15 modes are required at 30 kHz, and as many as twenty-five modes may be important at 60 kHz[3]. Single waveguide mode analytical solutions have been used to interpret variations of narrowband VLF transmitter signals propagating on long ($\geq$6000 km), primarily sea-based, paths [*Inan and Carpenter*, 1987; *Poulsen et.al*, 1990], but are not useful for the relatively short (<3000 km) land-based paths considered in this work.

For relatively short paths, and for cases with sharp gradients in the ground or ionospheric conductivity along the propagation path, consideration of multiple modes is necessary for accurate numerical solutions. Along most propagation paths, one or more of the waveguide boundary parameters may vary. These variations can be abrupt, such as the change in ground conductivity and relative permittivity across a land/sea boundary, or they can be smooth (i.e., varying negligibly over spatial scales comparable to a VLF wavelength), such as the change in the vector orientation of the static magnetic field (which determines the complex refractive index of the ionospheric boundary). Abrupt variations lead to coupling of energy between different waveguide

---

[3]For the $\sim$25 kHz propagation modeling in this work, 20 modes were included.
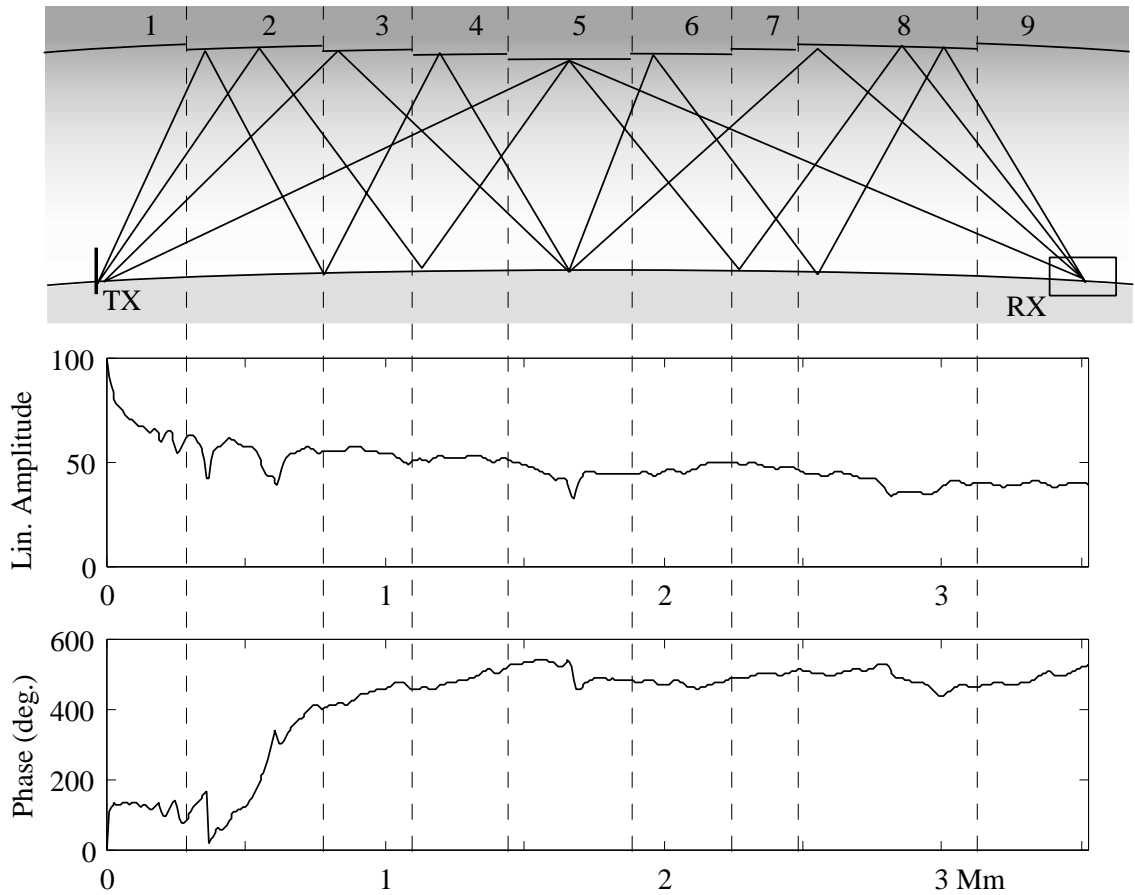
Figure 1.2: VLF signal propagation. The top panel shows example ray paths from a VLF transmitter to a receiver. The path of propagation has been quantized into hypothetical slabs in this illustration, each with an associated magnetic field, electron density and temperature profile, and ground conductivity and relative permittivity. The variation with distance of the transmitted amplitude and phase of the signal are plotted below (from a simulation with a 3.5 Mm path length).

modes [*Wait*, 1968].

A numerical example of VLF propagation in the Earth-ionosphere waveguide is presented in Figure 1.2. The top panel shows the great circle path of propagation segmented into regions with different ionospheric conductivity profiles. To aid in the visualization, the ray optics approach is taken, and only four ray paths are depicted. In the lower two panels, the amplitude and phase of the VLF signal (as computed numerically using available models described later in this section) are plotted as a function of distance from the transmitter. The signal amplitude corresponds to the (arbitrarily scaled) amplitude of the vertical electric or magnetic field at receiver

points at ground level. The signal phase plotted in Figure 1.2 corresponds to the *difference*, in degrees, between the phase of the modeled field and the phase of a signal propagating in free space to the same radial distance at the transmitter's center frequency. At several points along the propagation path, the amplitude dips sharply and the phase correspondingly undergoes sharp changes. These amplitude nulls and phase shifts are caused by destructive interference in the superposition of multiple propagating modes, each of which propagate with different phase and attenuation constants. With large distances from the transmitter, as one mode (typically the one with the lowest attenuation rate) becomes dominant in intensity, the interference of the other modes diminishes in intensity, and in general the depth of the nulls becomes smaller.

The efficient propagation of wave energy in the VLF band up to large distances in the Earth-ionosphere waveguide results in a spectrum laden with signals from both natural and man-made sources. The bulk of the energy radiated by electromagnetic pulses due to lightning return strokes is in the ELF/VLF range [*Arnold and Pierce*, 1964]. These impulses, known as VLF radio atmospherics, or "sferics", occur on time scales of several milliseconds, and can propagate over global distances. Their measured properties have been used to deduce causative lightning currents [*Uman*, 1987; pp. 330–334], as well as information about the properties of the ionosphere along the great circle path of propagation [*Cummer et al.*, 1998].

An example of a typical VLF spectrum, as observed in this case at Fort Collins, Colorado, is shown in Figure 1.3. The superposition of the natural and man-made VLF signals results in an approximately constant average envelope in the one-second time domain snapshot, with the exception of several intense sferics. These impulses have broad spectral content in the VLF range, as can be seen in the resulting dynamic spectra[4] exhibiting vertical lines of increased intensity. VLF transmitter signals, for example those originating in Hawaii, Maine, Washington, and Puerto Rico (see

---

[4]Dynamic spectra such as that shown are used to display the frequency content of dynamic signals in the frequency-time domain. Successive FFTs are calculated, and their magnitude is plotted with a color scale for each time period. With the appropriate Δf versus Δt tradeoff, a spectrogram reveals the shape of transient signatures that may be obscured in the time domain.
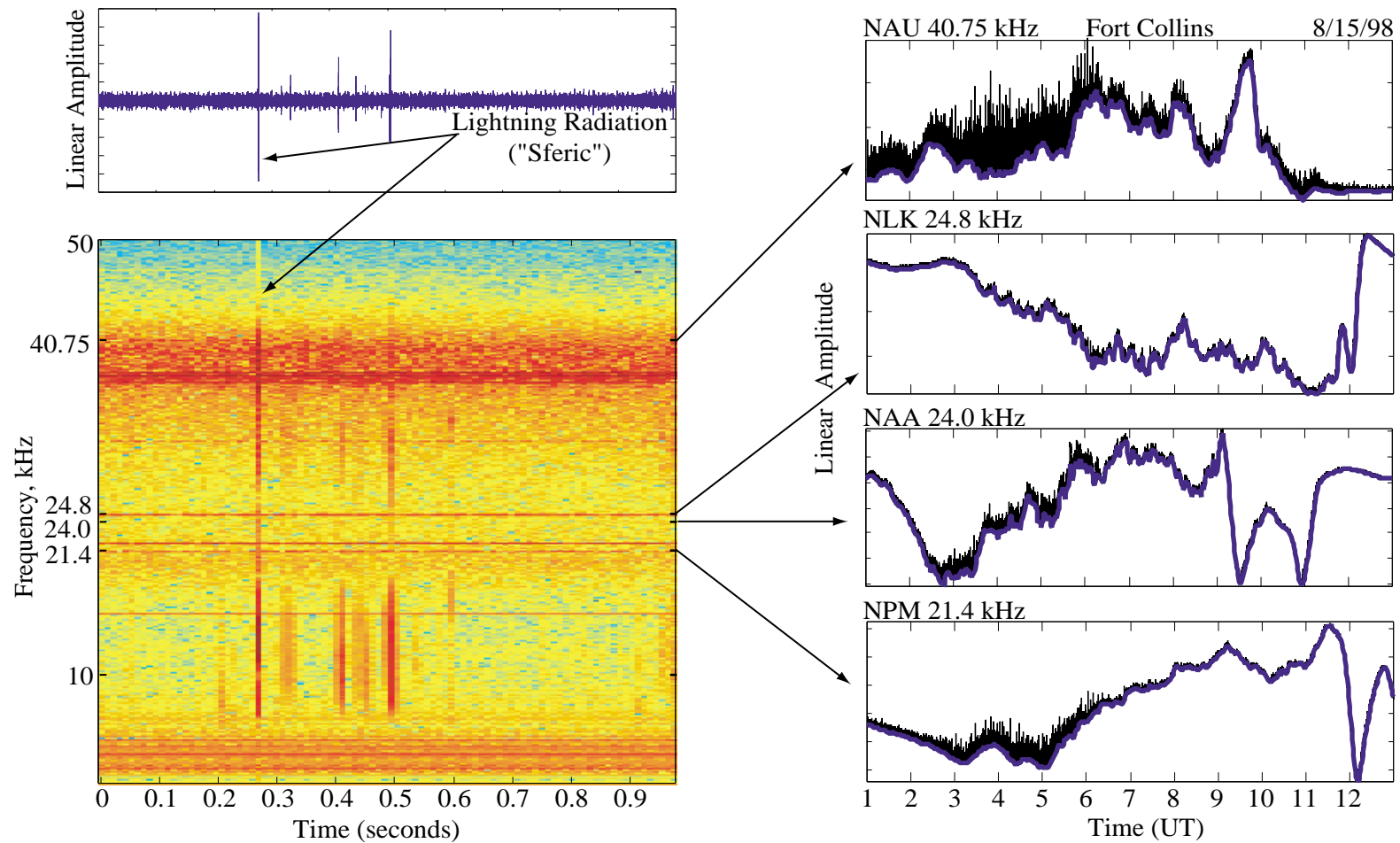
Figure 1.3: Example VLF data. A one second time domain snapshot of broadband data has a nearly constant envelope with several impulses due to lightning discharges. The resulting spectrogram shows the broadband nature of the sferics, along with the narrowband VLF transmitter signals. Example narrowband amplitude data (amplitude is detected from a ± 150 Hz band around the carrier frequency) from the four transmitters (see Table 2.1) used in this work for a 12-hour period as measured at a receiver in Fort Collins, CO, is shown on the right.

Table 2.1 in Section 2.1), appear as narrow horizontal lines in the spectrogram. The intensity of these signals is nearly steady over this one-second period, but undergoes dramatic diurnal changes as shown in the twelve hour narrowband amplitude records for the four VLF transmitters used in this work.

In this work, subionospheric VLF propagation in the presence of localized D region disturbances is quantitatively modeled using a waveguide mode approach. Based upon a mathematical formulation developed by *Budden* [1962], in which the Earth's curvature, magnetic field, electron-neutral collision frequency, and electron density are taken into account, a two-dimensional model was developed at the Naval Research and Development Laboratory [*Ferguson et al.*, 1989, and references therein]. This model, known as the Long Wave Propagation Capability (LWPC) code, assumes a two-dimensional cylindrical geometry (but with an added geometrical correction so as to accurately model the spherical geometry of the Earth-ionosphere waveguide) in which there is no variation in waveguide parameters along the axis perpendicular to the direction of propagation. The planar phase front coherence condition for calculation of mode eigenangles assumes the waveguide parameters within each slab to be uniform in the direction transverse to the propagation path, and results in modes which propagate independently of one another. While a completely homogeneous waveguide model can be useful in some circumstances [e.g., *Cummer et al.*, 1997], a more general case consists of propagation along a great circle path with changes in waveguide parameters such as ground conductivity, magnetic field, and ionospheric electron density profile (and hence conductivity). Whenever such a change is encountered along a propagation path, particularly for sharp gradients with spatial scales of less than a wavelength, wave energy can be coupled among the individual modes [*Wait*, 1968].

To quantitatively evaluate the signal amplitude and phase along realistic propagation paths while accounting for such mode coupling, the LWPC code consists of three components. An initial routine, PRESEG, references a table of the earth's ground conductivity and a magnetic field model, and forces boundaries along the waveguide

propagation path at points where those parameters change significantly (such as a land-sea boundary). In addition, waveguide parameters can be varied along the path by case-specific break points (in Figure 1.2, break points are shown for hypothetical changes in the electron density profile along the path of propagation). Within each region, a routine named MODEFNDR uses these waveguide parameters and searches for eigenangles which satisfy the planar phase front coherence condition [*Ferguson and Snyder*, 1987]. Although the execution time of MODEFNDR is significantly reduced by limiting the number of modes, the relatively short paths used in this work required attention to multiple modes, and 20 modes were considered in this work. A third routine, FASTMC, calculates the mode conversion coefficient matrices at the predefined boundaries, and calculates the resulting vertical electric field as a function of height and distance along the propagation path [*Papert and Ferguson*, 1986].

Poulsen et.al [1990] and *Poulsen et.al* [1993a, b] extended the two-dimensional LWPC model to include effects of waveguide parameter variations in the dimension transverse to the direction of propagation to model cases in which a localized ionospheric disturbance occurs on or near the propagation path. The total electromagnetic field at the receiver was calculated as the superposition of the field arriving over the direct path from the transmitter and the field scattered by a localized "disturbance" in the waveguide, as illustrated in Figure 1.4. The scattered field was modeled by first calculating the electromagnetic field which propagated to the disturbance, then calculating the fraction of the electromagnetic field which is scattered in the direction of the receiver, and propagating that scattered component to the receiver. The two-dimensional propagation along the three individual paths was modeled by the LWPC program, and thus included the effects of mode coupling across sharp waveguide discontinuities. The localized waveguide disturbance was assumed to be smoothly varying over spatial scales on the order of a wavelength, allowing the mode coupling within the disturbance to be neglected. Although the three-dimensional modeling in this dissertation assumes azimuthal symmetry of the scattering region, the 3D model is not restricted to this case [e.g. *Rodriguez and Inan*, 1994].
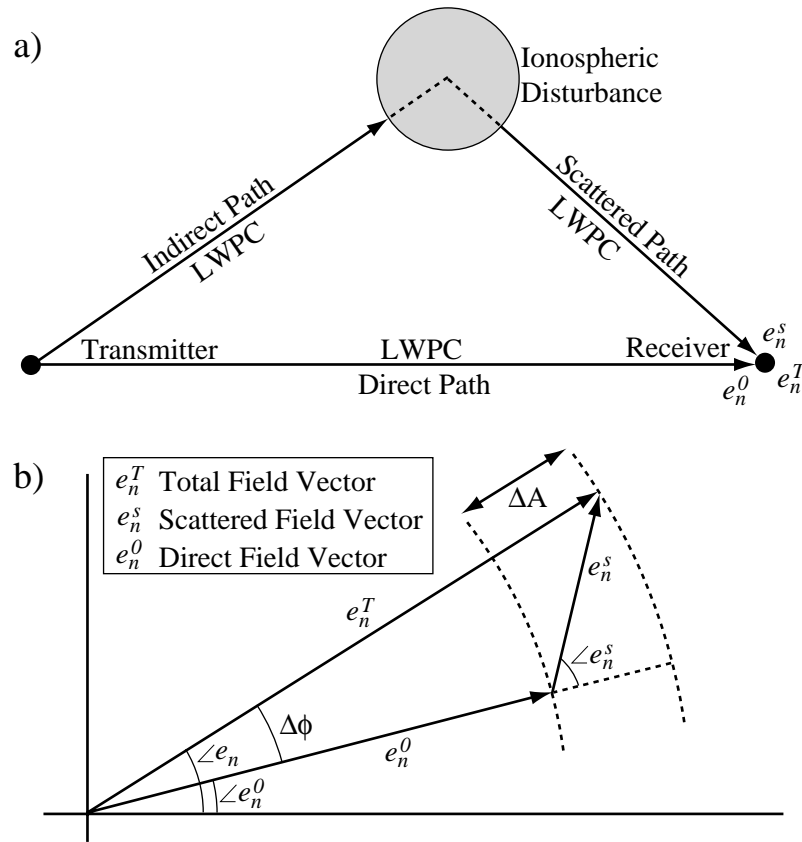
Figure 1.4: Segments of the three-dimensional LWPC model. (a) A representation of the direct and indirect (scattered) great circle paths considered in the three-dimensional Long Wave Propagation Capability (LWPC) model. (b) The phasor representation of the direct, scattered, and total received field vectors. Adapted from *Poulsen* [1991].

1.3   Lightning-Induced VLF Signal Perturbations

Very Low Frequency probing is a powerful tool for remote sensing of transient D region ionospheric disturbances. Using VLF techniques, studies have been made of D region processes involving solar flares [*Bracewell and Straker*, 1949], meteor showers [*Chilton* 1961], nuclear detonations [*Zmuda et al.*, 1963], auroral enhancements [*Cummer et al.*, 1997], and gamma ray flares of extraterrestrial origin [*Inan et al.*, 1999].

During nighttime, when relatively low electron densities make the D region inaccessible to probing with radar and ionosondes, VLF transmitter signals propagating in the earth/ionosphere waveguide are sensitive to even slight (a few percent) heating

or ionization enhancements, which can cause conductivity changes at ∼85 km altitudes. The particular type of transient ionospheric conductivity changes considered in this work are those caused by lightning. Lightning discharges regularly disturb the nighttime D region, producing intense (by factors of ∼10 to ∼100) heating of ambient electrons lasting for a few hundreds of ms [*Inan et al.*, 1991; *Pasko et al.*, 1996], ionization changes which recover in tens to hundreds of seconds [*Inan et al.*, 1991; *Taranenko et al.*, 1993; *Inan et al.*, 1996a], and quiescent changes in electron temperature of tens of percent [*Inan et al.*, 1996b; *Pasko et al.*, 1998] that are maintained throughout the duration of individual thunderstorms. These localized disturbances are often manifested as sudden changes in the amplitude and/or phase of a VLF signal propagating on a nearby path, followed by a relatively slow recovery back to the "ambient" level (the signal level that would have been in effect in the absence of the transient perturbation). In this work, such perturbations on a subionospheric VLF signal are referred to as "VLF events".

The particular two varieties of lightning-induced VLF events studied in this work, known as "early/fast" and "LEP" VLF events, are shown in Figure 1.5. "Early/fast" VLF events, the result of a *direct* effect of a lightning discharge on the conductivity of the lower ionosphere, are introduced in Section 1.3.1 and are the subject of Chapter 3. Lightning-induced electron precipitation (LEP) VLF events result in an *indirect* modification of the lower ionospheric conductivity, in which the VLF electromagnetic discharge radiated by lightning propagates into the magnetosphere and interacts with trapped energetic electrons, causing precipitation into the lower ionosphere and producing secondary ionization therein. LEP event signatures are introduced in Section 1.3.2 and their investigation is the subject of Chapter 4.
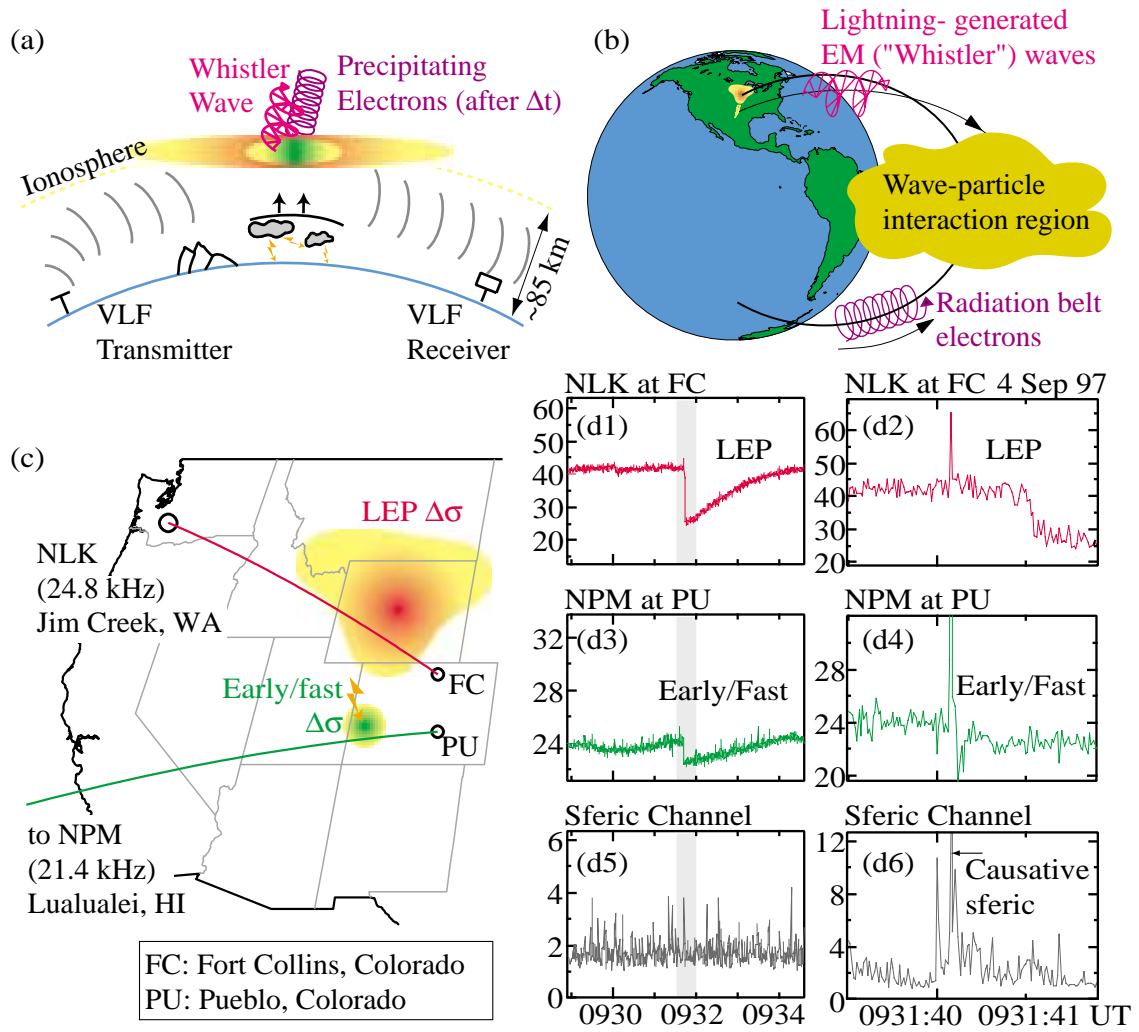
Figure 1.5: Early/fast and LEP VLF events. (a) Cross section of the Earth-ionosphere waveguide, with a relatively small (early/fast) ionospheric disturbance and a relatively large (LEP) ionospheric disturbance. (b) Illustration of the magnetospheric propagation path of a lightning-induced whistler wave. The whistler wave can change the momentum of trapped radiation belt electrons, causing them to precipitate into the atmosphere. (c) On 4 September 1997, at ∼09:31:40.2 UT, a lightning discharge in Midwestern Colorado occurred within 50 km of the NPM–PU propagation path. Superimposed upon the map are shaded regions illustrating an associated direct coupling (early/fast) disturbance along the NPM–PU path, and an associated indirect coupling (LEP) disturbance along the NLK–FC path. (d1,d2) The NLK signal amplitude exhibits a decrease after a several hundred millisecond onset delay, characteristic of LEP VLF events. (d3,d4) The NPM signal amplitude exhibits a decrease simultaneously (within 20 ms) with respect to the causative lightning discharge, characteristic of early/fast VLF events.

1.3.1 "Early/Fast" VLF Events

"Early/fast" VLF events exhibit a rapid onset (<20 ms, i.e., "fast") followed by a relatively slow recovery (tens of seconds) and occur within 20 ms of a causative lightning discharge (i.e., "early") [*Inan et al.*, 1993]. An example early/fast event is shown in both low and high resolution in Figure 1.5. In this case, the event occurs on the amplitude signal that originates from a VLF transmitter in Hawaii, and is recorded at a VLF receiver in Pueblo, Colorado. At ~9:31:40 UT, the received signal amplitude decreased by ~0.7 dB, and recovers back to the pre-event level in ~100 s. In the high resolution view of the event onset, one can see an impulse from a radio atmospheric intruding into the transmitter's narrowband spectrum (21.4 ± 200 Hz) at the onset time. This sferic was associated with a cloud-to-ground (CG) lightning discharge in Western Colorado, indicated by an arrow in the figure, less than 50 km from the great circle path of propagation.

The physical mechanism underlying these events is not yet quantitatively understood. Quasi-electrostatic thundercloud fields may quiescently heat the D region of the ionosphere and modify its ambient conductivity throughout the duration of an active thunderstorm [*Inan et al.*, 1996b]. Lightning-induced changes in the thundercloud charge may lead to localized heating/cooling of the D region causing small changes in the vicinity of the quiescent value and thus affect the nighttime reflection height (~85 km) of subionospheric VLF signals. However, it has also been suggested that these events may be due to secondary ionization regions produced by electromagnetic impulses radiated by lightning and associated with optical discharges known as Elves [*Dowden et al.*, 1996a] or ionization columns associated with Sprites [*Dowden et al.*, 1996b], so that the physical nature of ionospheric disturbances involved in these events remains in dispute [*Inan et al.*, 1996c].

In Chapter 3, the typical scattering pattern of these direct disturbances is determined by comparing simultaneous measurements of the perturbed amplitude and phase at multiple sites along a "holographic" strip with a numerical model of VLF propagation and scattering in order to estimate the lateral extent of the disturbances.

In addition, the nature of the associated CG lightning discharges which lead to these types of VLF events is discussed and a summary of occurrence statistics is presented.

1.3.2 Lightning-Induced Electron Precipitation Events

Lightning-Induced Electron Precipitation (LEP) VLF events exhibit an onset delay (a few hundred ms up to 1 s) with respect to a causative lightning discharge, an onset duration (typically 0.5–1.5 s), and a recovery period of 10–100 s [*Burgess and Inan*, 1993]. An example LEP event is shown in Figure 1.5, associated with the same lightning discharge as in the previous early/fast event example. While the early/fast event appeared on the NPM signal from Hawaii to Pueblo, Colorado, which passed fewer than 50 km from the location of the lightning discharge, the LEP event[5] occurred on the NLK signal originating in Washington (State) and received at Fort Collins, Colorado (traversing a path that is poleward displaced by several hundred kilometers with respect to the discharge). As shown in the high resolution view, the signal amplitude remains constant for nearly 1 s after the occurrence of the lightning (as signified by the causative sferic), after which it decreases by $\sim$4 dB over a period of several hundred ms. The amplitude then recovers back to its pre-event level in $\sim$100 s.

This type of event was first observed by Mike Trimpi while monitoring VLF transmitter signals in Antarctica [*Helliwell et al.*, 1973]. The VLF transmitter signal perturbations were hypothesized to be due to secondary ionization at the VLF reflection height by the scattered energetic electrons and were named lightning-induced electron precipitation events[6]. There is now extensive experimental evidence for this type of precipitation as measured on satellites, rockets, and via subionospheric VLF remote sensing [*Voss et al.*, 1998 and associated references therein].

---

[5]As discussed in Section 4.5, LEP and early/fast events typically happen during different times of the year under specific lightning and/or magnetospheric conditions. This example from 4 September 1997 is a rare case with favorable conditions for both types of events and the proper observational configuration to record them both.

[6]VLF events were widely referred to as "Trimpi" events in the literature of the 1970s and 1980s, with some persistence even today. With the discovery of early/fast and other types of events, we now specify the variety in identification, such as "early/fast VLF events" or "LEP VLF events".

The majority of previous theoretical [e.g., *Inan et al.*, 1989] and experimental [e.g., *Burgess and Inan*, 1993] work on the LEP phenomena mostly emphasized interactions with "ducted" whistler waves that propagate in field-aligned regions of enhanced ionization (see Section 4.2). While the possibility of this resonant pitch angle scattering by obliquely propagating "nonducted" whistlers has been recognized [*Jasna et al.*, 1992], the first comprehensive quantitative model of the transient precipitation of bursts of energetic electrons by oblique whistlers launched by individual lightning flashes has only recently been realized [*Lauben et al.*, 1999]. The predictions of this model have been verified via measurements of subionospheric VLF signal amplitude and phase along a holographic strip [*Johnson et al.*, 1999b].

Observations of LEP disturbances with multiple receivers are presented in Chapter 4, along with a quantitative interpretation of the disturbance sizes, temporal signatures, and occurrence statistics.

1.4 Contributions

Prior to this work, VLF remote sensing had been primarily employed with networks of a few widely spaced great circle paths, due in part to the complexity in design and operation of the custom-built analog receivers utilized. Despite this limitation, extensive studies of LEP VLF events [e.g., *Helliwell et al.*, 1973; *Inan and Carpenter*, 1987; *Burgess and Inan*, 1993; *Lev-Tov et al.*, 1995] and early/fast VLF events [e.g., *Armstrong*, 1983; *Burke et al.*, 1991; *Inan et al.*, 1993; *Inan et al.*, 1996a] were carried out, enabling the identification of the unique event signatures, cause and effect relationships, and providing support for various theoretical investigations into the causative mechanisms [e.g., *Chang and Inan*, 1985; *Dowden et al.*, 1996a; *Inan et al.*, 1996b].

With recent technological advances, namely GPS-based timing, personal computer processor speed, and the ubiquity of Internet access, a relatively low-cost VLF receiver was developed and integrated with front-end electronic systems adapted from the

early fully-analog receivers. Following *Chen et al.* [1996], a strategic deployment of digital VLF receivers was completed with optimal spacing for the holographic imaging of lightning-induced ionospheric disturbances. This Holographic Array for Ionospheric/Lightning research (HAIL) system consisted of nine receivers in a North-South orientation in the midwestern United States, began operation in the summer of 1998, and formed the basis for the following scientific contributions of the author:

- *Johnson et al.* [1999a], Chapter 3: Measured the scattering pattern of early/fast lightning-induced ionospheric disturbances at multiple stations, and determined their spatial extent using the measurements together with a 3D VLF propagation and scattering model;

- *Johnson and Inan* [2000], Chapter 3: Identified a key signature of lightning discharges that leads to direct disturbances of the overlying ionosphere;

- Chapter 3: Produced the first year-long database of early/fast VLF events. Interpreted an observed correlation between early/fast event activity and lightning activity along the great circle paths of propagation, and determined the fraction of cloud-to-ground discharges which led to early/fast events for a two-month period.

- *Johnson et al.* [1999b], Chapter 4: Provided the first evidence of precipitation of radiation belt electrons by obliquely propagating (nonducted) whistler waves launched by lightning, and quantitatively assessed the predictions of a recent theoretical model;

- Chapter 4: Produced the first year-long database of indirect coupling events identifying a clear correlation between LEP event activity and geomagnetic activity.

Chapter 2

Description of Experiment

Very Low Frequency remote sensing relies upon high resolution measurements of the amplitude and phase of subionospherically propagating coherent signals generated by a VLF transmitter. In this chapter, we describe the characteristics of the transmitters and the VLF receiving systems used in this study, and the geographical configuration of these receivers, collectively known as the Holographic Array for Ionospheric/Lightning research (HAIL).

2.1 VLF Transmitter Signals

The U. S. Navy operates transmitters in the 10 to 50 kHz frequency range for global communication and navigation with submarines and surface ships. The use of the radio frequency band at the low end of the spectrum stems from two factors: (i) the skin depth of electromagnetic signals is inversely proportional to the square root of frequency ($\sim$2.5 m for seawater at 10 kHz, Section 1.2), making sub-surface communication possible, (ii) the Earth-ionosphere waveguide attenuation rates for global VLF propagation are low — on the order of 0.5 to 2 dB/Mm [*Ferguson and Snyder*, 1980; p. 7], and (iii) electrically short monopole antennas with ground planes are feasible with relatively high efficiency ($\sim$50%) providing for radiated power levels of $\sim$100 to $\sim$1000 kW [*Watt*, 1967, p. 23]. At even lower frequencies in the ELF range, radiating structures for efficient transmission become prohibitively large (more than

Call Letters	Location	Frequency (kHz)	Power (kW)	Latitude (N)	Longitude (W)
NPM	Lualualei, Hawaii	21.4	480	38°59′	76°27′
NAA	Cutler, Maine	24.0	750/1000	44°39′	67°17′
NLK	Jim Creek, Washington	24.8	192	48°12′	121°55′
NAU	Aguadilla, Puerto Rico	40.75	100	12°25′	67°09′

Table 2.1: VLF and LF transmitters used in this work

a square kilometer in area) [*Watt*, 1967, p. 14], and the few available transmitters radiate much lower power levels [*Kim and Muehldorf*, 1995; p. 150].

The four VLF transmitter signals used in this work are listed in Table 2.1. Each of these transmitters operates continuously (with the exception of maintenance down time, typically less than several hours per week), and normally transmit data at a bit rate of r_b =200 bits/second using minimum-shift keying (MSK) modulation.

MSK, also known as continuous phase frequency-shift keying (CPFSK), consists of mark and space frequencies offset from the carrier center frequency, but with phase continuous boundaries. The frequency offset is one fourth of the bit rate ($f_\Delta = r_b/4$), which in our case is 50 Hz since $r_b = 200$ bits/second. Assuming the message bits to be independent and identically distributed, the low pass equivalent spectrum is given by (see *Carlson* [1986, pp. 522–525]; *Shafer* [1994]):

$$G_{lp}(f) = \frac{16}{\pi^2 r_b} \left[\frac{\cos(2\pi f/r_b)}{(4f/r_b)^2 - 1} \right]^2 \tag{2.1}$$

In the top panel of Figure 2.1, simulated MSK spectra are shown for the three transmitters used in this study in the 20–30 kHz band, assuming equal amplitude for the signals. In this example, the NAA and NLK signal bands begin to overlap at ∼35 dB below the maximum power level, thus limiting the possible dynamic range for demodulation. In the bottom panel of Figure 2.1, the power spectrum from a one second period of data recorded at Stanford University shows the characteristic MSK spectral shape of the three transmitters used in this work. A fourth transmitter signature can be seen at 25.2 kHz, and is due to a new VLF transmitter which began
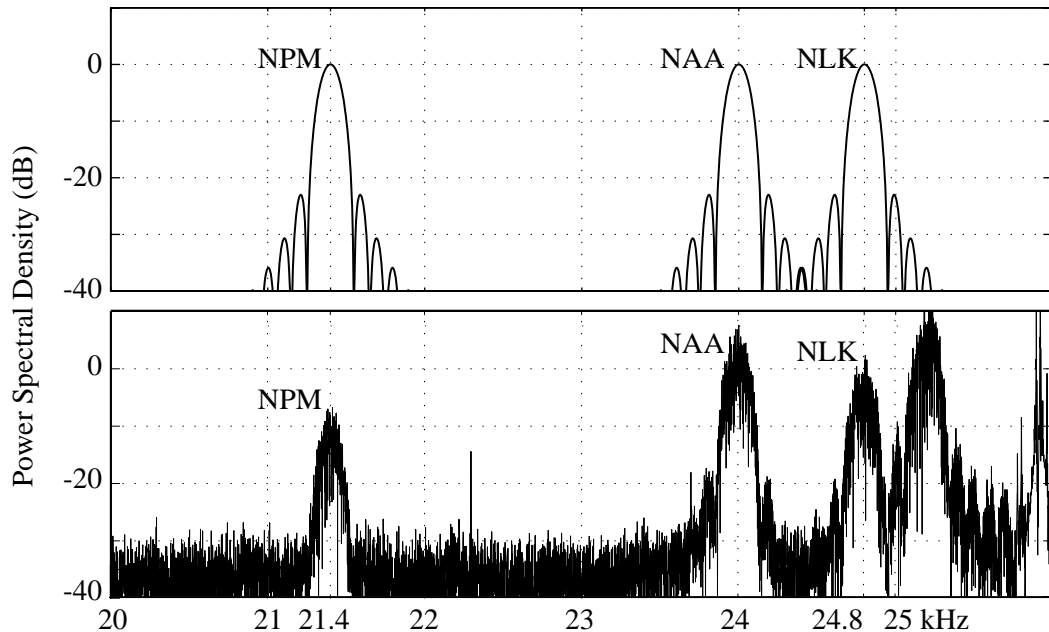
Figure 2.1: Measured and modeled minimum-shift keying (MSK) spectra. The top panel shows the ideal MSK spectra for three of the VLF transmitters. The NAA and NLK transmitters have center frequencies within 800 Hz, and show cross modulation 35 dB below the maximum power level. In the bottom panel, an example spectrum shows the relative power levels as measured at Stanford University, and reveals a fourth VLF transmitter that was added in early 2000.

operation in North Dakota in early 2000 [*E. Kennedy*, private communication].

2.2   VLF Receiving System

2.2.1   Analog Front End and Digitization

The VLF receiving systems used in this work typically consist of a single loop antenna used to sense the magnetic field of the subionospherically propagating electromagnetic signal, an analog front end for signal conditioning, and a digital PC-based real time demodulation of the amplitude and phase of up to six VLF transmitters. A system overview is shown schematically in Figure 2.2, and the individual components are described below.

Magnetic loop antennas are used because of their superior immunity to interference, favorable broadband noise figure, and ease of calibration as compared with
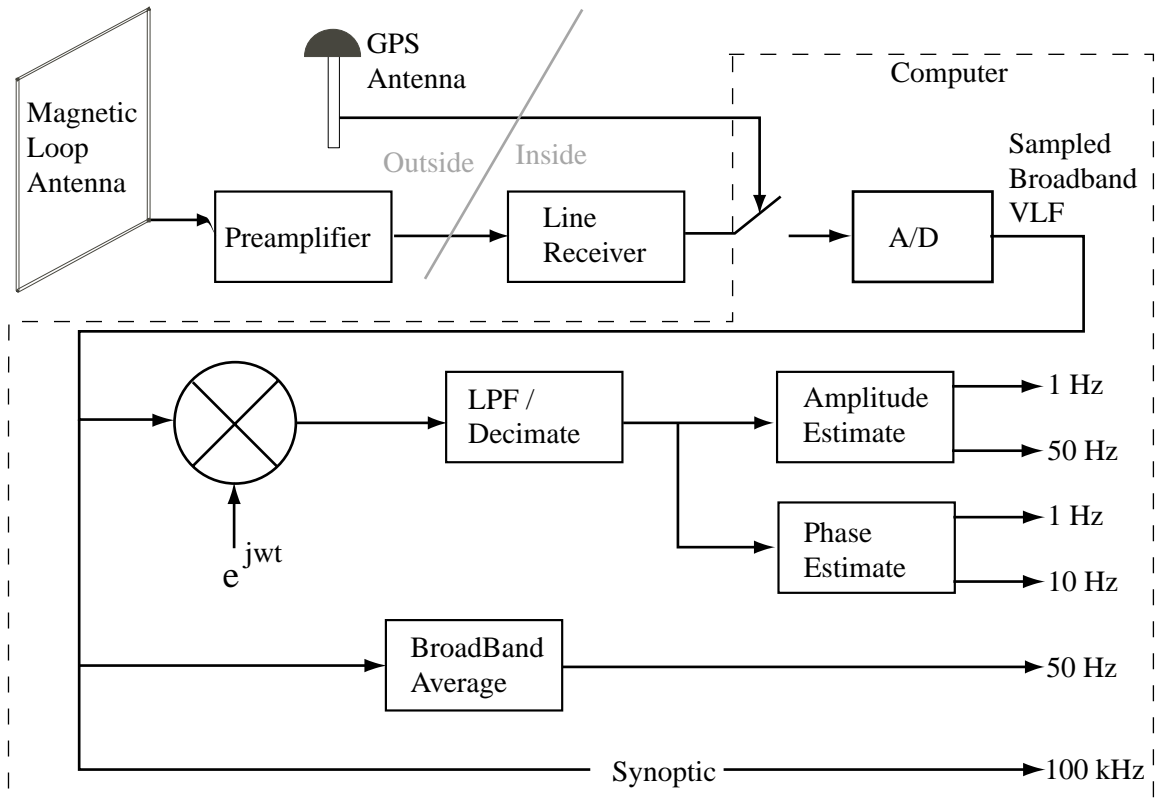
Figure 2.2: VLF receiver block diagram. The VLF signals were received with a magnetic loop antenna and then amplified, filtered and sampled by a 16 bit A/D card. Timing was based on a GPS reference. Once digitized, the broadband VLF was mixed down by each of the four VLF transmitter center frequencies, filtered and decimated, and then the amplitude and phase was calculated and archived. The data was then transmitted to Stanford University by automatic FTP each day.

electric field antennas. The antenna used in this system is 1.7 x 1.7 m^2 with a 1 Ω, 1 mH input impedance [*Paschal*, 1988]. It consists of 11 turns of ♯16 AWG wire, tightly wrapped in a square formation around two crossed aluminum bars, and is typically secured upright in a specific orientation by guy ropes. The voltage induced at the terminals of the loop is fed into an impedance-matched input transformer.

The measurements reported in this thesis were made with two different types of VLF front-end receivers. The "TVLF", or Tunable Very Low Frequency receiver, consists of an analog front end as well as modules for analog amplitude and phase demodulation. Its front-end was designed to connect directly to the antenna with up to ∼70 meters of coaxial cable. In order to allow more flexibility in the antenna

deployment location, the so-called "HAIL" front-end system was designed with a preamplifier and line receiver, capable of operating with a ∼2000 feet coaxial cable run. Both systems had a passband of ∼9–43 kHz and had a clipper circuit limiting the analog output to a ±3.5 V range. While the TVLF and HAIL front-ends differ in design and capability, they were deployed according to their design specifications. Consequently, each of the receivers used in this work had negligible noise figures compared with the atmospheric and external VLF noise environment.

The output of the analog front-end system, typically set to be ∼1 V peak-to-peak, was digitized and processed in real time. Acquisition timing was derived from a Global Positioning System (GPS) timing receiver[1]. Each second, the time was read through a serial communication port, with a delay of several hundred milliseconds. When the second preceding the scheduled start time was detected, an input trigger on the 16 bit analog to digital converter[2] was enabled. Once this trigger, connected to a 1 pulse-per-second output from the GPS receiver, was activated, data acquisition began within 1 μs of the scheduled start time. Individual samples were subsequently acquired at times corresponding to the rising edge of a GPS based 100 kHz square wave. The streaming 16 bit samples were double-buffered and transmitted each second to the processor.

The digital broadband data was mixed down to baseband (i.e., the signal spectrum was downshifted by the center frequency of each of the VLF transmitters), resulting in four complex data streams subsequently used for amplitude and phase demodulation. In view of the relatively small bandwidth (∼300 Hz) of the MSK modulated signals, each complex data stream was filtered and decimated by a factor of 1000 (to a new sample rate of 1 kHz). Because the output of a finite impulse response filter depends only on previous inputs, it was necessary to calculate the filtered output only for the desired 1000 output samples per second. Due to the relatively small MSK bandwidth with respect to the initial sample rate (100 kHz), and the need to have greater than 30 dB of rejection at frequencies only 400 Hz from the center frequency, a digital filter

---

[1]TrueTime XL-AK 601-101-035.
[2]National Instruments PCI MIO 16XE-10.
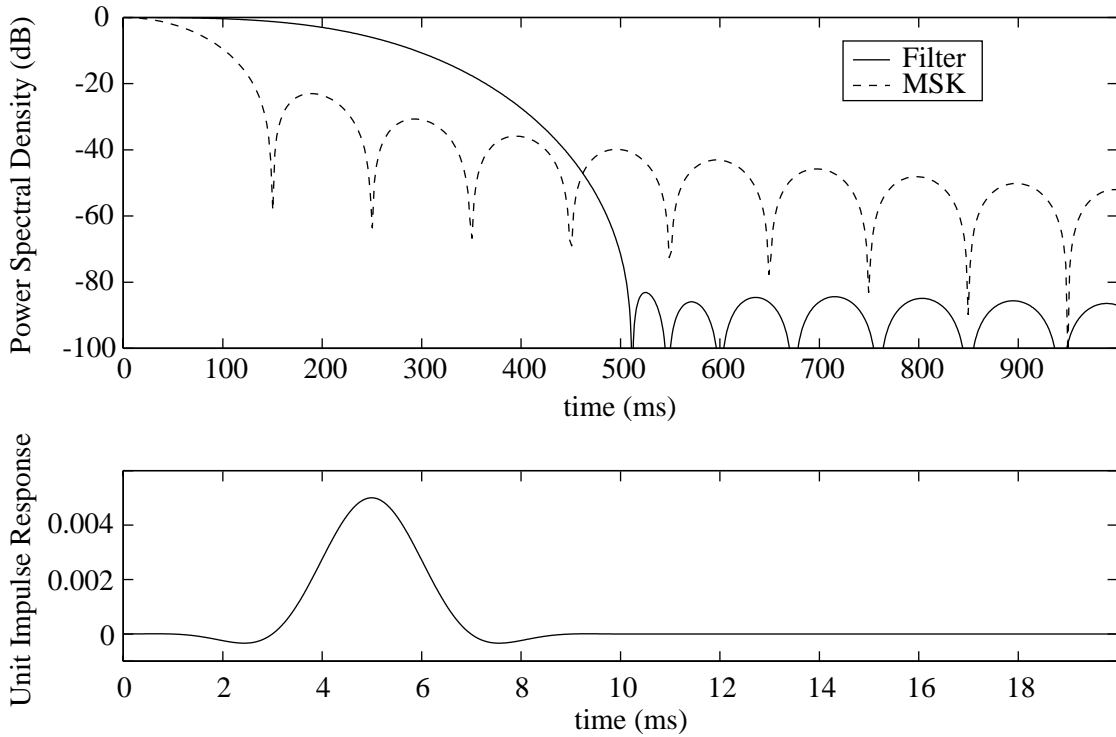
Figure 2.3: Digital filter response. The top panel shows the power spectral density of an ideal MSK signal superimposed upon the frequency response of the FIR filter used to isolate individual transmitter signals. The filter provided >80 dB of isolation for frequencies greater than 500 Hz, and ~30 dB of rejection 400 Hz from the center frequency. The lower panel shows the filter's impulse response with delay a factor of four smaller than the ultimate 20 ms sample rate.

using a Kaiser window with β of 8 (the β parameter affects the sidelobe attenuation levels of the Fourier transform of the window) and 1000 taps was selected[3] [*Kaiser*, 1974], the frequency response of which is shown superimposed upon the MSK power spectral density in Figure 2.3. The impulse response of this filter illustrates a ~5 ms delay, which is less than the 20 ms time resolution of our recorded data, and thus does not significantly affect data integrity.

As shown in Figure 2.2, the digitized signal could be additionally used to continuously measure a broadband average of the incoming signal in order to monitor sferic

---

[3]At the time of implementation, real time processing of four transmitters required a filter with no more than ~1000 taps. None of the channels used in this work significantly interfered with one another, but a new 25.2 kHz channel apparent in Figure 2.1 may significantly affect the demodulated amplitude and phase of NLK (and vice versa), so a longer and more narrow filter is suggested for future designs.

activity. In parallel with estimation of the amplitude and phase narrowband trans-
mitter signals, the broadband VLF data was rectified and averaged to the same 20
ms sample interval as the amplitude channel, giving an indication of the occurrence
time and relative strength of different sferics. This data stream is referred to in later
chapters as the "sferic channel".

The data acquisition code also provides the ability to save broadband snapshots
(as shown in Figure 1.3) at synoptic intervals. While such snapshots are not routinely
acquired, this capability proved useful for field site installation and occasional remote
system diagnostics.

2.2.2 Amplitude and Phase Demodulation

In this section, we describe the method used to estimate the average amplitude and
relative phase of the VLF transmitter signals after they have been shifted down to
baseband.

The complex baseband signal for MSK modulation can be thought of as a pha-
sor which ideally rotates by $\pm 90°$ for each bit. The amplitude of the transmitter
signal is defined by the phasor's vector length ($\sqrt{A_{\mathrm{real}}^2 + A_{\mathrm{imag}}^2}$). A 0.5 s example of
amplitude demodulation is shown in Figure 2.4. For the case shown, the normalized
broadband signal containing several sferics has an amplitude of ~ 1 unit peak-to-peak.
The real and imaginary components which result from downconverting the signal by
the carrier center frequency (NLK at 24.8 kHz) are shown in Figure 2.4b and 2.4c
respectively. The phasing relationship between the components is described in the
rest of this section, but the magnitude of their vector sum (i.e., signal amplitude) re-
mains approximately constant as shown in the bottom panel. This amplitude signal
was averaged by a variable amount (20 ms in this work) and saved to disk. A low
resolution (1 s averaged) output was also computed in real time, and saved separately
for use in cursory analysis.

The VLF phase measurement used in this thesis was computed from the phase
difference between the received phase and an estimate of the transmitted phase. In
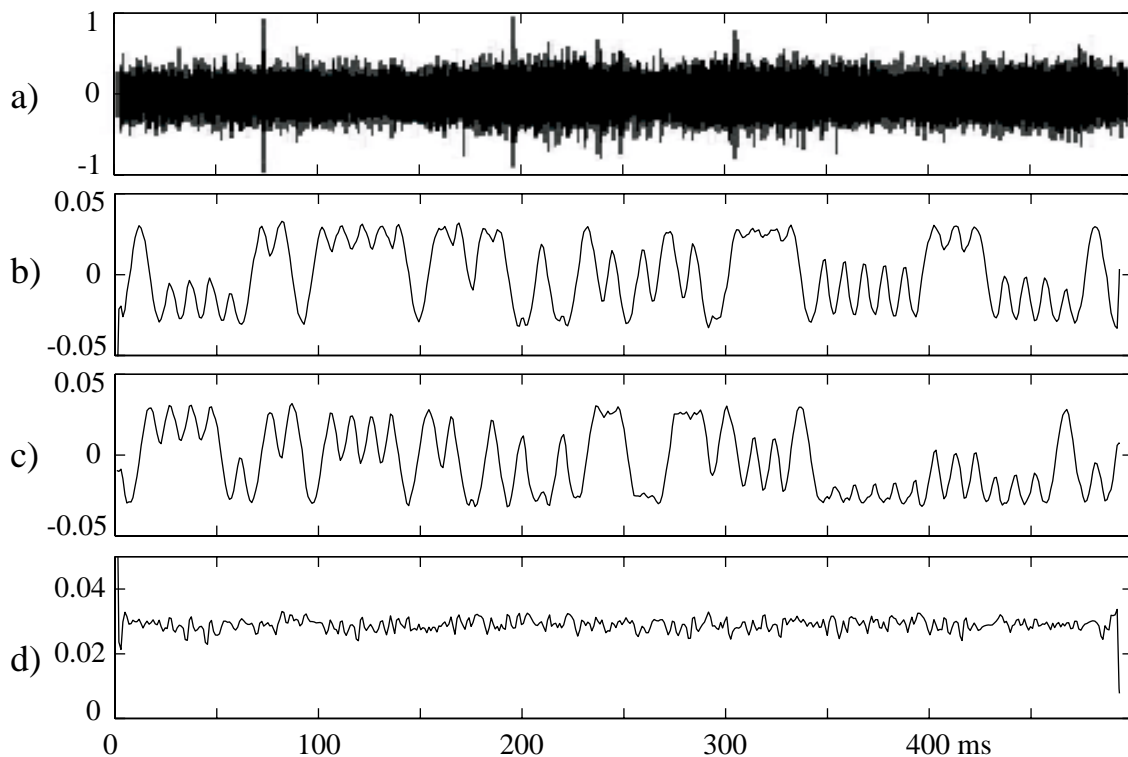
Figure 2.4: Amplitude demodulation example. (a) A normalized example of a 500 ms broadband record recorded at Stanford University. (b) The real component of the NLK signal after being mixed down to DC and filtered. (c) The imaginary component. (d) The amplitude of the complex signal.

past Stanford work [*Wolf*, 1990], the time-averaged phase measurement was obtained with an analog phase-locked-loop circuit, using an external temperature-controlled oscillator for the phase reference. In our work, the baseband signal was used to estimate the transmitted bits, which were then used to reconstruct an estimate of the sequence of transmitted phase from which an instantaneous phase difference measurement was made. This method of MSK phase determination is similar to that used by *Shafer* [1994]. Although no frequency source is shown in the new digital acquisition scheme (Figure 2.2), a phase reference is implicit; the sample acquisition triggers were derived from the GPS clock, making the GPS time itself the reference. Because the U. S. Navy VLF transmitters also used this same time source for modulation, the demodulation is frequency locked.

Phase of the baseband MSK signal is defined by the four-quadrant inverse tangent
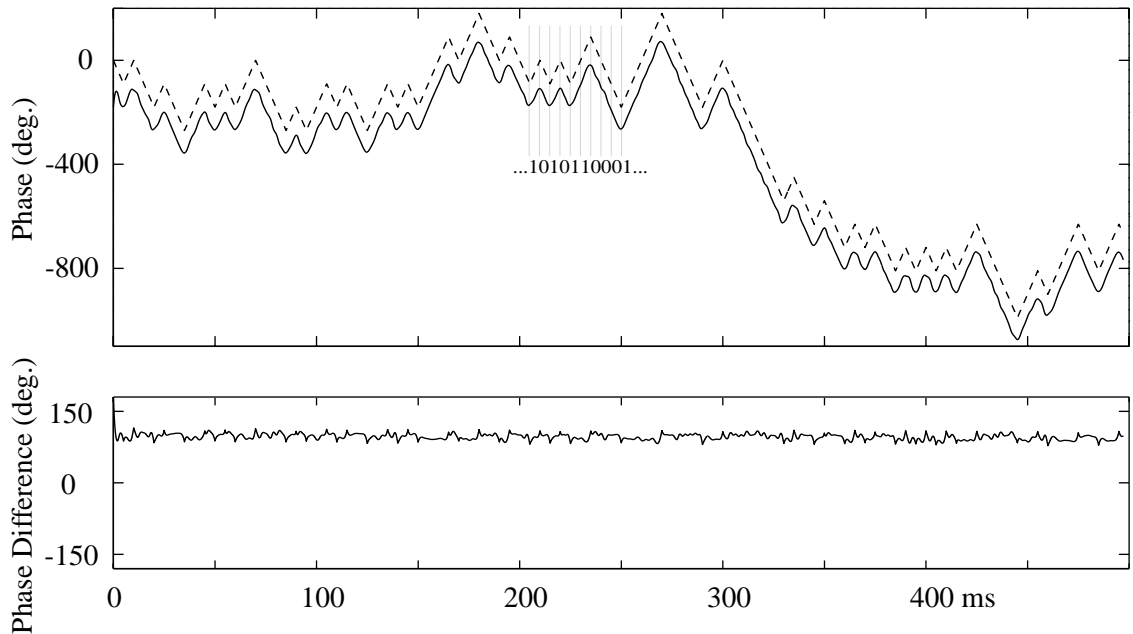
Figure 2.5: Phase demodulation example. The top panel shows the measured and reconstructed phase for the 500 ms NLK example from Figure 2.4. A phase increase by 90 ° represents a logical "1" while a decrease represents a logical "0".

of the real and imaginary components. An example of MSK phase at baseband, corresponding to the same 500 ms data segment shown in Figure 2.4, is shown as the solid line in Figure 2.5. When a logical "1" is transmitted, the carrier frequency increases by f_Δ, causing the phase to increase (with respect to a reference at the center frequency) by 90° over the duration of the bit. Likewise, transmission of a logical "0" results in a linear decrease in phase of 90°. In the case of Figure 2.5, the identification of each bit is unambiguous.

Aside from phase advances and decreases representing the message bits, there are two other characteristics of the baseband phase signal to consider. First, because the VLF transmitters do not require that a bit starts at the beginning of a second, an estimate of the bit transition time (in general different for the four transmitters and for each transmitter during each transmission episode) is needed. An estimate of this bit transition time can be found by first computing a histogram of the times at which there are inflections in the received phase signal (modulo the bit duration), and selecting the most common time from the distribution [*Shafer*, 1994]. Secondly, due

to the propagation delay between the source and the receiver, there is an initial phase difference between the received and simulated phase signals. Because the absolute value of the signal phase is not of interest in the present study (we are interested in transient ionospheric disturbances exhibited as a "change" in phase), this initial relative phase shift was arbitrarily set during each data acquisition episode.

Once the bit transition time and phase offset are selected, the signal can then be demodulated by calculating the average phase slope for each bit duration, and assigning binary bit values based upon the sign of each of the averages. An estimate of the transmitted phase signal can then be constructed with piecewise linear phase segments which either increase or decrease in phase by 90° over a bit period, an example of which is shown as the dashed line in Figure 2.5. The difference between the received phase and the reconstructed estimate of the transmitted phase is shown in the bottom panel of Figure 2.5, and is relatively constant over the 500 ms duration.

The real-time phase demodulation method utilized in this work was realized using a least-mean-squared adaptive filter method[4]. This real time algorithm first calculates the four-quadrant inverse tangent of the real and imaginary component of the baseband signal. Rather than unwrapping the phase, as was done in Figure 2.5, the phase is left in the ±180° range. The reference phase path consists of segments from four adjacent triangle waveforms, as shown with solid lines in Figure 2.6. The bit transition time and phase offset, unknown at the beginning of data acquisition, are modeled with three variables. Two of the variables are used to model the bit transition time, corresponding to a shift along the time axis of the triangle waveforms. In the real time algorithm, the triangle waveform is approximated to first order by a sinusoid, with phase being determined by the addition of a weighted sine and cosine wave. The phase offset, corresponding to a shift along the phase axis, is parameterized by the third variable. Those three variables are adjusted to minimize the least-mean-squared error between the received and constructed phase paths. The rate at which convergence occurs is determined by a parameter in the least-mean-squared

---

[4]This was initially reported in an unpublished Stanford course project paper entitled "Tracking and decoding an MSK signal using an LMS adaptive filter" by J. M. Dicarlo (1998).
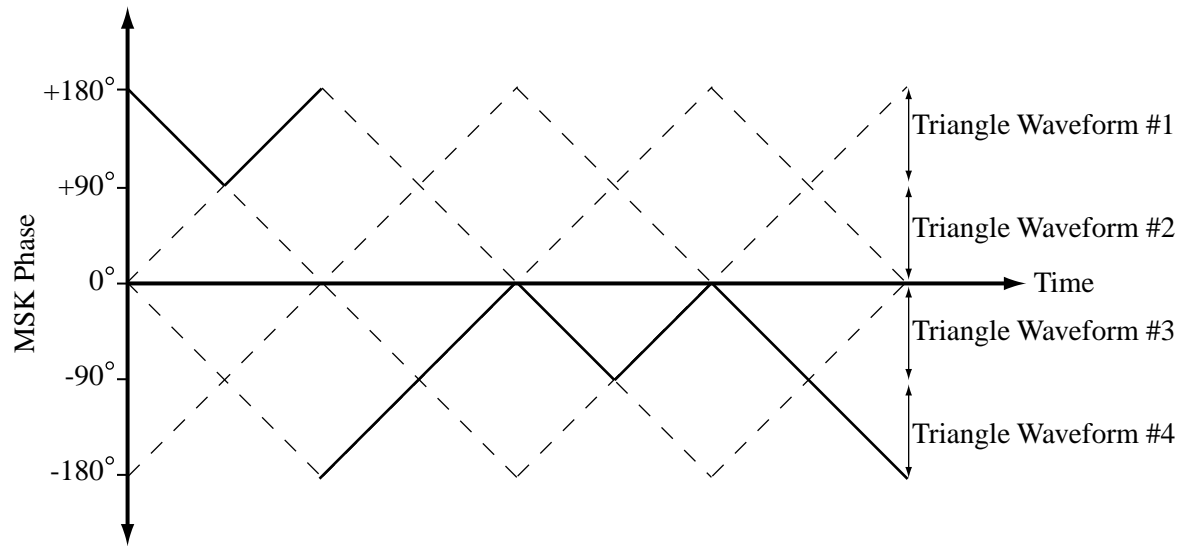
Figure 2.6: Ideal MSK phase example. For an eight bit period, all possible MSK phase paths are shown (assuming a constant bit transition time and no phase offset). An MSK path is composed of individual segments of four adjacent triangle waves. The example phase path shown in bold represents a "01110100" bit sequence.

algorithm, which is experimentally chosen so that convergence occurred in the first ~100 seconds of acquisition. The variables are not allowed to change after convergence due to two factors: (i) the bit transition time is typically found to be constant for the entire night, given the GPS timing reference, and (ii) the actual phase path will diverge from the theoretical phase path due to diurnal trends and perturbations caused by ionospheric effects — the intended measurement. During data acquisition, the difference between the measured phase and this calculated phase path is averaged and recorded with high resolution at 100 ms and low resolution at 1 s.

2.3   The HAIL Array

The key scientific contributions (see Section 1.4) reported in this dissertation were obtained via the use of multiple VLF receivers as described above in a nine-element holographic configuration that enabled the first definitive quantitative assessment of

the spatial extent of the transient ionospheric disturbances produced by lightning discharges. In this section, we describe this holographic array, known as the Holographic Array for Ionospheric/Lightning research (HAIL). We begin this section with a discussion of several publications detailing previous measurements of lightning-induced D region ionospheric disturbances, which motivated the deployment of an array of VLF receivers. The configuration and typical operation of HAIL are then discussed, followed by an example and description of typical data.

Past research motivating the establishment of the HAIL array includes: (i) experimental observations of the VLF scattering pattern of ionospheric disturbances, and (ii) theoretical modeling efforts aimed at the interpretation of the measured scattering pattern in terms of the causative disturbance location, size, and shape. *Dowden and Adams* [1990] measured the phase difference between scattered VLF signals at two receivers 8.86 km apart in an attempt to determine the arrival angle of the scattered signal. Their method relied on the independence of VLF phase with respect to the scattering angle, distance to the scatterer, and disturbance size; assumptions which were subsequently shown to be false [*Poulsen et al.*, 1993a]. Using several non-uniformly oriented great circle paths from multiple transmitters, *Inan et al.* [1990] used the absence or presence of perturbations on crossing and nearby paths to determine crude spatial resolution and event location. *Lev-Tov et al.* [1995] used a three-dimensional numerical model along with measurements of amplitude perturbation magnitude, and found that the observed LEP perturbations were likely less than 250 km in lateral extent. The need for a holographic measurement of the lateral extent of ionospheric disturbances of the early/fast type became evident as a result of findings that VLF events were only observed when causative lightning discharges occurred within ± 50 km of the great circle VLF propagation path [*Inan et al.*, 1993], a fact which was used to infer that the lateral extent of the disturbances was $\sim$100–150 km [*Inan et al.*, 1996a].

Chen et al. [1996] introduced the technique of VLF strip holographic imaging using the *Poulsen et al.* [1993a] propagation and scattering code, providing the means

NLK
(24.8 kHz)

NAA

(24.0 kHz)

Cheyenne, WY
Ft. Collins, CO
Boulder, CO
Parker, CO
Co. Springs, CO
Pueblo, CO
Walsenburg, CO
Trinidad, CO
Las Vegas, NM

to NPM
(21.4 kHz)

to NAU
(40.75 kHz)
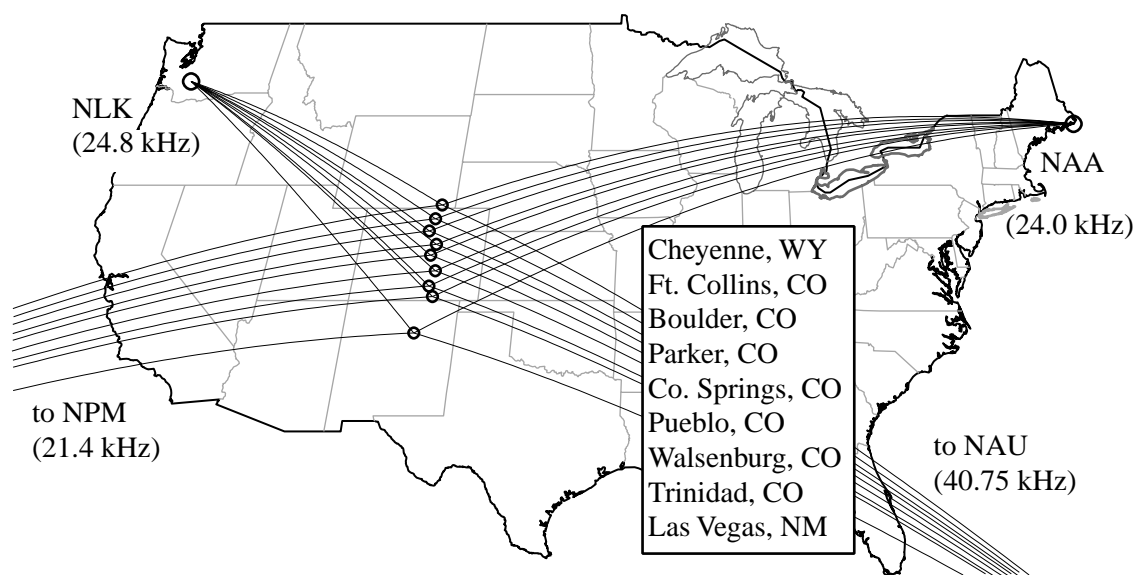
Figure 2.7: The Holographic Array for Ionospheric/Lightning research (HAIL). A map showing the locations of the HAIL receivers and the great circle paths to the VLF transmitters used in this work.

to simply relate the scattered signal pattern along a suitably spaced array to the location and size of the disturbance, albeit only for a single waveguide mode case. The single mode results of *Chen et al.* [1996] provide insight for cases when receivers are not located nearby a null of the transmitted signal for the ambient ionosphere electron density profile selected. In order to fully recover the lateral extent of an assumed Gaussian ionospheric density disturbance located along a ∼4 Mm long great circle path of propagation, *Chen et al.* [1996] found that VLF receivers needed to be located transverse to the direction of propagation with an inter-station spacing of ∼50 km.

The currently deployed HAIL array consists of nine VLF receivers in the midwest, shown in Figure 2.7 with great circle paths from the four VLF transmitters used in this work to the receivers. The known occurrence of intense summer midwestern lightning storms, particularly those in eastern Colorado, Nebraska, and Kansas, influenced the decision to deploy the array along the "Front Range" of the Rocky Mountains. In the early summer of 1997, TVLF analog receivers (see Section 2.2.1), along with the HAIL demodulation software, were deployed at five locations from Ft. Collins, Colorado to

Location	Symbol	Latitude (N)	Longitude (W)	Receiver Type
Cheyenne, Wyoming	CH	41°01′	104°48′	HAIL
Fort Collins, Colorado	FC	40°33′	105°02′	TVLF
Boulder, Colorado	BO	40°01′	105°16′	HAIL
Parker, Colorado	PA	39°26′	104°45′	TVLF
Colorado Springs, Colorado	CS	38°58′	104°59′	HAIL
Pueblo, Colorado	PU	38°17′	104°35′	TVLF
Walsenburg, Colorado	WA	37°38′	104°48′	HAIL
Trinidad, Colorado	TR	37°10′	104°31′	TVLF
Las Vegas, New Mexico	LV	35°36′	105°13′	TVLF

Table 2.2: HAIL receiver locations

Las Vegas, New Mexico, with ∼130 km spacing. During the summer of 1997, tens of days with hundreds of events were observed, but the spatial sampling was not adequate for fine resolution of the spatial extent of the disturbances. The following summer, four more stations with the new HAIL analog front-end were added, for a total of nine receivers with ∼65 km spacing (except for the longer spacing to the southernmost receiver).

Table 2.2 gives a summary of receiver location and type. Throughout this work, transmitter-receiver paths are identified by the transmitter call sign followed by the two letter station identifier (e.g., NLK–FC). As will be shown in Chapter 3, the chosen spacing provided adequate resolution to quantitatively determine the size of individual early/fast disturbances.

A technological milestone which allowed the successful deployment and operation of nine stations with high reliability was the expansion of Internet access to high schools, regardless of location. Automatic data transfer to Stanford facilitated remote station maintenance because no action was required by default. Intervention was necessary only when a station failed to transmit normal data. Remote operation control was made possible by programming the data acquisition software to read an initialization file each second. This file, containing variables such as start and stop times, data resolution, and broadband acquisition, was occasionally updated from Stanford when a change was necessary.

HAIL data was typically acquired nightly during 01:00 to 13:00 UT, covering the time of nighttime propagation ranging from Maine (NAA–HAIL) to Hawaii (NPM–HAIL) for much of the year. Sferic channel recordings were made at the CH, CS, and LV stations. Amplitude data was sampled at 1 s and 20 ms, while phase data was sampled at 1 s and 100 ms, all samples saved as 16 bit integers in a Matlab format, resulting in a daily quantity of data of ~20–25 MB per station.

Data from the National Lightning Detection Network (NLDN) provides the time, location, polarity, and peak current of most cloud-to-ground lightning discharges that occur in and around the continental United States [*Orville,* 1994], and is used in this work to identify the discharges associated with VLF perturbations observed in HAIL data.

An example of the recorded amplitude data for 1 August 1998, showing typical diurnal changes as well as local and atmospheric noise conditions, is shown in Figure 2.8. Several typical signal characteristics observed in this data are noted below.

- At ~07:30 UT, the NPM–HAIL signal levels all decrease to nearly zero (Event A). This is indicative of a brief signal interruption at the transmitters.

- Slightly later than ~01:00 UT, the signal level of all transmitters at WA decreases to zero (Event B). Likewise, the signal level at PA decreases at ~11:00 UT (Event C). These signal dropouts are due to a data acquisition restart, which causes an ~2 minute lapse in data.

- The signal-to-noise ratio varies considerably for the range of transmitter–receiver paths, due to the varying orientations of the magnetic loop antennas and the different transmitter power levels, but also due to the different ambient electromagnetic noise levels at the sites. As an example, the NLK–BO amplitude is substantially noisier than the NLK signal at the other sites, although the transmitter is the same and the antenna orientations are not substantially different.

- Multiple mode propagation effects are clearly manifested as large amplitude changes as the day/night terminator crosses the great circle path [*Crombie,*

1964], labeled as "sunset" and "sunrise" in Figure 2.8.

- Multiple mode propagation effects are also evident (in some cases) for a transmitter signal measured along the receiver array. Typically, VLF signals propagate with less attenuation during nighttime due to much lower ionization levels in the D region [*Wait*, 1957]. For a primarily single mode signal, the nighttime amplitude should be larger than that during the day, as it is with the NAA–HAIL amplitude signals. However, multiple modes exist for receivers relatively close to the transmitter (<5000 km), and can destructively interfere, making the nighttime amplitude lower than that during the day. As an example, the NAU–LV amplitude signal has a higher nighttime than daytime amplitude, the NAU–CH station has a similar daytime and nighttime amplitude, and the NLK–CH station has a lower nighttime than daytime amplitude.

- Large radio atmospherics, especially when they occur at high rates (due to lightning flash rates) are sometimes evident in 1 s averaged amplitude data, particularly when the source thunderstorm is nearby (<1000 km), and when the received transmitter field strength is relatively low (such as when a transmitter is turned off or when the receiver is in a null). In Figure 2.8, large sferic impulses are particularly evident on the northern NAU–HAIL amplitude signals, earlier in the night, when a large thunderstorm (located West of the HAIL array, ranging from Mexico to Canada) was active.
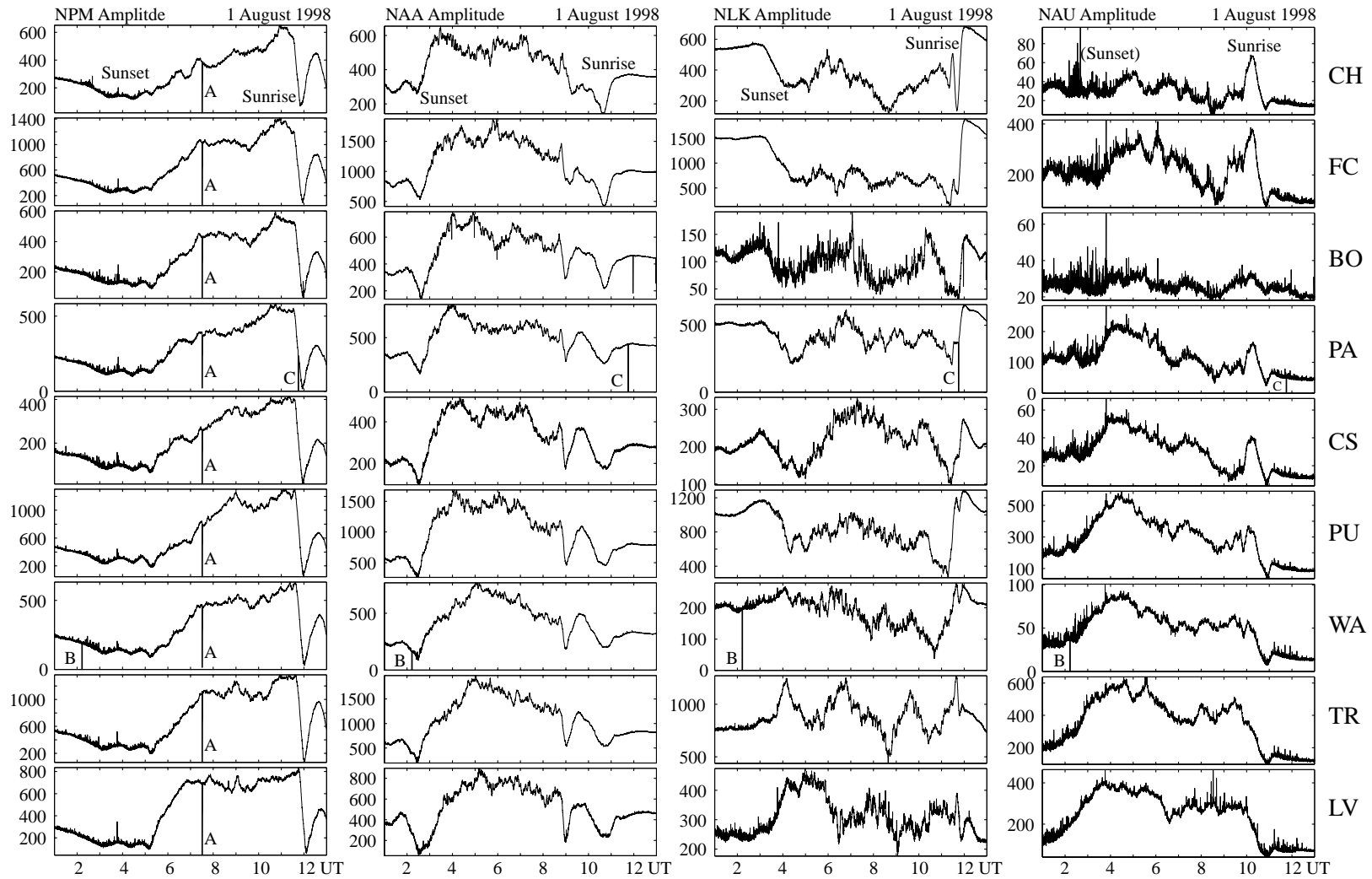
Figure 2.8: HAIL amplitude data for 1 August, 1998. Received VLF Amplitude is plotted with linear arbitrary units (with zero representing the absence of signal) for the four VLF transmitters used in this work.

Chapter 3

Early/Fast VLF Events

"Early/fast" VLF events are characteristic changes in the amplitude and/or phase of a subionospheric VLF signal that result from a lightning-induced conductivity change in the lower ionosphere. The event signatures exhibit a rapid onset (<20 ms, i.e., "fast") followed by a relatively slow recovery (typically 10 to 100 s) and occur within 20 ms of a causative cloud-to-ground (CG) lightning discharge (i.e., "early") [*Inan et al.*, 1993]. In this chapter, we describe and interpret new observations of early/fast VLF events made with the HAIL array. The results presented in Sections 3.1 and 3.2 were originally published as a journal article [*Johnson et al.*, 1999a], and involve the comparison of the measured scattering patterns of associated ionospheric disturbances along the HAIL array with those predicted for ionospheric disturbances with a variety of lateral extents, using a 3D model of VLF propagation and scattering in the Earth-ionosphere waveguide. In Sections 3.3 and 3.4, the nature of the lightning associated with these events is shown to be consistent with bursts of intracloud (IC) lightning accompanying a cloud-to-ground lightning discharge [*Johnson and Inan*, 2000]. In Section 3.5, we present early/fast VLF event occurrence statistics for a two month period, and comment on the correlation of event onsets with occurrence patterns on cloud-to-ground lightning discharges.

3.1   Early/Fast VLF Event Signatures

The direct effects of lightning discharges on the conductivity of the overlying D region produces a characteristic VLF amplitude and/or phase perturbation signature that is unambiguously identifiable. Figure 3.1a shows a cross section of an earth-ionosphere waveguide path, with an ionospheric disturbance between the transmitter and receiver. In general, the disturbance can be laterally off the GCP between the transmitter and receiver as shown in Figure 3.1b. Figure 3.1c shows data for a three-minute time period illustrating rapid signal amplitude changes followed by exponential-like recoveries back to "ambient" (i.e., the signal level that would be in effect in the absence of the transient perturbation) signal levels (indicated by the dashed line) that often exhibit relatively slow variations during the night. A typical early/fast event onset (Figure 3.1d) is simultaneous (within one 20 ms sample) with the causative sferic (Figure 3.1e), constituting the impulsive signature of the causative lightning discharge. Early/fast VLF events are observed on a given VLF path only when the causative lightning discharge occurs within 50 km of the GCP from the transmitter to receiver [*Inan et al.*, 1993], a fact which has been interpreted to suggest that the disturbances have lateral extents of ~100 to 150 km [*Inan et al.*, 1996a].

We now present examples of early/fast event signatures observed during three different days in August 1998. On seventeen days in August 1998, HAIL data clearly show early/fast event activity on the NAA signal at one or more of the HAIL sites. Of these seventeen, ten days have records during which repeated (>10 in one hour) and clearly identifiable (>0.5 dB) early/fast events occur. Three half-hour records were selected on the basis of the event magnitudes decreasing to negligible levels at the northern and southern-most receivers and varied proximity of the causative lightning (200, 400, and 700 km) to the HAIL array.

For early/fast events, the associated CG discharge as identified in NLDN data is most often located nearest the particular HAIL paths with the largest amplitude
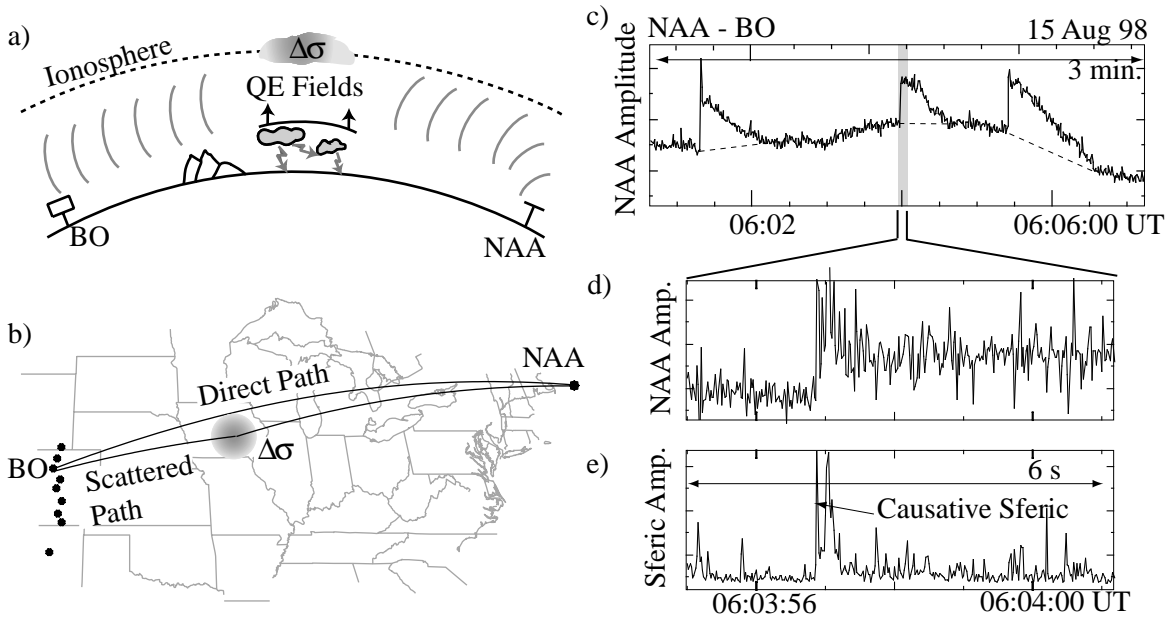
Figure 3.1: Early/fast event overview. The top two panels schematically illustrate the scale of the thunderstorm/ionosphere interaction region in an early/fast VLF event. A three minute record of the amplitude of the NAA transmitter signal received at the Boulder site (BO) shows three typical early/fast events which recover to pre-event levels in ~30 s. The middle event is expanded in panel (d) and plotted together with broadband sferic intensity (e) to show the simultaneity of the causative sferic with the event onset.

perturbations[1]. In each of the top panels of Figure 3.2, the locations of lightning discharges (which occurred during the time period corresponding to the amplitude record shown) are indicated. The region of lightning activity containing the time-correlated causative discharges is circled, and in each case these regions encompass the perturbed GCPs.

For each of the cases discussed below, a "scattering pattern beamwidth" was calculated. The pseudo-plane VLF waves incident on the ionospheric disturbance region are scattered, and the angular extent of the scattering is here described with a radiation power pattern in azimuth as measured from the center of the disturbance. For ionospheric disturbances which have Gaussian cross sections, the scattering pattern for a single waveguide mode contains one main lobe, which can be described with an

---

[1]In some cases, the particular mode structure of the VLF path nearest the associated CG is such that an adjacent path may have a larger event magnitude.

effective beamwidth [*Chen et al.*, 1996]. In this work, the beamwidth is calculated
with the following method: first, the geographic location of each receiver along the
array is converted into an azimuth as observed from the lightning discharge location
(which is presumed to be immediately below the center of the ionospheric distur-
bance). The perturbed amplitude and phase values are then converted into scattered
field magnitudes by a simple vector calculation [see Figure 1.4 and *Poulsen et al.*,
1993a]. The scattered field as a function of azimuth is then interpolated to find the
angular range around the peak in which the magnitude is within 15 dB of the peak.

CASE 1: 2 AUGUST 1998: Lightning activity from 05:00 to 05:30 UT was situated
about 500 km to the east of the HAIL array and spanned most of the NAA–HAIL
GCPs. Fourteen early/fast events identified as A through N in Figure 3.2a were
observed at PU, with some also seen at the adjacent sites. The causative lightning
discharges all lie within 50 km of the NAA–PU path. The average event amplitude
was ∼0.5 dB and the average event phase was ∼1°. The scattering pattern of the
ionospheric disturbance had a 15 dB beamwidth with an ∼18° angular width. Other
events which appear to occur simultaneously, such as B and K, are in fact distinct
events with onsets separated by several seconds, and are produced by discharges at
different locations.

CASE 2: 15 AUGUST 1998: Figure 3.2b shows data from 06:00 to 06:30 UT.
While there was lightning activity along HAIL paths in Nebraska, the events shown
originated from lightning located near the northeast corner of Colorado within the
circled region. Event O at 06:07:25 UT shown in Figure 3.2b and with high resolution
in Figure 3.3 was typical of the sequence and perturbed the NAA–FC and NAA–BO
signals with a 15 dB beamwidth with an angular width of <∼30°. Although event
P appears to be observed at 7 HAIL receivers, it is actually two separate events, P1
and P2.

CASE 3: 21 AUGUST 1998: The lightning activity in Figure 3.2c from 08:15 to
08:45 UT was approximately 700 km from the array in eastern Nebraska. Event Q at
08:27:40 UT in Figure 3.2c was typical of the sequence and perturbed only NAA–PA
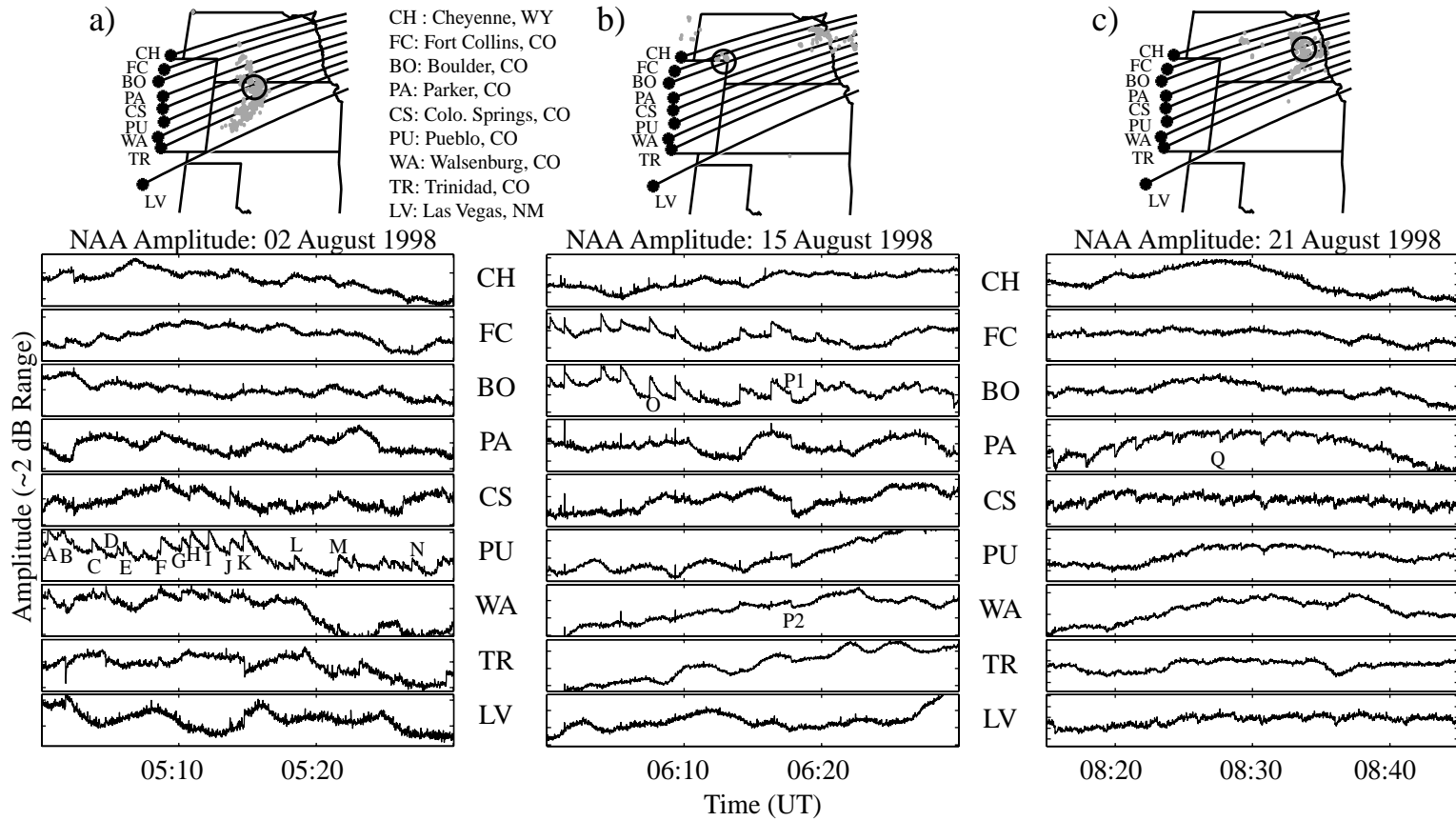
Figure 3.2: Early/fast event examples. Early/fast event sequences measured at HAIL sites on three days in August 1998. Although not shown, phase was also measured and showed similar perturbations. Lightning locations are plotted above, together with NAA–HAIL GCPs, corresponding to the time period of the amplitude record for each case.

and NAA–CS. For this event, the scattered signal projected a 15 dB beamwidth of 20°.

3.2 VLF Diffraction Pattern

The magnitude of the VLF early/fast amplitude and phase changes observed are determined by the directional scattering properties of the associated ionospheric disturbance, dependent primarily on its lateral extent. In this section, we quantitatively interpret the observed amplitude/phase changes in terms of the scattering pattern of the associated disturbance using a three-dimensional multiple-mode waveguide model of VLF propagation and scattering. As discussed in Section 1.2, this model accounts for the presence of localized D region disturbances using realistic parameters for the ground conductivity, the earth's magnetic field, and the altitude profile of nighttime ionospheric conductivity. Although the physical nature and the conductivity profile of ionospheric disturbances that produce early/fast VLF events remains in dispute [*Inan et al.*, 1996c; *Dowden et al.*, 1996b], the VLF scattering pattern of the disturbance is largely determined by its lateral extent [*Poulsen et al.*, 1993b; *Chen et al.*, 1996]. For our purposes, we use a disturbed electron density profile[2] producing a 20% enhancement in conductivity at 80 km, assumed to fall off as a Gaussian function of radial distance (i.e., as $e^{-(r/a)^2}$, where a is the disturbance radius). The assumption that the scattering pattern does not depend sensitively on the altitude profile is only valid if the unperturbed (ambient) signal does not exhibit a deep null located at the receivers. Both our measurements and our model calculations indicate that this is a good assumption for the cases studied.

The linear projected width of the main beam of the scattering pattern along the HAIL array is determined by the transmitter and disturbance locations, and the horizontal extent of the ionospheric disturbance. As discussed in *Chen et al.* [1996], two limiting cases of disturbance widths can cause this projected linear width to be

---

[2]The ambient profile used in this case is Profile R1 as seen in Figure 4.13 and the disturbed profile is Profile IV taken from [*Poulsen et al.*, 1993b].
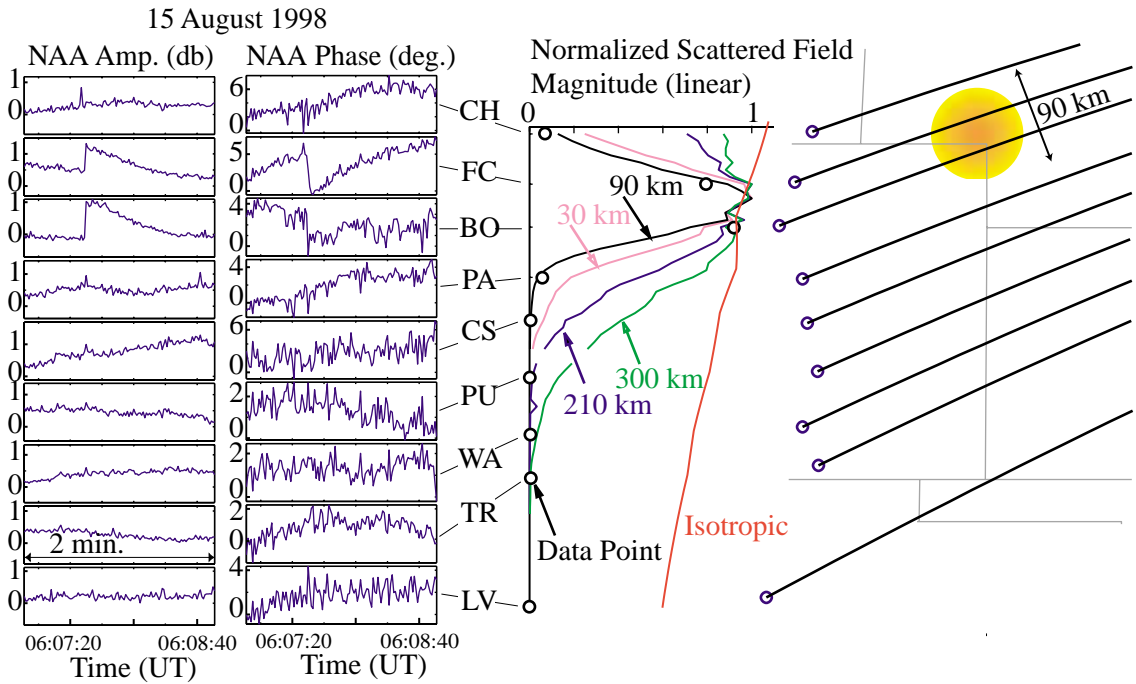
Figure 3.3: Early/fast event O. Measured and modeled disturbances along the HAIL array for event O. Amplitude and phase plots are shown as well as a map with the causative lightning location. The magnitude of the scattered field changes measured along the HAIL array are plotted (as circles), with modeled scattering patterns for ionospheric disturbances of several different extents. A predicted scattering pattern from an isotropic source is also shown for reference.

large. For narrow disturbance widths (< 50 km), the angular width of the scattering pattern increases with decreasing disturbance size diameter, becoming nearly isotropic for disturbances less than a wavelength ($\sim$15 km) in diameter (although such isotropic radiation scatters much less electromagnetic energy to a given receiver, making event detection less likely). At the other extreme, for relatively large disturbances (> 500 km) the projection of the scattering pattern along the HAIL array is large since the disturbance overlaps more of the VLF paths. For any given disturbance location, an ionospheric disturbance width thus exists at which the angular width of the scattering pattern is minimized, producing a beam highly focused in the forward direction.

Scattering patterns for Event O from Figure 3.2 are displayed in Figure 3.3 for disturbances of different Gaussian horizontal extents. The patterns have been normalized so that the beamwidths can be accurately compared, and normalized scattered
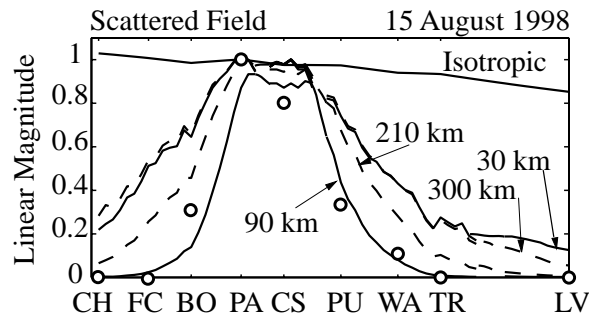
Figure 3.4: Early/fast event Q. Measured and modeled disturbances along the HAIL array for event Q.

field changes from the HAIL receivers are shown superimposed. The 90 km wide disturbance has a narrow main beam which fits the data more closely than the wide beam patterns associated with the larger (and smaller) disturbance widths.

Modeled scattering patterns for event Q from Figure 3.2, along with the normalized HAIL measurements, are shown in Figure 3.4. The causative CG for this case was located in the region circled in Figure 3.2c, $\sim$700 km from PA (along the NAA–PA path). Although the causative lightning in this example was quite distant compared to the August 15 case, the derived angular beamwidth is remarkably similar and the data points remain consistent with the 90 km disturbance curve. The slight lateral shift of the data points with respect to the modeled curves may be due to the difference between the lightning location and the center of the ionospheric disturbance [*Wescott et al.*, 1998].

3.3   Early/Fast Events and Sferic Clusters

An interesting question arises from the spatial distribution of lightning activity during 08:10 to 08:50 UT on 21 August 1998. With positive and negative lightning discharges occurring over regions covering most of the central HAIL paths, early/fast events might be expected to occur over many of these paths. The peak current of the causative discharges associated with early/fast events ranged from -24 to -64 kA and from $+18$ to $+52$ kA. During this period, there were 10 discharges with peak

current magnitudes greater than 64 kA that did not produce a VLF event, despite being located on a HAIL GCP. This observation suggests that characteristics of the lightning discharges other than the peak electric field as recorded by NLDN may be an important measure of the effectiveness of the lightning-ionosphere interaction, consistent with previous findings [*Inan et al.*, 1993]. In this section, we examine properties of lightning discharges that lead to "early/fast" VLF events and show that only those lightning events with bursts of intracloud (IC) lightning produce the early/fast type of ionospheric disturbances.

In past observations, early/fast VLF events have been identified by the fact that their onsets occur nearly simultaneously (within 20 ms) with lightning discharges measured as associated radio atmospherics and sometimes also as CG discharges identified in NLDN data [*Inan et al.*, 1996a; and references therein]. In many cases, the associated sferics were observed in narrowband VLF data as singular impulsive peaks, allowing the precise (within the data resolution of 20 ms) identification of the event onset and supporting the concept of the ionospheric effect being produced by a single discharge. Those early/fast VLF event flashes associated with NLDN data are found to be positive and negative, ranging in recorded peak current intensities from 20 kA to 180 kA [*Inan et al.*, 1996a]. However, many events were observed with no associated NLDN-detected CG flashes but nevertheless with clear impulsive sferic signatures, interpreted as possible evidence of intracloud flashes. One common feature of the early/fast observations reported in all but one of the previous papers has been that the associated sferics were observed at distances of >500 km from the lightning discharges in narrowband VLF channels tuned to known VLF transmitter signal frequencies. As a result, only the peak of the associated sferic which exceeded the transmitter signal level was observable.

In Figure 3.5, NLDN-recorded CG lightning and the corresponding amplitude records from the HAIL receivers are shown for 20-minute periods on two different days. On 15 August, several discharges located near the Northeast corner of Colorado occurred within 20 ms of early/fast events as recorded by two receivers with GCPs
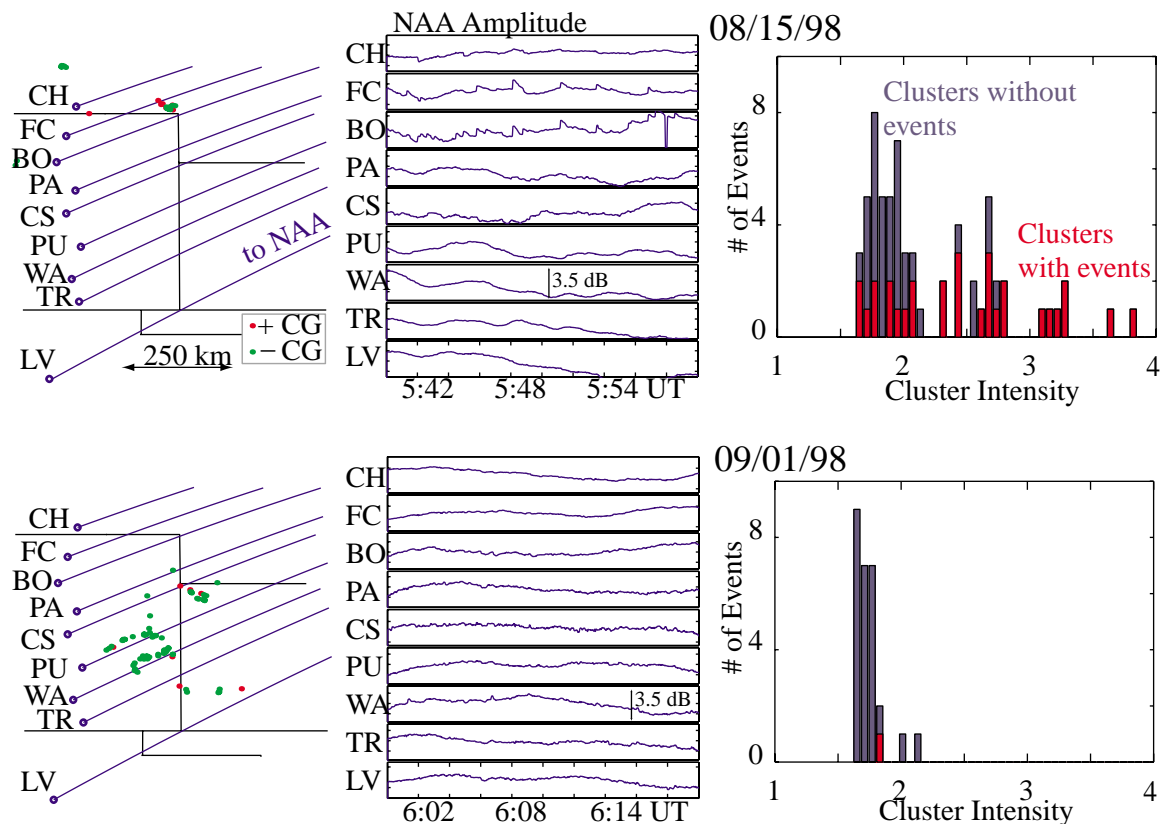
Figure 3.5: Example days with and without sferic clusters. The location of lightning discharges for 20 minute periods on two different days are shown, along with the amplitude of the NAA transmitter received at 9 sites (all shown with a 3.5 dB range). (a) On 15 August 1998, early fast events are observed at the CH, FC, and BO sites, and a histogram of cluster intensity shows large clusters that are preferentially associated with the events (histogram only shows clusters with more than 1.65 times the median sferic level). (b) On 1 September 1998, lightning occurring with similar proximity to the array does not show many large clusters or early/fast VLF events.

on either side of the lightning location. On 1 September, NLDN recorded a number of discharges with similar proximity to the array and similar peak currents, yet few early/fast events are observed.

Four early/fast events from the 15 August period as measured on the NAA–FC signal are labeled A–D in the top panel of Figure 3.6. Expanded views of these event onsets, spectrograms of the corresponding broadband data from YR, and the NLDN-recorded times of CG discharges are shown for each of the four events. Although the NLDN only recorded a CG at the onset of event D, each of the four events coincides
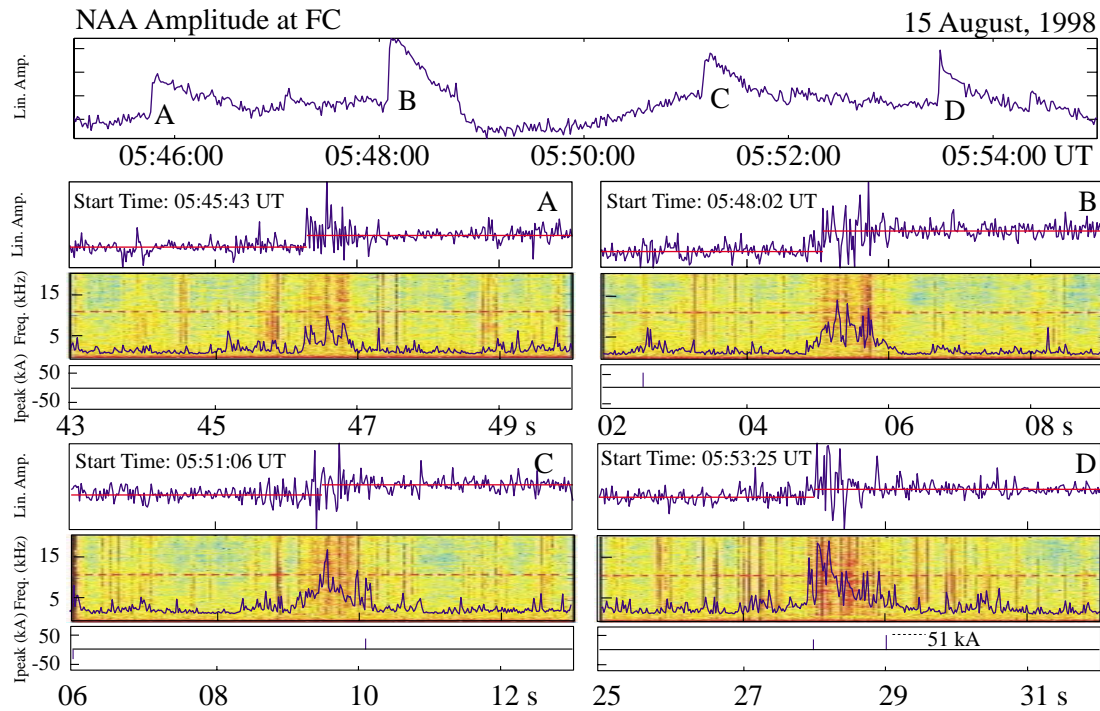
Figure 3.6: Four consecutive sferic clusters. Top panel shows a sequence of four early/fast events labeled A–D measured on the NAA–FC path. Each of the four event onsets is shown below with the NLDN recorded discharges and the associated broadband spectrogram showing the sferic clusters (with integrated signal intensity superimposed). Events A–C have sferic activity at the event onset, but do not have an associated CG, suggesting that intracloud lightning was causative.

with an unusually large cluster of sferic activity. In these and other cases of an event without an associated CG, we nevertheless assume that the locations of the causative sferics are within the same thunderstorm, based on the similarity of consecutive event signatures and sferic clusters.

Such large sferic clusters are found to occur predominantly in association with early/fast event onsets and may thus represent an inherent property of lightning episodes that produce ionospheric disturbances. In the 15 August case, this one-to-one association was observed to the degree that the early/fast VLF event onsets could be identified solely by inspection of the sferic data. In another case (not shown), during a period on 2 August 1998 from 05:00 to 05:30 UT, many hundreds of CGs of positive and negative polarity occurred within 500 km to the east of the HAIL array. During this period, only ~10 CGs were accompanied with sferic clusters (these were

all from a small area of the storm near the NAA–PU path), and these were also the only CGs associated with early/fast events measured primarily at the PU receiver.

As exemplified by the 1 September case in Figure 3.5, there are many more lightning CGs recorded by NLDN, and presumably many more IC discharges, than there are VLF events. During most periods of early/fast VLF event activity observed with the HAIL array, many NLDN-recorded CGs in a localized storm are not associated with VLF events — even if they occur within close proximity of one of the HAIL VLF paths, consistent with past findings [*Inan et al.*, 1993] that early/fast event occurrence or magnitude does not correlate well with NLDN peak current. Our findings indicate that the early/fast events are only produced by lightning episodes that include large sferic clusters.

The high degree of sferic cluster variability is well illustrated in Figure 3.7, showing several early/fast events (labeled A–H) and associated sferic clusters observed on 10 August 1998. These sferic spectra were recorded at YR, ∼300 km from the associated CG lightning activity.

Despite their variability in shape and duration, clusters all have an increased integrated intensity, and an algorithm has been designed to identify them. First, the sferic channel record is convolved with a test shape and normalized by its median value.   Then, the largest output of the convolution record is selected from every few seconds, and only values above a threshold are selected as clusters. The blue histograms in Figure 3.5 show this cluster intensity for a one-hour period around the 20-minute periods shown (a cluster intensity of 4 represents 4 times the median integrated intensity, weighted by the test shape). We then calculate an event "size" for all of the identified clusters defined as the ratio of several seconds of pre- and post-event amplitude; those clusters with events larger than a certain size are selected, and a histogram of that subset is superimposed in red. In Figure 3.5, the test shape was an 80-second unit step, with a 20-second interval, a threshold of 1.65, and an event threshold of 0.3 dB. Despite this very general algorithm used for both days in Figure 3.5, the results show that (i) there are relatively larger clusters seen on 15
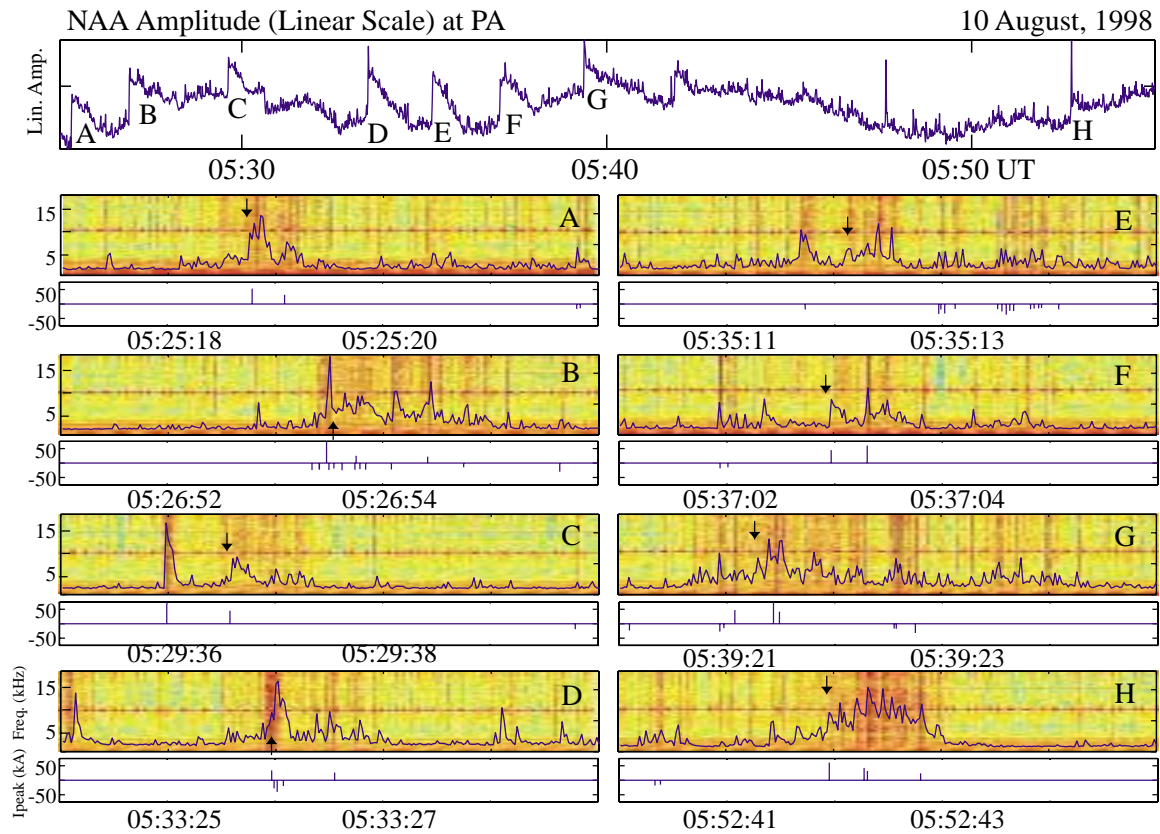
Figure 3.7: Sferic cluster variability. Eight early/fast events measured on the NAA–PA path, labeled A–H, are associated with sferic clusters showing a variety of shapes and durations. Some of the clusters are associated with NLDN recorded CGs while some are not. The time of the event onset is indicated with an arrow.

August than on 1 September and (ii) the large clusters are predominantly associated with early/fast events, and (iii) the early/fast events are predominantly associated with large clusters. Although not shown, this algorithm yielded similar results for the 10 August period.

3.4   IC Lightning as a Source of Sferic Clusters

A key property of the sferic clusters that lead to early/fast VLF events is the fact that they are apparent only in VLF waves which have propagated within a few hundred kilometers of the active thunderstorm. At large distances from the active thunderstorm, the associated large sferic is still unambiguously observed [*Inan et al.*, 1996a]

while the cluster is not. This property is illustrated in Figure 3.8, showing a sferic cluster associated with an early/fast event as observed at YR (200 km from the lightning) together with simultaneous broadband sferic spectra recorded at Stanford University (SU) (1800 km from the lightning). The associated time-domain waveforms are also shown on an expanded scale for a selected portion around the event onset. While the sferic cluster is clearly evident on the YR spectrogram, it is not visible at SU. In particular, the ~200 ms portion of the cluster is clearly evident in the YR time-domain waveform and detected intensity records from ~450 to ~650 ms. Noting that both the YR and SU time domain data are normalized so that the largest sferics have approximately the same amplitude, the intensity of the cluster of VLF energy (relative to the peak intensity of the largest sferics) is much larger at YR than at SU. It thus appears that the sferic cluster component of the VLF signal as observed at YR attenuated during its propagation between YR and SU significantly more than the discrete sferics.

This more rapid attenuation of the sferic cluster is consistent with an intracloud (quasi-horizontal) source, since the radiation pattern of a horizontal dipole above conducting ground exhibits a null at low elevation angles and thus preferentially launches waves that emanate from the antenna at relatively high angles [*Jordan and Balmain*, 1968; pp. 641–644], the raypaths of which are incident on the ionosphere at smaller angles of incidence (measured from vertical). Considering propagating modes in the earth-ionosphere waveguide as a superposition of uniform plane waves, wave energy launched at such high elevation angles preferentially excites higher-order waveguide modes [*Inan and Inan*, 1999; pp. 269–71], which in turn have higher attenuation rates [*Wait*, 1957]. Vertical discharges, in contrast, exhibit a maximum in their radiation pattern at low elevation angles, thereby preferentially exciting low-order waveguide modes with substantially lower attenuation rates.

In past work involving measurements at distances >500 km from the active thunderstorm, singular sferics were always observed in association with early/fast event onsets, even when no associated CG flashes were identified by NLDN. Such "causative"
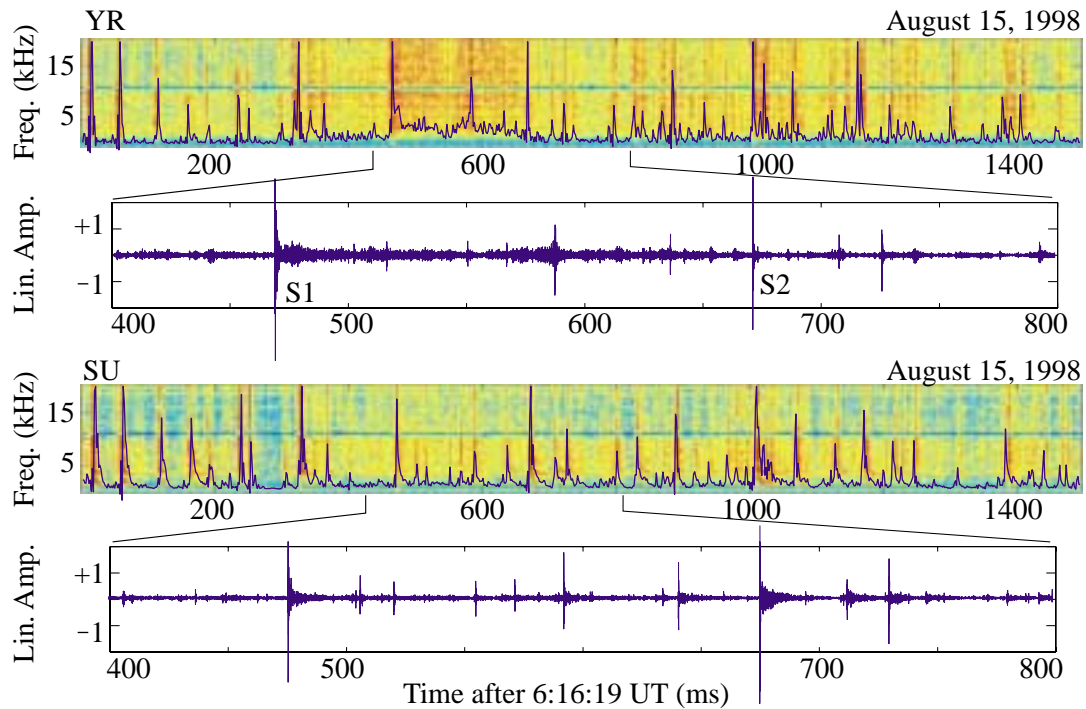
Figure 3.8: Sferic cluster attenuation. Spectrogram and normalized time domain data shown from YR, 200 km from the associated lightning discharge, with a cluster of sferic activity. Broadband data recorded at SU, some 1600 km farther from the lightning, demonstrates that the sferic cluster radiation has attenuated more rapidly than the individual atmospherics, consistent with quadrapole radiation from quasi-horizontal (intracloud) lighting.

sferics may have been due to large quasi-vertical intracloud flashes that partially excite higher order modes. As an example, the sferics labeled S1 and S2 in Figure 3.8 both appear to attenuate by a similar amount at SU compared with YR; yet, only S1 was recorded by NLDN (with peak current of +30 kA) as a CG. Peak current correlates well with sferic intensity, and both appear to be of the same magnitude. Based on the fact that NLDN claims to miss less than 10% percent of 30 kA flashes in the central U.S., S2 may have resulted from a quasi-vertical IC. On the other hand, these particularly complicated discharges may more often be discarded by the NLDN detection algorithm.

Although highly variable as indicated in Figure 3.7, the sferic clusters generally contain a few hundred milliseconds of increased intensity, followed by more impulsive bursts, consistent with other measurements of intracloud flashes. As an example, *Shao*

and *Krehbiel* [1996] shows a radar echo from an intracloud lightning flash demonstrating the continuous channel active portion of the flash lasting for ∼200 ms followed by the so-called K burst of intermittent flashes lasting for another ∼500 ms, with an overall shape remarkably similar to that of sferic bursts shown here. This similarity, the relatively high attenuation of the sferic cluster energy, the several hundred millisecond sustained radiation, and the lack of NLDN recorded CGs in every case all but excludes the cloud-to-ground channel as the sole radiator of the sferic clusters. This strongly suggests that the VLF energy of the clusters originates in intracloud lightning.

3.5 Early/Fast Event Occurrence

In this section, we present a fifteen-month survey of early/fast VLF event occurrence as observed on the NAA–HAIL paths, compare the occurrence from a two-month subset of the survey with lightning occurrence parameters in the vicinity of the NAA–HAIL great circle paths, and quantify the overall percentage of those lightning discharges that lead to detectable early/fast ionospheric disturbances.

In order to uniformly measure the VLF event occurrence rate for a period of many months, an algorithm was designed to automatically identify the characteristic event perturbation signature. Low resolution (1 s averaged) amplitude data were processed during the period from 03:00 to 10:00 UT (when events were most often observed). The data are first convolved with a step function, and the largest sample of the resulting sequence is selected from consecutive minute-long intervals. For each interval, an "event" magnitude is calculated as the ratio of the median of six pre-event samples to the median of three post-event samples. Events with a magnitude greater than 0.3 dB are then tested for a monotonic recovery to pre-event levels by calculating the median value of the data for three periods, and discarding those events in which the consecutive median values did not decrease. In this work the periods spanned the
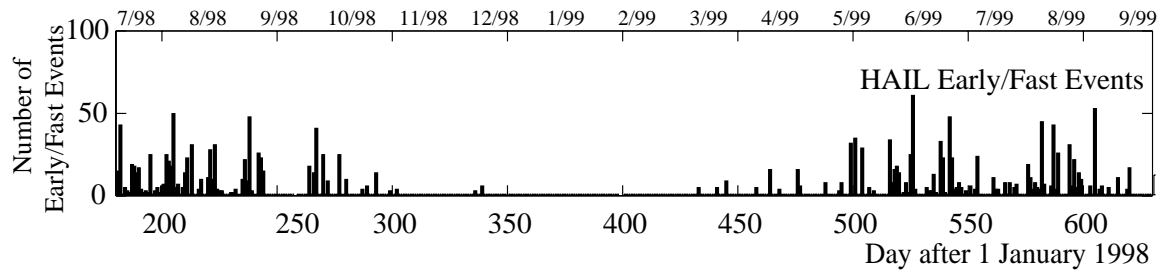
Figure 3.9: Early/fast event occurrence. Occurrence of early/fast VLF events as recorded from a single HAIL station, for the period 1 July to 1 September 1998.

following times[3] (in seconds), with t=0 being the event onset: 3–6 s; 9–11 s; 18–21 s.

From July 1998 through September 1999, processing the data in this manner resulted in thousands of candidate events. For each day, the events are visually inspected, and a count is made of those that appeared to be of the early/fast or LEP variety[4]. Because the onset delay differentiation is not observable with the low resolution data, the identification of event type is made with inspection of the multiple station amplitude data and/or the high resolution data. Multiple station amplitude data is used to identify event variety because early/fast events are typically observed at fewer than four of the nine HAIL receivers (see Figure 3.2) while LEP events are typically observed at more than four of the receivers (see Figure 4.2). For those cases in which the scattering pattern is projected along the edge of the HAIL array, a high resolution view of the event onset is used to provide unambiguous identification. As an additional simplification, the event count from each day is assumed to be entirely of one variety or the other. While there are instances where this is not the case (e.g., Figure 1.5 and *Inan et al.* [1993; 1996a]), high-resolution analysis of consecutive events typically indicates that they are entirely of one variety or the other.

In Figure 3.9, early/fast VLF event counts are shown to illustrate the seasonal variability of occurrence. Because selected receiver sites were occasionally non-operational

---

[3]These sample times were chosen to identify recoveries consistent with events visually identified as having well-defined recoveries.

[4]VLF event types not considered include short-duration events [*Inan et al.*, 1996a], and bipolar recoveries [*Burgess and Inan*, 1993].
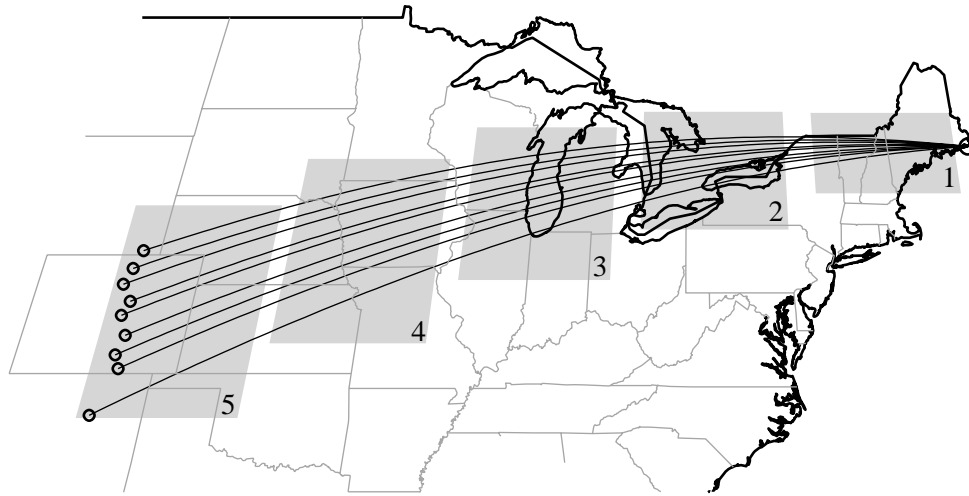
Figure 3.10: Geographic regions considered in the early/fast event statistics. Lightning occurring in each of the five grey regions was compared with early/fast event activity in Figure 3.11.

(particularly during the winter months), event counts were generated from consecutive periods in which only one receiver was monitored. This survey was then repeated twice, over separate path combinations, to more closely approximate the total number of events which would have been observed had data from all nine receivers been inspected. Early/fast event activity peaks during the boreal late-spring and summer periods, with few early/fast events observed during the winter months. On active days, more than 25 (in some cases, as many as 60) early/fast events greater than 0.3 dB were observed at a single site.

As noted in Section 3.1, *Inan et al.* [1996a] found that early/fast VLF events occur in cases for which the lightning discharge is within ± 50 km from the great circle path of propagation. In order to establish a correlation between the occurrence of lightning discharges and early/fast event activity, we thus limit the lightning occurrence region to be that within ± 50 km of the great circle paths in question. An approximation to this region for the NAA–HAIL paths is composed of five rectangular (in latitude and longitude) sub-regions, as shown in Figure 3.10.

For the period from 1 July to 1 September 1998, early/fast VLF events are counted on the NAA–TR and the NAA–FC signals, and the sum is plotted in Figure 3.11.

Because these two great circle paths are separated from each other by more than 100 km for the midwestern thunderstorm region, an early/fast event is not likely to be observed on both receivers simultaneously. The sum of the events measured along these two paths is thus used here as an approximation of the total number of early/fast events which would have been measured along the entire array. Also shown in Figure 3.11 is the total number of cloud-to-ground discharges measured by NLDN occurring over each of the five regions shown in Figure 3.10. The majority of lightning activity occurs in the midwestern[5] regions 4 and 5. For days with little lightning activity in these regions, few events are recorded, and for those days with a particularly large amount of lightning in those regions, the early/fast occurrence rate increases. The infrequent lightning activity in regions 1 and 2 is not well correlated with our observed early/fast event activity, perhaps due to the nature of the lightning in those regions or the rapid attenuation (with distance along the path) of the higher order modes of the signal scattered from an early/fast ionospheric disturbance. In any case, in an attempt to quantify the average fraction of observed lightning discharges which lead to early/fast events, we take the mean of the daily ratio of the number of early/fast events (on the NAA–TR and the NAA–FC signals) to the number of CG lightning discharges in regions 4 and 5. For this two month period, $\sim 0.43\%$ of all lightning discharges in these two regions produced early/fast events.

---

[5]As mentioned in Section 2.3, the establishment of the HAIL array in the midwest was in part motivated by this active midwestern summer lightning activity.
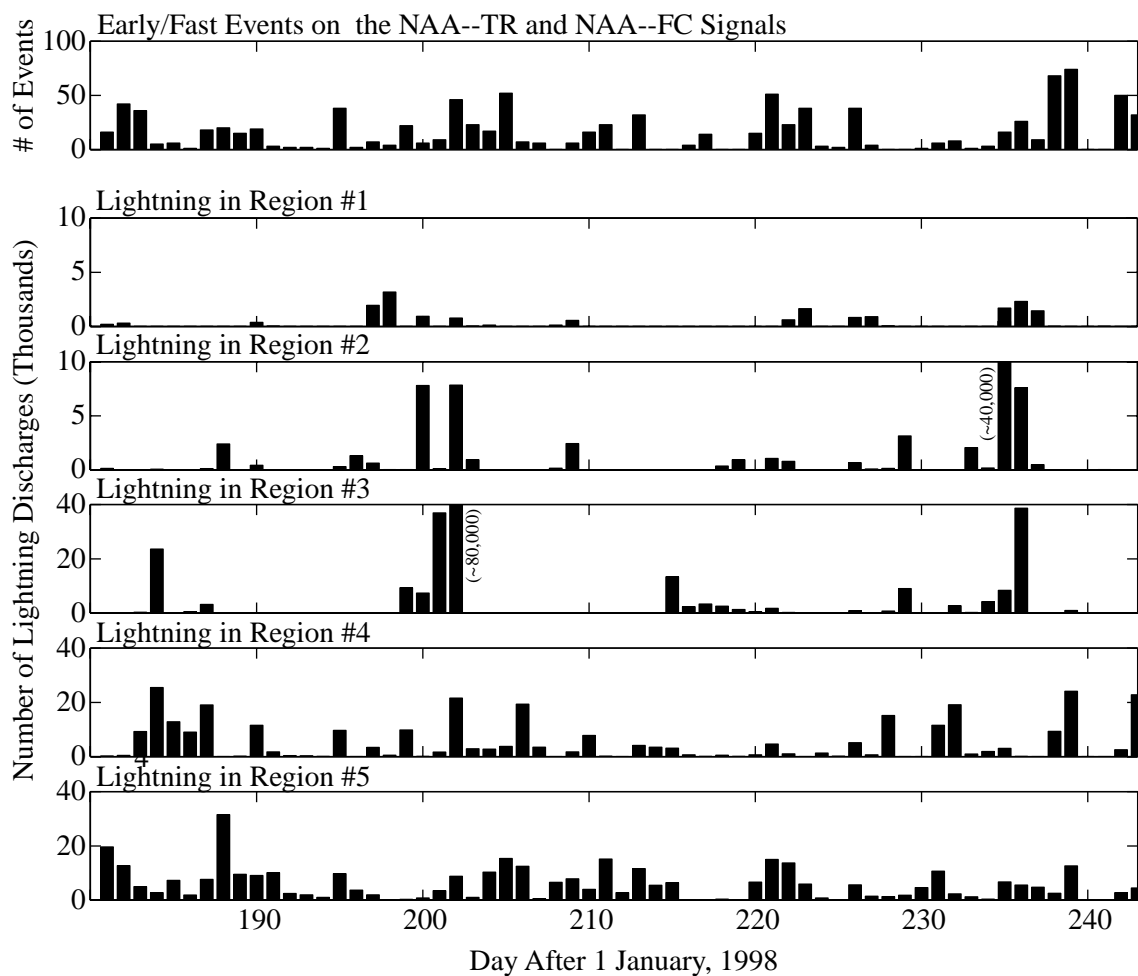
Figure 3.11: Early/fast event correlation with lightning activity. From 1 July to 1 September 1998, the early/fast event count is shown from the NAA–TR and NAA–FC signals (an approximation to the total number of early/fast events which would have been measured along the entire array). The total number of cloud-to-ground discharges which occurred during recording times is plotted below for each of the five regions shown from Figure 3.10. About 0.43% of all lightning activity during this period was associated with an early/fast VLF event.

Chapter 4

Lightning-Induced Electron Precipitation Events

In addition to directly disturbing the lower ionosphere, lightning discharges can indirectly cause ionospheric disturbances through a process of lightning-induced precipitation of energetic electrons (LEP), as mentioned in Section 1.3.2. Ionospheric disturbances produced by LEP events are detected via their associated characteristic perturbations in the amplitude and/or phase of a subionospheric VLF signal. Such perturbations, known as LEP VLF events, differ from early/fast VLF events in that they exhibit a characteristic onset delay and duration associated with the event onset [*Inan et al.*, 1996a] and recover to the pre-event signal level with a less rapid initial rate [*Sampath et al.*, 2000]. In Section 4.1, we illustrate the typical characteristics of an LEP VLF event.

The physical mechanism for LEP VLF events involves a process of magnetospheric wave-particle interaction. A fraction of the energy radiated by a lightning discharge escapes into the magnetosphere and propagates as a whistler-mode wave where, through a process known as gyroresonance, it interacts with and changes the pitch angle of trapped radiation belt electrons, causing those close to the loss cone to precipitate into the lower ionosphere. These precipitated high energy electrons cause secondary ionization, modifying the ambient conductivity which in turn is manifested as a VLF perturbation in subionospheric VLF waves. In Section 4.2, we differentiate

and provide an overview of both "ducted" and "nonducted" whistler waves, which respectively propagate along and at a varying angle (i.e., obliquely) to the geomagnetic field lines, and also introduce the process of gyroresonance. In Section 4.3.1, we discuss the various physical parameters that determine the electron precipitation fluxes produced by obliquely propagating (nonducted) whistlers. In Sections 4.3.2 and 4.3.3, we present the first recognized experimental evidence of LEP produced by nonducted whistler waves launched by lightning discharges (work originally published as a journal article [*Johnson et al.*, 1999b]). We then quantitatively interpret a set of precipitation signatures observed with the HAIL array and assess the magnitude of the precipitation fluxes in Section 4.4. We conclude in Section 4.5 by reporting on the long term occurrence statistics of LEP VLF events and comment on their association with lightning and geomagnetic activity.

4.1   LEP VLF Event Signatures

The modification of the D region conductivity by the LEP process and the detection of this effect as subionospheric VLF signal changes are schematically described in Figure 4.1. A small fraction of the electromagnetic wave energy radiated by lightning discharges couples through the lower ionosphere and propagates into the magnetosphere as a whistler mode wave, where it can interact with trapped radiation belt electrons, scattering them in pitch angle and causing them to precipitate into the atmosphere, leading to significant disturbances of the D region conductivity and perturbing the amplitude and/or phase of the subionospheric VLF signals. Two significant differences distinguish such disturbances from those produced by direct coupling (i.e., as measured by early/fast VLF events) discussed in Chapter 3; (i) the causative lightning discharges are not necessarily located directly below the disturbed region and are instead typically at lower latitudes and (ii) the size of the scattering region is typically much larger than $\sim$100 km across (Figure 4.1b) as evidenced by the fact that often many HAIL paths are simultaneously disturbed. The resulting VLF signal
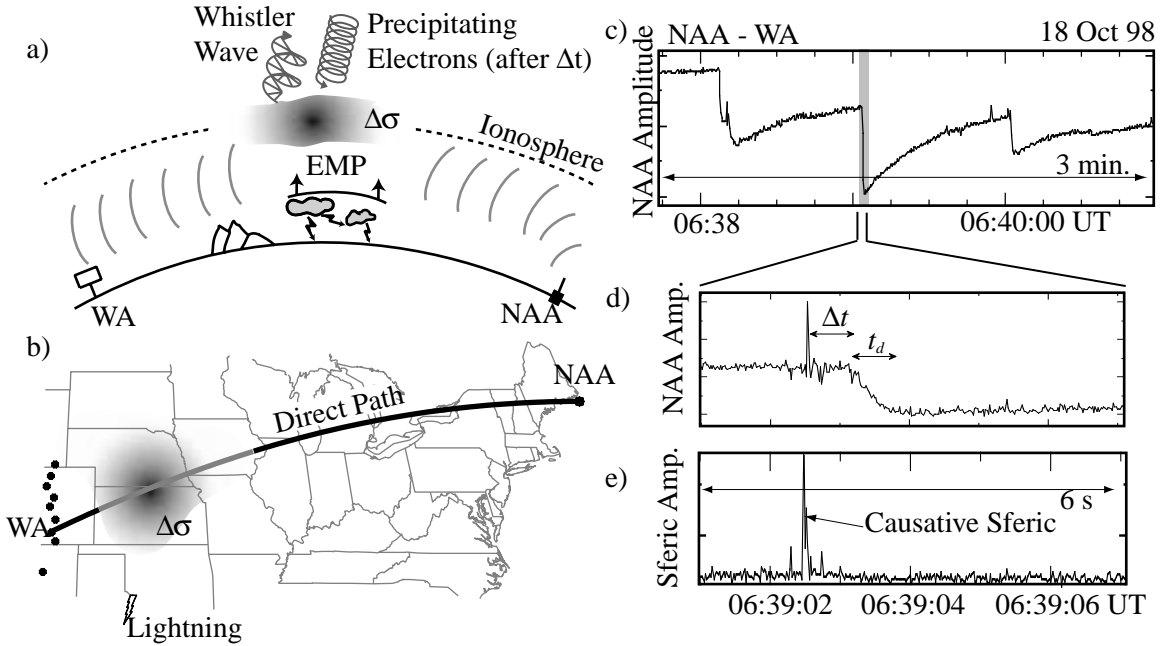
Figure 4.1: LEP event overview. (a) Lightning-induced electron precipitation causes secondary ionization along a great circle path of propagation. (b) The D region ionospheric disturbance perturbs VLF signals propagating underneath. (c–e) An example LEP event with characteristic onset delay (Δt) and duration t_d with respect to the causative sferic.

perturbations are characterized (Figure 4.1c and 4.1d) by (i) a characteristic onset delay Δt (a few hundred ms up to $\sim$1 s) with respect to the causative sferic (Figure 4.1e) due to the magnetospheric travel time of the outgoing whistler wave and the pitch angle scattered energetic particles: (ii) an onset duration, t_d (typically $\sim$0.5–1.5 s) representing the duration of the precipitation burst, during which the VLF event magnitude increases due to continuing generation of secondary ionization: and (iii) a recovery period of 10–100 s following the termination of the precipitation burst, as the ionization returns from enhanced levels back to pre-event levels [*Pasko and Inan*, 1994].

For LEP type VLF events, the onset delay Δt and the duration t_d depend on the L shell of the geomagnetic field line(s) near which the whistler waves propagate, as well as the ambient magnetospheric cold plasma density [*Inan and Carpenter*, 1986]. For LEP events induced by ducted whistlers, as described in the following section, these

parameters are quantized for any given case (see Figure 4.3). In contrast, scattering by obliquely propagating whistlers (that permeate a wide range of field lines) leads to precipitation over an extended region, with a continuum of onset delays and durations as a function of latitude [*Lauben et al.*, 1999]. Example LEP event sequences from three days, shown in Figure 4.2, reveal that individual events are visible at a majority of the HAIL receivers, consistent with a relatively large disturbance region overlying most NAA–HAIL paths. The particularly high signal-to-noise ratio case from 18 October 1998 is discussed in detail in Sections 4.3 and 4.4

4.2   Ducted and Nonducted Whistlers

The magnetized cold plasma environment of the magnetosphere supports a rich variety of propagating electromagnetic modes. In the VLF range and between the local proton gyrofrequency (typically <500 Hz) and electron gyrofrequency (typically >14 kHz in the plasmasphere), magnetospheric waves propagate as highly dispersive right-hand elliptical polarized modes [*Baumjohann and Treumann*, 1997; p. 230]. In 1925, T. L. Eckersley published an observation of electromagnetic signals in the audio frequency range with descending pitch (over ∼1 s duration), which he attributed to impulsive signals dispersed from a medium loaded with free ions. By the early 1950s, these "whistlers" were identified by L. R. O. Storey as originating from lightning-generated impulses and being dispersed by propagation through unexpectedly high plasma densities at distances of several Earth radii. Through such observations, whistler wave characteristics were used to map the electron density of the inner magnetosphere [see *Helliwell*, 1965; pp 180–202].

In order to be detected on the ground after propagation in the magnetosphere, whistlers must arrive at the top of the ionosphere with an angle of incidence within several degrees of normal, so that they do not undergo total internal reflection [*Helliwell*, 1965; pp. 51–61]. Field aligned structures with enhanced electron densities several tens of a percent above the background levels were hypothesized to guide the
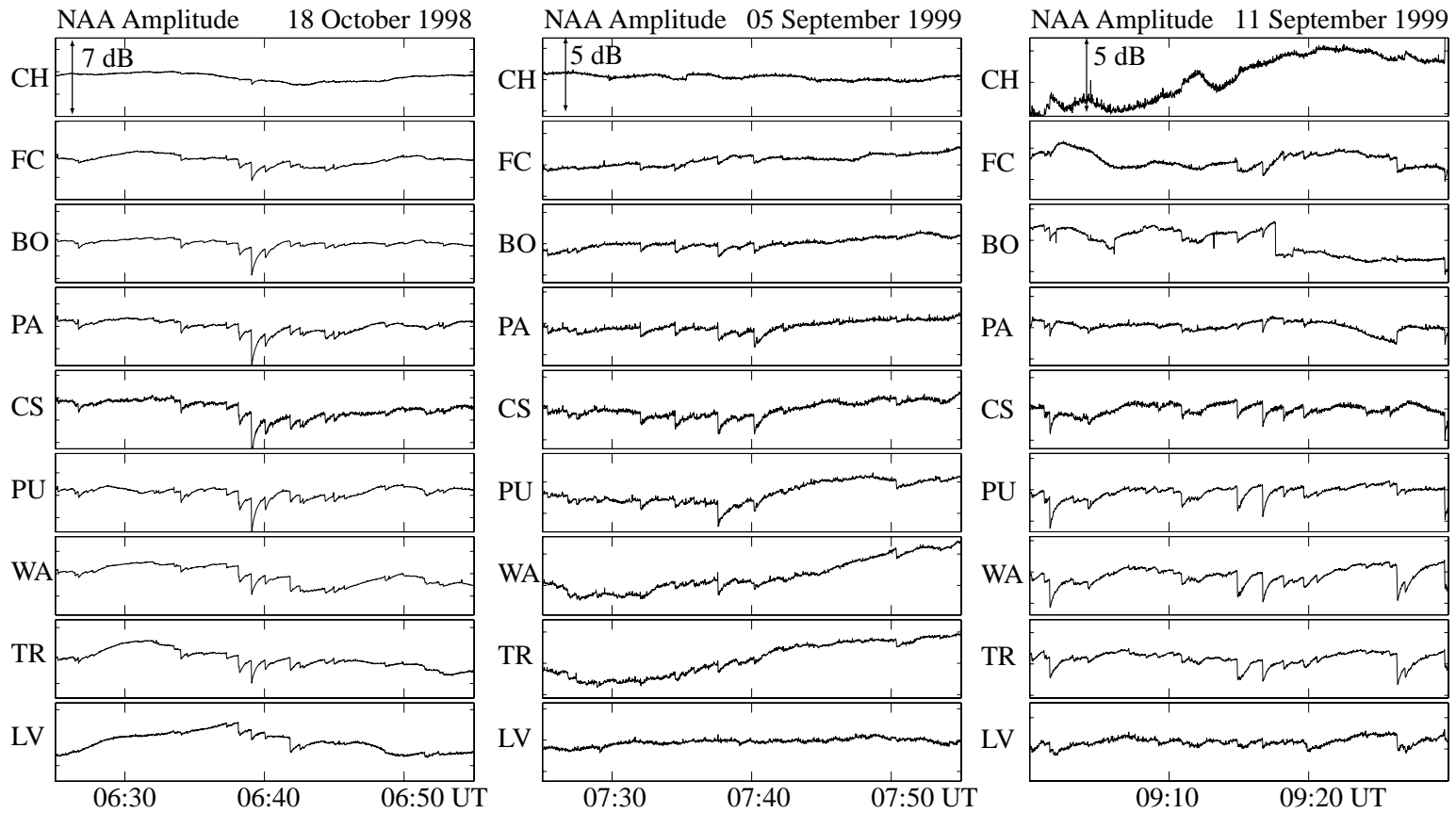
Figure 4.2: LEP event examples. LEP event examples from three days in 1998. While the shape and size of the events are variable, they typically are observed on a majority of the HAIL receivers. In each case, expansion of the event onsets clearly shows the onset delay and duration characteristic of LEP events. (Note: the NAA–BO amplitude for the 11 September 1999 case was somewhat corrupted by an anomalous level shift.)
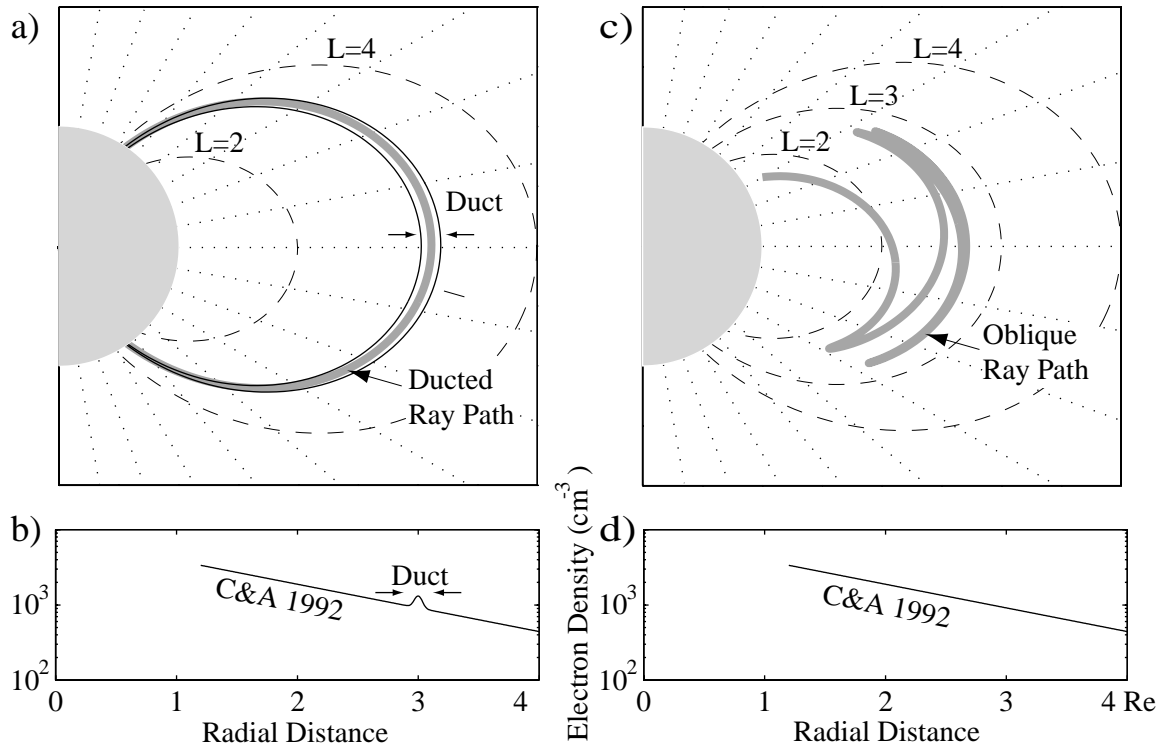
Figure 4.3: Ducted vs. oblique whistler wave propagation paths. (a) Example ray path of a whistler wave propagating along a duct of enhanced conductivity. (b) Example equatorial cold electron density profile with a hypothetical density enhancement at L=3. (c) Example ray path of an obliquely propagating (nonducted) whistler wave. (d) Exponential density profile from *Carpenter and Anderson* [1992].

whistler wave propagation along magnetic field lines (in a manner analogous to light propagating in a refractive index graded optical fiber), as illustrated in Figure 4.3a. These structures, known as magnetospheric "ducts", have been estimated to have lateral extents of ≤500 km at the equator [see *Burgess and Inan*, 1993, and references therein]. Despite many attempts to observe ducts by *in situ* satellite observations, their relatively small size make them unlikely to be observed, and only one *in situ* observation has been made to date [*Angerami*, 1970].

In the absence of ducts of enhanced plasma density, whistler waves propagate "obliquely" in the magnetosphere along raypaths determined by gradients of the magnetospheric cold plasma and the Earth's magnetic field. Oblique propagation, illustrated in Figure 4.3b, is in general not along a magnetic field line, and occurs with

wave-normal vectors having angles (with respect to the local static magnetic field) of up to the so-called resonance cone angle, which can be close to 90°, and also at large angles with respect to the ray direction vector (i.e., the direction of energy travel). Although the high wave-normal angles prevent the whistler energy from penetrating through the sharp lower ionospheric boundary to ground level, these obliquely prop-agating so-called *nonducted* whistlers are commonly observed on satellites [*Edgar*, 1976; *Gurnett and Inan*, 1988].

As whistler waves propagate through the magnetosphere, they encounter energetic radiation belt electrons gyrating in trapped orbits along the magnetic field lines. The number density of these energetic electrons is relatively low (<1 el/cc) so that their effect on the propagation characteristics of the waves can be typically neglected [*Inan et al.*, 1978]. However, when the Doppler-shifted wave frequency of a whistler wave is matched to the gyrofrequency of a counterstreaming trapped energetic electron, the wave fields can cumulatively affect the particle, causing its momentum to change [*Inan et al.*, 1978]. This "gyroresonance" condition can be expressed by $\omega_h/\gamma \simeq \omega + k_\parallel v_\parallel$ where ω is the whistler wave frequency, $\omega_h/\gamma = qB/m\gamma$ is the relativistic gyrofrequency of the trapped electron with $\gamma = (1 - v^2/c^2)^{-1/2}$ being the relativistic factor, and $k_\parallel$ and $v_\parallel$ are respectively the wave number and the component of the particle velocity in the direction of the magnetic field line.

The ratio of the electron velocity perpendicular to the magnetic field to its parallel velocity in its gyrating orbit determines an instantaneous *pitch angle*, where $\alpha = \tan^{-1}[v_\perp/v_\parallel]$ with respect to the magnetic field line. This pitch angle varies as the particle traverses its path between the two hemispheres, increasing with distance away from the geomagnetic equator. As the electron travels poleward, α increases and $v_\parallel$ decreases until the pitch angle becomes 90°, and the electron "mirrors" back moving in the opposite direction [*Walt*, 1994; pp. 10–23].

Electrons with an equatorial pitch angle below the so-called "loss cone" angle, α_{lc}, descend below an altitude (typically taken to be ∼1000 km [e.g., *Chang and Inan*, 1985]) where a collision with an atmospheric molecule is highly probable. The
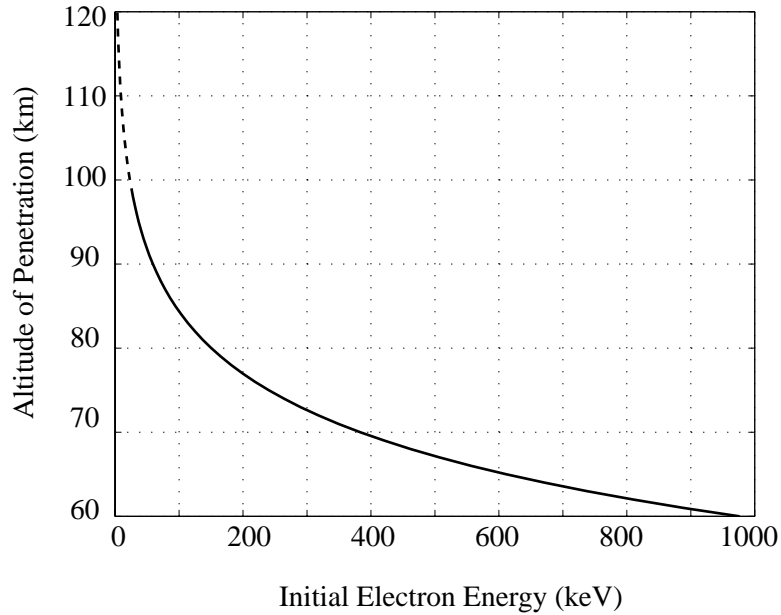
Figure 4.4: Depth of penetration of precipitating electrons. The most probable depth of penetration of electrons from 1 keV to 1 MeV [*Banks et al.*, 1974].

equatorial pitch angle is specified by $\alpha < \alpha_{\mathrm{lc}} = \sin^{-1}\sqrt{B_{eq}/B_a}$, where B_a is the magnitude of the magnetic field at the mirror altitude and B_{eq} is the magnitude of the magnetic field at the equatorial plane.

When an energetic electron descends into the atmosphere, it loses momentum by undergoing repeated collisions with neutrals, producing localized heating, secondary ionization, light, and x-rays. An overview of models that describe the ionospheric response to energetic electrons penetrating into the atmosphere is given in *Doolittle* [1982; pp. 96–100]. *Banks et al.* [1974] calculated the ionization rate per unit incident flux as a function of altitude, assuming that an incident beam of electrons is isotropic in pitch angle and that the energy distribution of the flux is defined by a narrow Gaussian distribution. Based on such a calculation, the altitude of maximum ionization rate can be found, and is plotted in Figure 4.4 for incident energies less than 1 MeV. We see that the lower D region altitude range is primarily affected by secondary ionization by electrons in the $\sim$100–200 keV energy range.
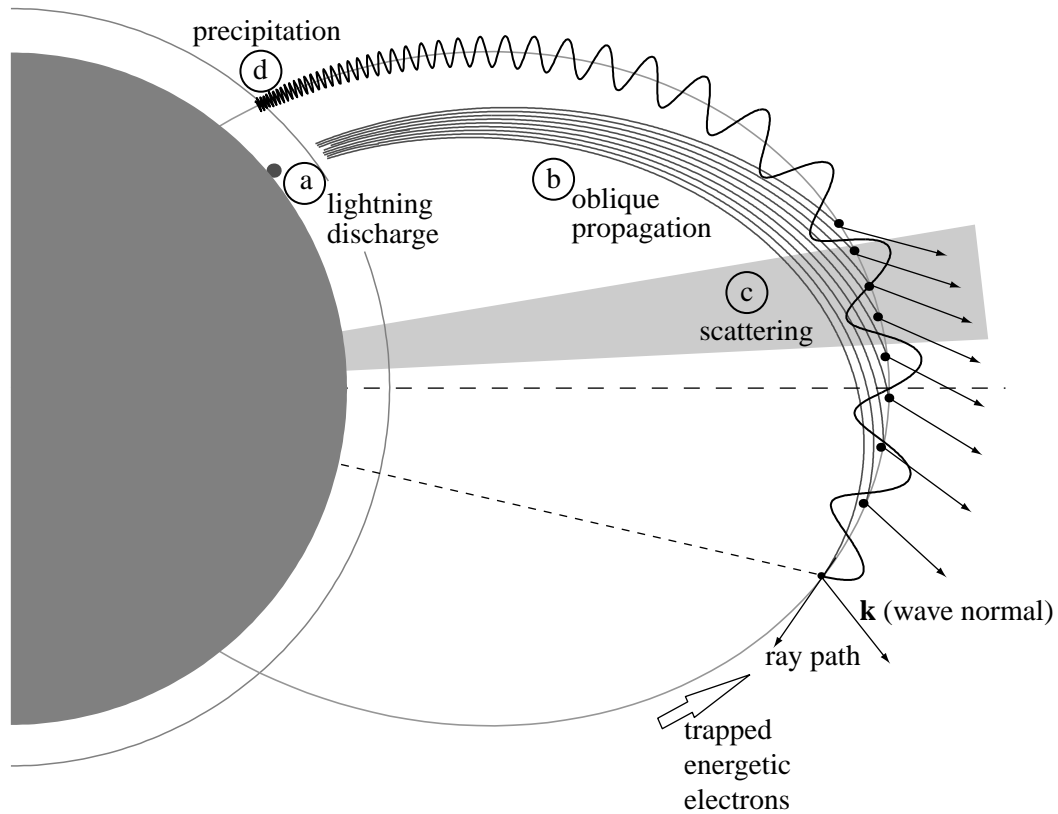
Figure 4.5: Oblique wave-particle interactions. (a) A lightning discharge occurs, injecting whistler mode waves into the magnetosphere. (b) In general, the wave energy propagates obliquely with respect to the Earth's magnetic field. (c) Near the equatorial region, the oblique whistler can resonate with trapped electrons, scattering them in pitch angle. (d) Those electrons which are scattered into the loss cone precipitate into the atmosphere causing secondary ionization. Adapted from *Lauben et al.* [1999].

4.3 Nonducted Whistler-Induced Precipitation

In this section, we review the recent *Lauben et al.* [1999] model of oblique (non-ducted) whistler-induced precipitation (illustrated in Figure 4.5), and discuss the various physical parameters that affect the magnitude of the resulting precipitated flux. In Section 4.3.2, we introduce a case study from 18 October 1998, and interpret the spatial size of the ionospheric disturbance in light of the size of the observed VLF event signatures. We then discuss the observed event onset delays in Section 4.3.3 and compare them with those expected from the *Lauben et al.* [1999] model.

4.3.1 Oblique Precipitation Model

The characteristics of precipitated fluxes induced by typical lightning-generated oblique whistler waves were quantified by *Lauben et al.* [1999]. The magnitude, spatial distribution, and energy spectra of induced precipitation fluxes produced by any given lightning discharge are determined by the illumination of the magnetosphere by whistler waves and magnetospheric conditions such as the cold plasma density distribution and the velocity space distribution of the trapped energetic electrons. In Section 4.4, we use VLF Earth-ionosphere waveguide propagation and scattering models to quantitatively interpret the observed VLF signatures and to ultimately compare them with the properties of the LEP bursts as predicted by *Lauben et al.* [1999]. In this context, it is important to recognize that the "typical" parameter values used in the *Lauben et al.* [1999] model contain inherent variability as described below.

The first step in quantifying the precipitation induced by obliquely propagating whistler waves is the calculation of the whistler wave field intensity injected into the magnetosphere by a given cloud-to-ground lightning discharge. The electromagnetic wave radiated by a lightning discharge is measured as a radio atmospheric at a point distant from the source and contains inherent spectral variability in both shape and magnitude. A three parameter model for the discharge current profile, initially proposed by *Bruce and Golde* [1941], is of the form $I(t) = I_0(\exp^{-bt} - \exp^{-at})$, where I_0, a, and b are constants. *Dennis and Pierce* [1964] found that the average spectrum, $S(\omega)$, for a group of sferics obeys a relation in which the frequency of maximum amplitude lies within the range of 4 to 7 kHz (for negative discharges) and that the amplitudes are log-normally distributed with a standard deviation of $\sim$7 dB. In that work, variability was found in the typical parameters between positive and negative discharges, with the positives having a spectral peak near $\sim$3 kHz and the negatives peaking at $\sim$5 kHz, and the authors noted that the spectrum of an individual stroke is influenced by such characteristics as nonvertical sections of the channel, branching, and irregularities of the current surge. Following *Cummer and Inan* [1997], *Lauben et al.* [1999] selected discharge parameters of $a = 5 \times 10^3$, $b = 1 \times 10^5$, and

$I_0 = -10.53$ kA, corresponding to a peak radiated electric field intensity 100 km from the discharge of $E_{100} = 10$ V/m. From *Orville et al.* [1991], the corresponding peak current for a cloud-to-ground discharge is found to be 33 kA using the relationship $I_{peak} = 2\pi D\varepsilon_0 c^2 E_{100}/v$, where c is the speed of light in free space, ε_0 is the dielectric permittivity of free space, $D = 10^5$ m is the distance from the discharge, and $v = 1.5 \times 10^8$ m/s is the return stroke velocity.

The radiated wave power expands spherically at first, and eventually spreads out in a more cylindrical pattern due to the guidance of the Earth-ionosphere waveguide boundaries. Following *Crary* [1961] and *Inan et al.* [1984], the spreading is assumed to exhibit r^{-2} dependence for the first 1500 km, followed by attenuation of 2 dB/1000 km thereafter. A fraction of the wave energy couples upward through the lower ionosphere and propagates through this lossy medium with a frequency and latitude dependent attenuation as given by *Helliwell* [1965; p. 71]. The attenuation through the lower ionosphere is largely determined by the collision frequency profile, which in turn is related to the neutral atmospheric density, and thus does not change appreciably with time. The resulting wave power spectral density at ~1000 km, further decreased by 3 dB due to polarization loss, constitutes the input to a ray tracing model that in turn determines wave fields throughout the collisionless magnetospheric medium.

In situ satellite measurements by the Plasma Wave Instrument on the POLAR spacecraft have shown typical oblique wave field intensities of ~20 pT as measured near the magnetic equator (after propagation and attenuation with the above assumptions) [*Lauben et al.*, 1999]. This field intensity also corresponds to the causative discharge peak radiated field of $E_{100} = 10$ V/m assumed by *Cummer and Inan* [1997]. However, it is unlikely that the POLAR measurements were made in the region of maximum whistler field intensity, allowing the possibility of larger oblique whistler intensities. Additionally, from satellite measurements of pitch angle deflections of several degrees, *Inan et al.* [1989] estimated that whistlers associated with LEP events may have an equatorial magnetic field as large as 200 pT. Thus, whistlers leading to observed LEP events may have equatorial intensities greater than those conservatively
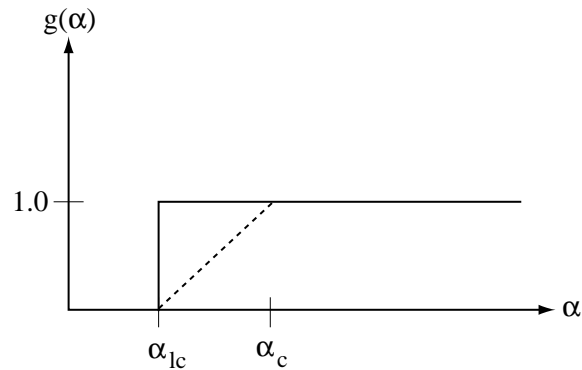
Figure 4.6: Loss cone distribution. An abrupt pitch angle distribution, $g(\alpha)$, of trapped electrons in the magnetosphere was assumed for the model used in this work, but *in situ* measurements suggest that the pitch angle distribution more likely exhibits a gradual edge [e.g. *Inan et al.*, 1989]. Figure adapted from *Inan et al.* [1982].

assumed by *Lauben et al.* [1999] and used in Section 4.4.

In addition to the whistler wave magnetic field intensity, several magnetospheric parameters directly affect the magnitude, spatial distribution, and energy spectrum of the precipitated flux. As mentioned in Section 4.2, trapped electrons with equatorial pitch angles less than the loss cone angle encounter the dense region of the atmosphere during their bounce motion and are likely to precipitate. In the simplest case, the pitch angle distribution of the trapped electrons, $g(\alpha)$, may be nearly zero for particles with an equatorial pitch angle less than the loss cone angle and nearly constant for particles with a pitch angle above the loss cone. *Lauben et al.* [1999] assumed such an abrupt edge of the loss cone as shown in Figure 4.6, and calculated precipitation fluxes for a whistler with peak intensity of $\sim$20 pT. However, based on spacecraft measurements [*Inan et al.*, 1989], the distribution function at the edge of the loss cone may not be abrupt (see dashed line in Figure 4.6) with the resulting precipitation flux being proportionally lower [*Inan et al.*, 1982].

The gradients of the magnetospheric cold plasma and the Earth's magnetic field determine the distribution of the whistler raypaths, and thus affect the size, shape, and latitudinal extent of the precipitation regions. The radial profile of cold plasma density used by *Lauben et al.* [1999] was based upon a quiet nighttime profile given

Lightning Power Spectrum	$S(\omega)$	*Cummer and Inan*, 1997
Pitch Angle Distribution	$g(\alpha)$	*Inan et al.*, 1989
Differential Energy Spectrum	Φ_E	*Inan et al.*, 1982
Velocity Dependence	v^n	*Inan et al.*, 1978

Table 4.1: Parameters which affect LEP flux

in *Carpenter and Anderson* [1992], and the magnetic field model used was a centered, tilted dipole model.

The magnitude and energy spectra of the precipitated flux is further determined by the trapped energetic particle distribution. The energetic particle distribution function $f(v, \alpha)$ can be written as [*Inan et al.*, 1982]:

$$f(v, \alpha) = \frac{m^2}{2E} \left[\frac{2E}{m} \right]^{n/2} \Phi_E v^{-n} g(\alpha) \qquad (4.1)$$

where Φ_E is the differential energy spectrum of electrons with energy E (keV) and rest mass m, and is taken to be 10^8 el/cm^2/s/sr/keV at $E =$ 1 keV [*Inan et al.*, 1978 and references therein]. The exponent in the v^{-n} velocity dependence can be adjusted to match particular *in situ* observations; a value of $n = 6$ was used by *Lauben et al.* [1999], once again based upon past work [*Inan et al.*, 1978 and references therein].

A summary of the various parameters used in the oblique LEP model which affect the magnitude of the precipitated flux, along with associated references, is provided in Table 4.1.

4.3.2 Nonducted LEP Events and Associated Disturbance Size

On eleven days in October 1998, data from the expanded HAIL array of nine receivers clearly show LEP VLF event activity on the NAA transmitter signal. Of these eleven, repeated (>10 in one hour) and clearly identifiable (>0.5 dB) LEP VLF events occur on six days.

In particular, several tens of events observed with the HAIL array on October 18

were large (several dB), and were individually imaged with the array on three sets of VLF paths, suggesting a massive ionospheric disturbance region. The left-hand panel of Figure 4.7 shows a five minute sequence of VLF amplitude events, marked A–D, from several disturbances on the NAA signal. Although the event magnitudes vary along the array for each event, relative values of the amplitude changes at different sites along the array were similar for the series of different events, indicating that the causative ionospheric disturbances were similar in location and size.

Event "B" from Figure 4.7 (at ∼6:39:03 UT), is expanded for the WA receiver in Figure 4.1, and shows the characteristic recovery to the ambient level (Figure 4.1c) and the characteristic onset delay and duration with respect to the causative sferic (Figures 4.1d and 4.1e). Data from NLDN identified only two discharges in the U.S. during the second containing the causative sferic, both located near Austin, Texas, occurring at 6:39:02.487 and 6:39:02.532 UT, with peak currents of ∼15 kA. Other events in the sequence are also associated exclusively with observed discharges in central Texas.

High-resolution amplitude data from all four VLF transmitters recorded at the nine HAIL receivers are plotted in Figure 4.7 for a four-second period around the event B onset. While ionospheric disturbances with ∼100 km spatial extents (e.g., those involved in early/fast VLF events) are typically observed at only two or three of the HAIL receivers (Chapter 3), in this case all of the NAA–HAIL paths and the upper five NAU–HAIL were perturbed, indicating a disturbance of much larger extent located to the east of the array. The absence of events on the lower four NAU–HAIL paths (despite being closer to the causative discharge), indicates a poleward-displaced precipitation zone, as predicted by *Lauben et al.* [1999]. While the NPM–HAIL paths are not perturbed, the northernmost two NLK–HAIL paths were affected, suggesting that the disturbance had a wider extent in longitude at higher latitudes.

With the assumption that the precipitation was centered about the line of constant magnetic longitude passing through the causative lightning location, the perturbations ranging from the NAU–PA path to the NAA–CH path indicated that the

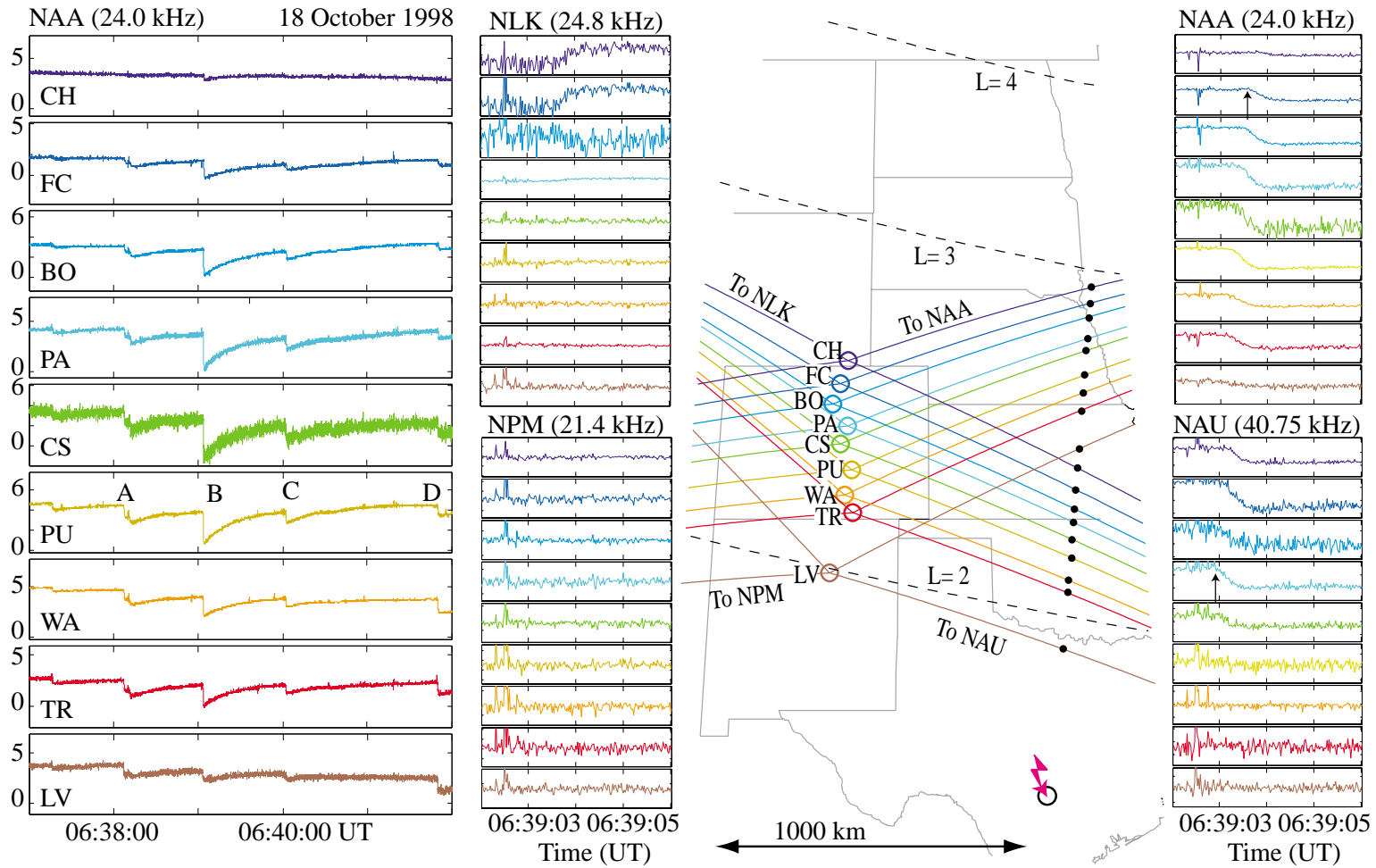**Figure 4.7: 18 October 1998 LEP event.** A five minute record of the received amplitude from NAA at the nine HAIL sites is shown on the left, with four VLF events labeled A–D. The amplitude for event B is expanded into 4 dB windows for each of the transmitter signals. Intersection points of the great circle paths and the magnetic longitude of the causative discharge (∼6:39:02.5 UT, near Austin, Texas) are shown as black dots.

disturbance has a latitudinal extent of more than 800 km. The perturbation of the
NLK–CH and NLK–FC signals suggest that the disturbance extended ∼900 km in
magnetic longitude. With the assumption of symmetry about the line of constant
magnetic longitude, the overall region of detectable electron density enhancement is
therefore on the order of 800 × 1800 km², or ∼1.5 million km². Based on model
predictions [*Lauben et al.*, 1999], the region may in fact have extended farther to the
North beyond the region covered by the HAIL VLF paths.

4.3.3   Differential Onset Delay

A striking feature of the data is the steadily increasing onset delay with increasing
geomagnetic latitude of the affected paths. The lowest path to be significantly af-
fected, NAU–PA, has an onset time for event B marked with an arrow in Figure 4.7.
In comparison, the corresponding onset occurs over ∼0.5 s later on the NAA–FC
path. To better illustrate the different onset times, filtered and normalized amplitude
signatures from NAA for events A–D are superimposed in Figure 4.8. In each of the
cases, the onset delay increased with receiver latitude. For the best defined case,
event B, we have a remarkably well defined set of curves with onset delay increasing
monotonically with latitude.

The distinctly different onset delays evident in Figure 4.8 indicate that the various
VLF paths respond to ionospheric disturbance regions that are activated at different
times, suggesting that the VLF amplitude changes on the different paths *cannot* be
due to subionospheric VLF scattering from a single localized ionospheric disturbance
produced near the footprint of a whistler-mode duct. Instead, the continuum of onset
delays steadily increasing with geomagnetic latitude agrees remarkably well with the
predictions of *Lauben et al.* [1999].

The resulting precipitation region for a source lightning discharge at the location
of the causative discharge for event B is shown in Figure 4.9a for electron energies
greater than 100 keV. For this case of a simple tilted dipole model and neglecting any
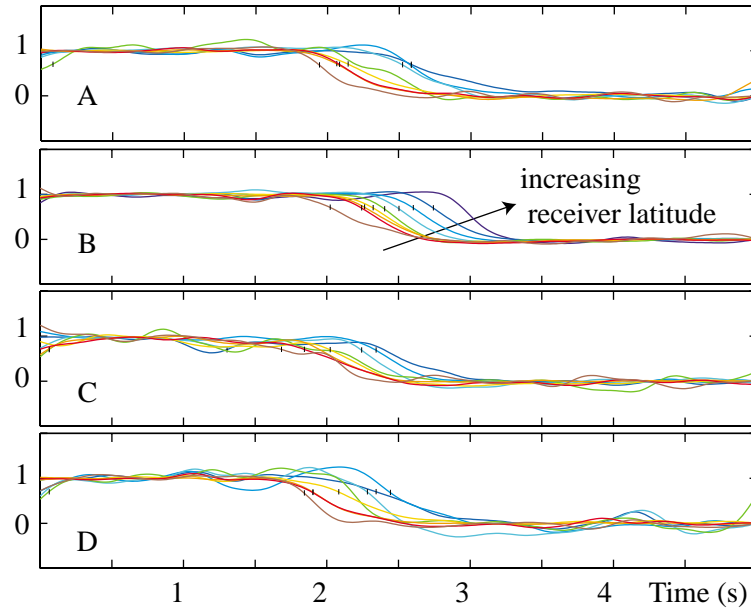
Figure 4.8: 18 October 1998 differential onset delay. Normalized and filtered high resolution (20 ms) data (linear scale) for the nine NAA–HAIL signals superimposed for the events A–D from Figure 4.7, illustrating the increase in onset delay with increasing path latitude.

longitudinal gradients in the Earth's magnetic field or cold plasma density, the precipitation region is symmetric in geomagnetic longitude. The energy-flux deposition as a function of time and latitude is shown in Figure 4.9b and describes the manner in which the different paths of the precipitation region appear in time. Also shown in circles are the onset delays and durations measured on the different HAIL paths, with the geomagnetic latitude for each path determined as the point of intersections of the constant longitude line with the great circle path of interest.

The measured onset delays and durations in Figure 4.9b have the same general latitudinal variation as those predicted, although the predicted flux appears earlier in time and higher in latitude. The higher-than-predicted onset delays indicate that the magnetospheric cold plasma density values were higher than those used in *Lauben et al.* [1999], resulting in longer travel times for both the waves (whistler-mode refractive index is proportional to the square root of cold plasma density) and particles (gyroresonant electron energies are lower for higher values of refractive index). The fact that the predicted precipitation region is located at higher latitudes implies
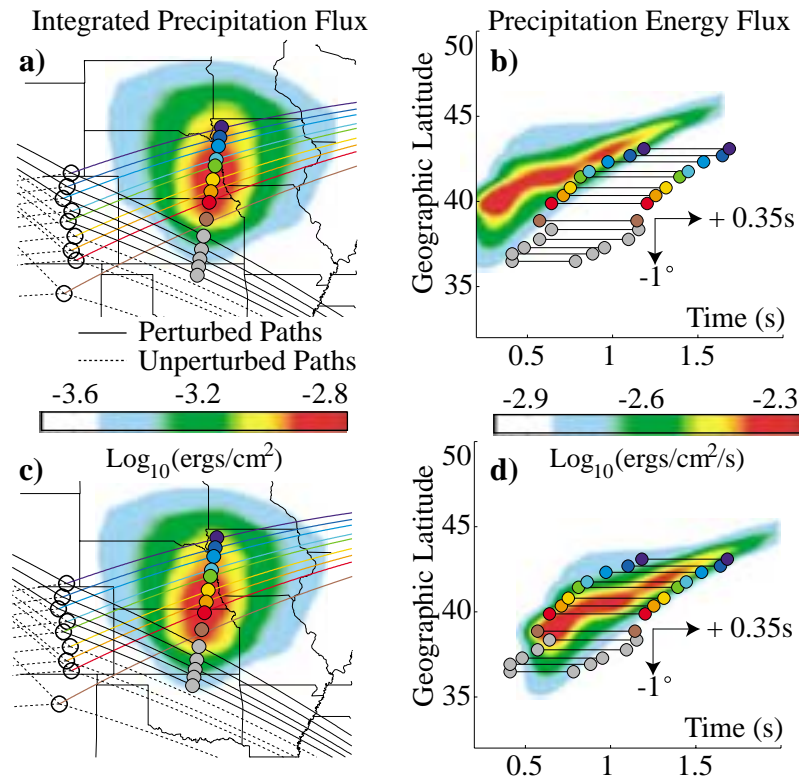
Figure 4.9: Energy flux signature. (a) *Lauben et al.* [1999] model predictions of time-integrated precipitation flux for E> 100 keV due to a 33 kA peak current discharge at the location of the causative discharge for event "B". (b) Corresponding flux plotted vs. geographic latitude and time, LEP event onset times and durations for event "B" superimposed. (c) and (d): Same as above, but shifted southward by 1° and increased in time by 0.35 s.

that the actual oblique whistler-mode raypaths were confined to somewhat lower L shells, and thus that the radial (i.e., L shell) variation of the magnetospheric cold plasma density was more rapid than that used in *Lauben et al.* [1999]. The raypath configuration is determined primarily by the gradients of the static magnetic field, which does not exhibit significant day-to-day variations within the plasmasphere, and cold plasma density, which varies day-to-day depending on the geomagnetic activity, plasmapause location and local time [Section 4.5.3 and *Carpenter and Anderson*, 1992].

A simple shift of 1° in latitude and 0.35 s in time brings the measured onset durations (indicated by two circles marking the beginning and end of onset with

a line drawn between them) in good agreement with those predicted, as shown in Figure 4.9d. Implementing this same 1° shift in latitude places the precipitation region solidly on the NAA–HAIL paths, as shown in Figure 4.9c. The association of the calculated ionospheric disturbance shape with the distribution of perturbed paths is quite remarkable, for example accounting for the fact that the middle NAA–HAIL paths have the largest signal perturbations, and that the lower four NAU paths are not perturbed.

4.4   Quantitative Interpretation of LEP Events

In Sections 4.3.2 and 4.3.3 we showed that the size, shape, location, and onset delay of the precipitation region inferred from measurements on the various HAIL VLF paths are consistent with the predictions of *Lauben et al.* [1999]. In this section we quantitatively interpret the observed VLF signal changes and inferred spatial extent of the precipitation for event B on 18 October 1998 in terms of the absolute magnitude of the time-integrated precipitation flux (fluence).

At the simplest level, we might interpret the observed change in amplitude at the HAIL receivers by assuming that the magnitudes of the VLF amplitude changes were linearly proportional to the product of deposited flux and spatial extent of the disturbed region, or more specifically the integral of the deposited flux along the disturbed region of the great circle path [*Inan and Carpenter*, 1987]. Assuming the precipitation region to have approximately the size and shape as shown in Figure 4.9c, the magnitude of the NAA signal perturbation would then be expected to remain relatively large on the southernmost HAIL paths. However, as seen in Figure 4.7, the amplitude of the NAA–LV signal perturbation is quite small. Such a result could come about if the precipitation region had an abrupt equatorward edge, perhaps due to a decrease in the trapped energetic electron flux below a certain L value. However, the fact that several NAU–HAIL paths lying further south were also perturbed indicates that the precipitation region extends below the NAA–LV path.
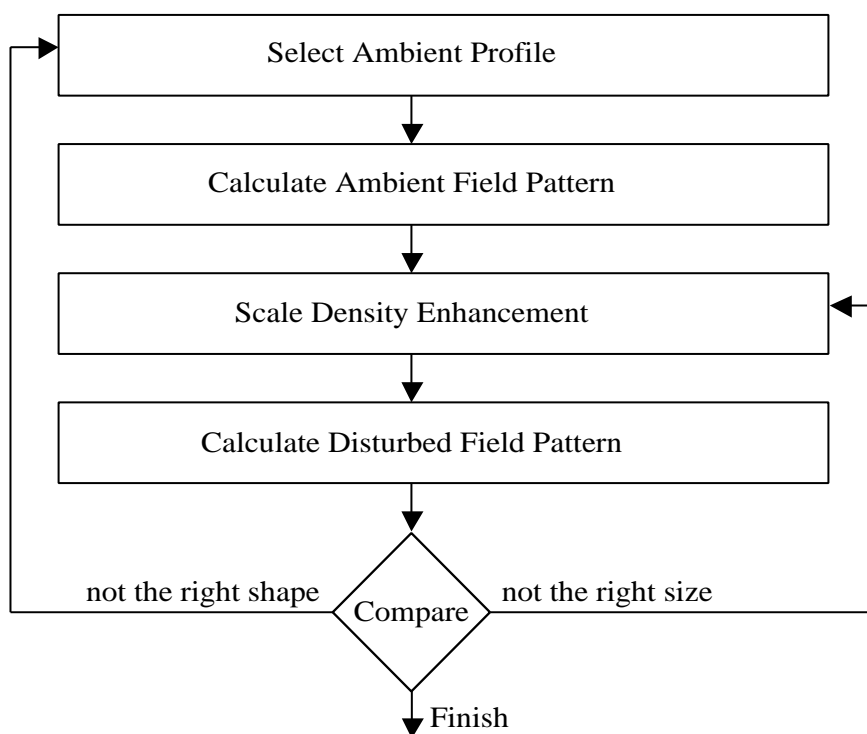
Figure 4.10: Iterative flux determination method. This block diagram illustrates the steps involved in the determination of the magnitude of the precipitating flux, as described in the text.

It is not surprising that the simple *Inan and Carpenter* [1987] interpretation does not provide consistent results in our case, since their method was based on a single waveguide mode model which is particularly applicable for long (>10,000 km) all-sea-based VLF paths. Such an assumption is not appropriate in our case, with various different land-based VLF paths of only several Mm lengths, in which case multiple waveguide mode effects are particularly prevalent.

Figure 4.10 describes a more general quantitative approach was used to interpret the LEP VLF events observed with the HAIL system in the context of the predictions of the *Lauben et al.* [1999] model. Using an assumed initial ambient electron density profile, the LWPC VLF propagation and scattering code (see Section 1.2) was first used to calculate the field amplitude and phase along the NAA–HAIL great circle paths. The precipitation flux calculated by *Lauben et al.* [1999] was used as the input to a Monte Carlo model to determine an ionospheric density enhancement, which

was then added to the ambient ionosphere profile to form a 3D disturbed ionosphere. The LWPC code was then used to calculate the perturbed fields, and the resulting field changes at the HAIL receiver locations were compared with the observations. This process was repeated until a modeled perturbation pattern along the array was obtained which was qualitatively similar to the observed pattern. Finally, in order to take into account the variable parameters summarized in Table 4.1, a multiplicative "scale factor" was applied to the precipitated flux magnitude, and optimized until the magnitude of the modeled perturbation pattern along the array quantitatively matched the observations. This process is described in more detail in the following subsections.

4.4.1   Ionospheric Density Enhancement

The precipitating electron flux and spectra as determined by the oblique whistler-induced precipitation model [*Lauben et al.*, 1999] was used as an input to a recent Monte Carlo simulation model developed by *Lehtinen* [2000], in order to determine the ionization enhancement profile. This general model uses the Langevin equation of motion to describe the momentum of a set of energetic electrons in a collisional gas based upon static electric and magnetic fields, and a stochastic force which describes the scattering. The stochastic force was subdivided into a dynamic friction component, which accounts for collisional excitation and ionization, and an angular diffusion component which imparts random changes in trajectory at each collision. In the event of ionization, the newly created electron was added to the set of scattering electrons. Each electron was followed through successive collisions with neutrals until it had either backscattered out of the simulation region, or until its kinetic energy had decreased below 2 keV.

For the specific case of calculating secondary ionization from this model of energetic electron precipitation, the computation region was defined by 2 km steps in altitude, beginning at 100 km and extending down to ground level. The fair-weather

electric field was taken to be zero because of its negligible influence on electron mo-
tion, and the magnetic field was taken to be vertical. The neutral density profile was
taken from an extension of the Mass Spectrometer Incoherent Scatter (MSISE) model
[*Hedin*, 1991][1]. An initial set of particles was introduced into the simulation with the
energy distribution obtained from *Lauben* [1999]. The initial pitch angle distribution
of the precipitating electrons was assumed to have the shape given by *Inan et al.*
[1989], with the depth of penetration into the loss cone scaled with the assumed wave
field intensity.

At the end of the simulation, a deposited energy enhancement exists at each
altitude from which the secondary electron production rate was calculated directly
by assuming that every deposited 35 eV of energy creates an electron-ion pair [*Rees*,
1963]. The number of additional electrons at each altitude range was normalized by
the ratio of the *Lauben* [1999] precipitating electron count to the number of electrons
used in the Monte Carlo simulation. In order to account for the variability of the
magnetospheric parameters given in Table 4.1, the final electron density enhancement
was obtained by multiplying the normalized enhancement by a scale factor.

The Monte Carlo model was run for the same samples in magnetic latitude and
longitude for which the *Lauben* [1999] two-dimensional precipitation region was origi-
nally calculated. Although the electrons enter at near grazing angles (they have been
scattered into the loss cone by fractions of a degree in equatorial pitch angle), they
are typically scattered within one gyroradius ($\sim$10–40 m) in the horizontal dimen-
sion. Consequently, each 2D ionospheric enhancement was calculated independently.
The resulting 3D ionospheric density enhancement was then interpolated from the
individual 2D enhancement profiles.

Slices of the resulting 3D electron density enhancement are shown at several alti-
tudes from 75 to 95 km in Figure 4.11, revealing that the lower altitude enhancement
regions are lower in latitude than the higher altitude ones. This result is due to
the fact that the energy of gyroresonant electrons increases with decreasing L value

---

[1]http://nssdc.gsfc.nasa.gov/space/model/atmos/msise.html
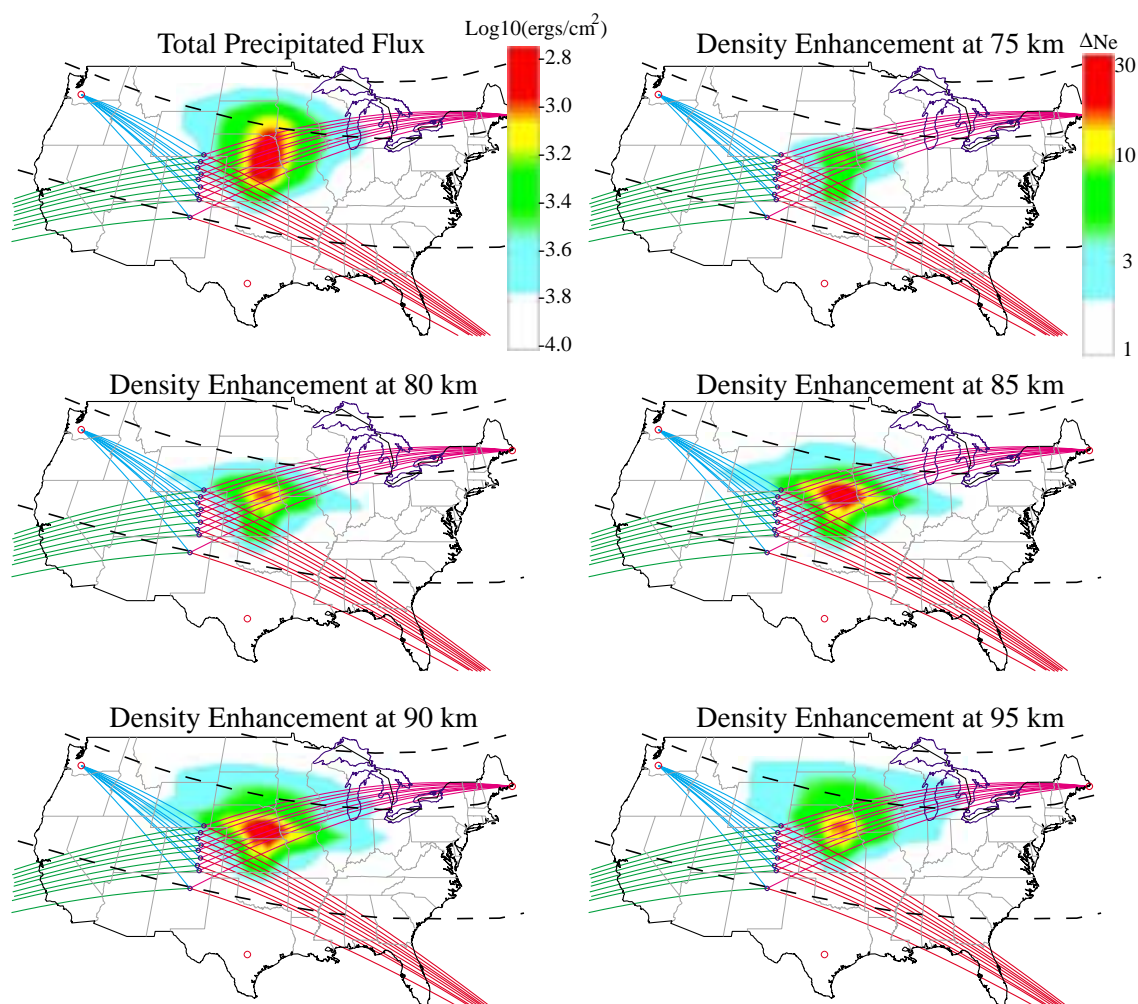
Figure 4.11: Ionospheric density enhancements. The upper left plot shows the total precipitated flux from the *Lauben et al.* [1999] model. A Monte Carlo model was used to generate the 3D ionospheric disturbance, from which several slices are shown. Lower L shells, corresponding to lower latitudes, have higher electron energy populations which penetrate deeper into the ionosphere.

[*Chang and Inan*, 1985]. At lower latitudes, the precipitation flux consists of more of the higher energy electrons, which deposit most of their energy (and hence create secondary ionization) at lower altitudes. The colorscale shown for the density enhancements in Figure 4.11 was selected so that, at the critical reflection altitudes from 80 to 90 km, the minimum enhancement levels displayed extended to the NLK–CH and NLK–FC paths.

Once produced, the secondary electron density enhancement chemically decays

back to ambient levels with an altitude-dependent rate [*Glukhov et al.*, 1992; *Pasko and Inan*, 1994], typically ~10 to ~100 s at the 60–85 km altitudes of interest here.

4.4.2 The Ambient Electron Density Profile

In Chapter 3, a "typical" nighttime ambient ionosphere was used in a 3D VLF propagation and scattering model in order to determine the VLF scattering pattern projected along the HAIL array due to a localized ionospheric disturbance. For that calculation, our goal was to determine the general shape of the scattering pattern, which is largely determined by the lateral shape of the disturbance, and is only weakly dependent on the altitude profile [*Chen et al.*, 1996]. Accordingly, the modeled ambient ionosphere was only constrained so that there were no strong nulls or peaks along the array to distort the projection of the scattered field pattern. However, for the 18 October 1998 case, we allow for the more general case of an arbitrarily shaped electron density profile for which nulls and/or peaks in field strength may exist along the array.

Assuming a homogeneous ionosphere (at least over the region above the VLF paths considered), and as a first order approximation for an all-night or all-day propagation path, both the absolute and the relative amplitudes from a distributed set of VLF receivers can be used to help determine the ambient profile. Accurate knowledge of the receiver calibrations and the transmitter-radiated power enables measurement of the absolute amplitude levels. For any given propagation path, a table of expected field strengths can be generated for a family of ambient profiles, such as *Wait and Spies* [1964] two parameter exponential models (see Section 1.1.1). Such expected field strengths can then be compared with the measured absolute amplitude levels, in order to select the most consistent profile.

However, in order to remove the uncertainty due to the receiver calibrations and transmitter power, the relative amplitude of the perturbations as observed on different signals is used here to bracket the possible ambient profile. A relative calibration for the NAA–HAIL signals was obtained by comparing daytime amplitude levels for a
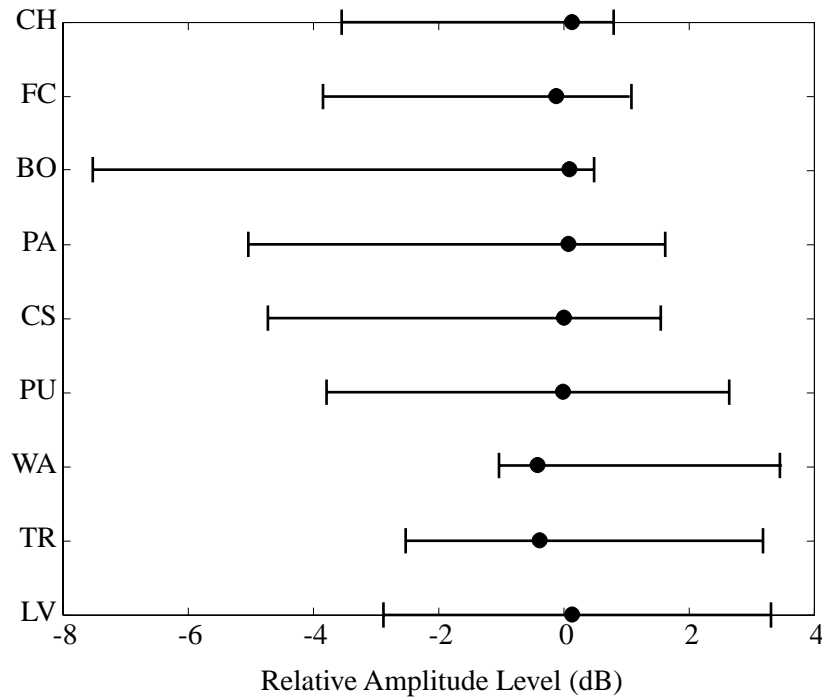
Figure 4.12: Range of ambient received field strengths. The horizontal lines correspond to the range of calibrated ambient received field strengths from 2–10 UT on 18 October 1998 for the NAA–HAIL channels. The black circles are the relative field strengths resulting from the 2D LWPC model using ambient profile 7.5 from Figure 4.13.

thirty day period in the summer of 1998. Although the absolute daytime amplitudes at any one receiver exhibit variations of tens of percent from day-to-day, the ratio of the amplitudes (i.e., their relative variation on any given day) among the receivers were variable within several percent. This ratio was used to calibrate the NAA–HAIL received amplitudes from 02:00–10:00 UT on 18 October 1998, and the corresponding range of amplitudes is shown in Figure 4.12. Only those amplitude profiles which resulted in relative amplitude trends along the array within this range (as determined by 2D LWPC simulation) were considered.

A variety of ambient nighttime D region profiles are shown in Figure 4.13. The International Reference Ionosphere (for this date, time, and location) is shown along with three models (labeled R1, R2, and R3) commonly used in past work [*Lev-Tov et al.*, 1995, and references therein]. The first was based upon a *Wait and Spies* [1964] model (see Section 1.1.1) over the 70 to 95 km altitude range, with a β of .5 and an h'
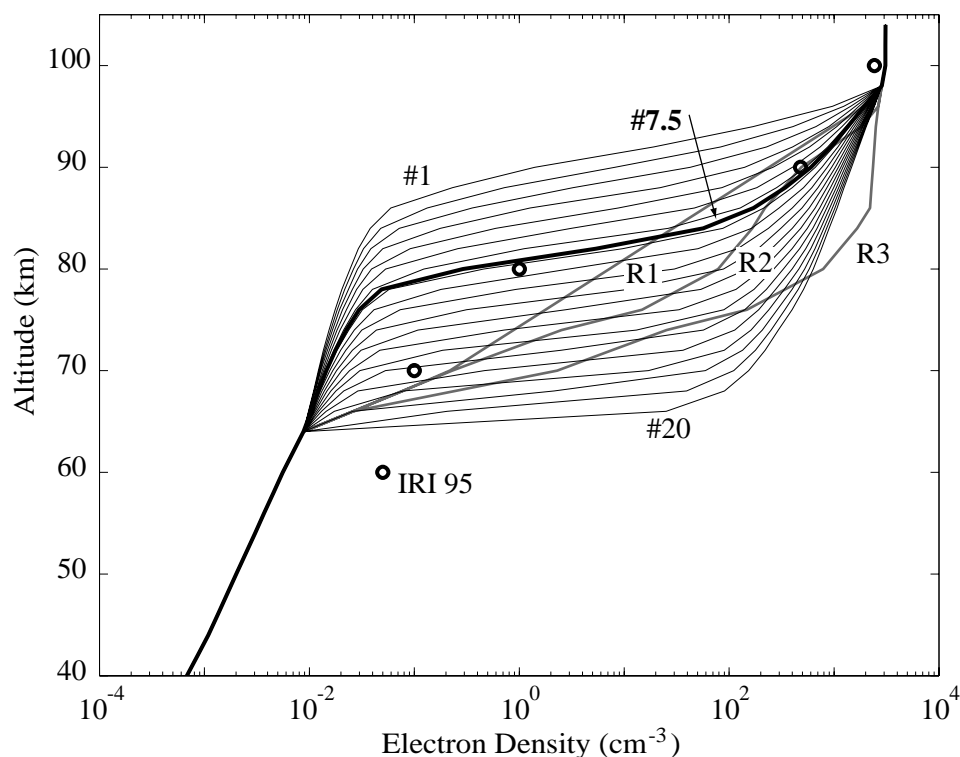
Figure 4.13: Ambient electron density profiles. The black circles correspond to the International Reference Ionosphere (IRI 95) nighttime ambient density profile. The grey lines labeled R1–R3 correspond to three density profiles used in past LEP modeling research [*Rodriguez*, 1994 and references therein]. A family of twenty profiles was heuristically generated to match the disturbance observations for event "B", with the interpolated profile 7.5 resulting in signal perturbations along the HAIL array most similar to those observed.

of 85 km. The second profile was used by *Reagan et al.* [1981] as an enhanced profile for an LEP study, and the third, suggested for disturbed conditions, was adapted from the second by increasing the density by an order of magnitude from 70 to 95 km [*Inan et al.*, 1992]. A family of 20 hybrid profiles (equal to the R1–R3 profiles below 64 km and above 98 km) is also shown. Many such families of hybrid profiles were generated and used in the iterative procedure described (see Figure 4.10) to find a profile which produces signal amplitude changes consistent with the observation.

Rather than relying solely on the modeled amplitude and phase as predicted at the end of the NAA–HAIL paths, two-dimensional color plots were used to view the

signal amplitude all along the path and extending beyond the receivers. As the ambient density profiles become more tenuous, the nulls in signal amplitude (resulting from the multi-mode nature of the signal; see Section 1.2) move away from the transmitter. In Figure 4.14, an example of this effect is shown for ambient profiles 1, 6, 11, and 16 selected from the family of twenty profiles shown in Figure 4.13. In this figure, the amplitude along the NAA–HAIL paths is shown with an arbitrary linear colormap scale for each ambient profile, along with a plot of the ionospheric density perturbation at 80 km. The field strength for the NAA–LV (southernmost) path is additionally plotted on a linear scale, while the ambient density profiles used are shown on the right. For the most tenuous profile (1), the amplitude is relatively smooth along the receivers, and exhibits a null at $\sim$2 Mm from the transmitter. As the ionosphere becomes denser, this particular null moves toward the transmitter, as is evident from the NAA–LV path plot shown at the bottom of the figure. When viewed in this two-dimensional manner, the importance of modeling the multi-mode propagation becomes evident. For example, for profile 6, an amplitude null occurs along the northern HAIL receivers, leading to a complex field strength pattern and a correspondingly complex perturbation signature along the array.
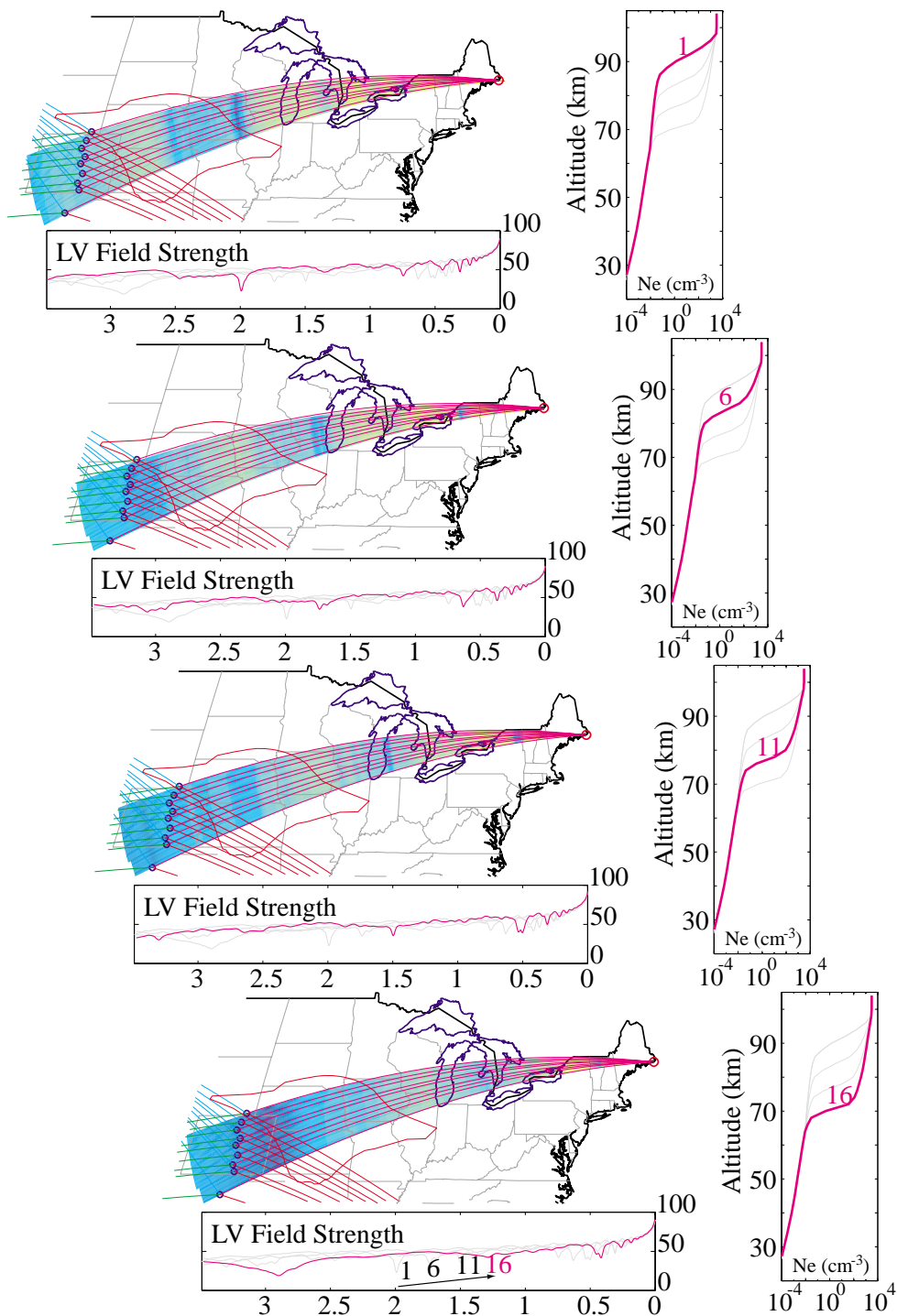
Figure 4.14: The ambient density profile's effect on field strength. Field strength is plotted with a linear colorscale for four electron density profiles. As the profile becomes more dense, the nulls in field strength move towards the transmitter.

4.4.3   Determination of the Precipitated Flux

While the modeled ambient amplitude variation along the array constrain the choice of an ambient ionospheric profile, as described in the previous section, it does not produce a unique solution. Rather, the selection of an ambient ionosphere is made based upon the requirement for the modeled *scattered* field to be qualitatively consistent with the measured amplitude and phase perturbations.

The LEP-produced ionospheric electron density enhancement discussed in Section 4.4.1 is added to an ambient ionosphere to generate a 3D electron density disturbance profile. The 2D LWPC model is then used to calculate the disturbed amplitude and phase along the NAA–HAIL great circle paths. In the calculation of the amplitude and phase for the ambient case, the ionosphere is assumed to be homogeneous along the great circle paths. However, for the case of the ionospheric density enhancement, the path is segmented into eleven equally-spaced paths, and an electron density profile was selected at the center of each segment along the path. Therefore, for the nine HAIL receivers, ninety-nine individual electron density altitude profiles are interpolated from the 3D electron density disturbance profile.

The resulting perturbed field along with the ambient field are used to create 2D maps of the expected event magnitude (in dB) and phase (in degrees). These event maps (as shown in the top panels of Figure 4.16) reveal the expected small perturbations for the portions of the NAA–HAIL great circle paths close to the transmitter (where there was relatively little flux precipitation), and larger perturbations thereafter. The spatial characteristics of these event maps are then used to compare with the event observations. As shown in Figure 4.7, the measured amplitude perturbations are negative, with the largest change of -3.5 dB in the middle of the array. The observed phase perturbations along the array are $\sim 10°$ for those north of CS, and $\sim -5°$ for WA and TR, and are plotted in Figure 4.15.

Most of the ambient profiles tested are not consistent with the amplitude and phase variations of the correct shape, despite the fact that many of them have relative variations in signal strength at the receivers consistent with the observations. For
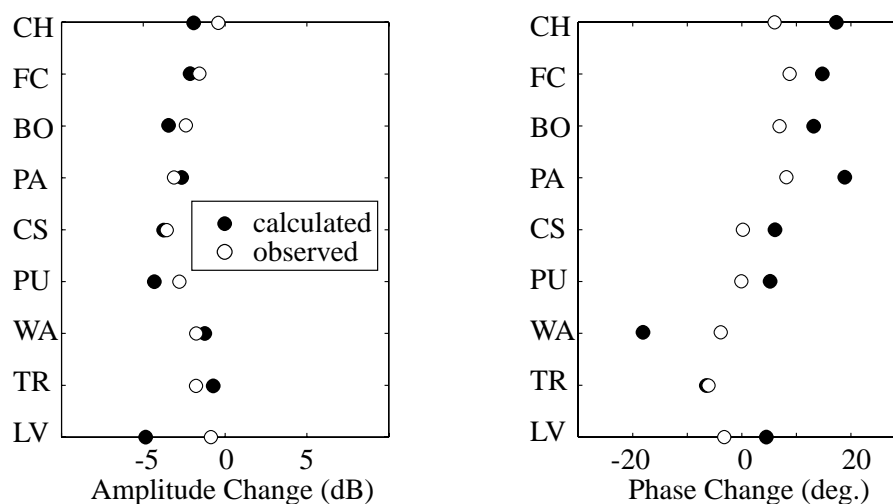
Figure 4.15: Measured and modeled event magnitudes. The observed changes in amplitude and phase are shown along with the modeled changes for profile 7.5.

example, ambient profile 16 from Figure 4.14, with a deep field strength null near the array, produces *positive* amplitude perturbations when the enhancement is added. In general, those ambient profiles for which a null existed near the HAIL receivers are not viable solutions because the change in mode structure due to the disturbance would generally move the null, resulting in positive amplitude perturbations at the HAIL receivers.

The International Reference Ionosphere and the three profiles used in past work (see Figure 4.13) do not result in modeled amplitude and phase changes similar to the observations, nor do any profiles from a variety of families of profiles which are generated and tested. However, among the family of twenty profiles shown in Figure 4.13, both profile 7 and profile 8 produce amplitude and phase perturbations at the HAIL receiver locations which are qualitatively similar to those observed. These two profiles are combined with a linear average, resulting in a profile 7.5. The resulting modeled amplitude and phase events for profile 7.5, with a scale factor of 1.0, are shown along with the measured events in Figure 4.15.

In order to illustrate the sensitivity of the result to the ambient profile selection, the average amplitude error between the measured and calculated VLF event

magnitudes is shown in Figure 4.16 for profiles 1–20 and also for 7.5. Also shown in Figure 4.16 are color plots of the modeled event magnitudes in the vicinity of the HAIL receivers for profiles 6, 7.5, and 9. In the color plots, the magnitudes of the measured amplitude perturbations are represented by the fill color of the circles drawn at the HAIL receiver locations. The color plot for profile 7.5 reveals a region of destructive interference along the array which is consistent with the measured negative amplitude perturbations for the eight northern NAA–HAIL signals. While the NAA–LV modeled amplitude perturbation differs from the measured event by several dB, the 2D view of the event pattern reveals that the LV receiver site is only ∼50 km to the west of an area consistent with the observation. Such an error between the measured and modeled event pattern could reasonably arise from our modeling approximations, such as the assumption of a homogeneous ambient ionospheric profile.

The *Lauben et al.*, [1999] model results include estimates of the total precipitated energy[2] (assuming energetic electron energy thresholds of 0, 100 keV, or 1 MeV) due to a lightning discharge located at magnetic latitudes of either 21°, 30°, 40°, or 50°. The estimate incorporates the net effect of all the competing factors discussed in Section 4.3.1, such as the lightning peak current, ionospheric absorption, and the differential energy spectrum of the magnetospheric electrons. For the case of a discharge source location at ∼40° magnetic latitude, as with our event B, the model results in a total energy precipitation 1.2 MJ, including only those electrons with energies greater than 100 keV (those which are primarily deposited at or above the nighttime VLF reflection height of ∼75 km).

In order to account for the potential variability of the factors listed in Table 4.1, a scale factor is introduced into the calculation of the D region electron density enhancement (discussed in Section 4.4.1). The electron density enhancement is proportional to the deposited time-integrated flux (the fluence), and hence energy, of the precipitation burst. For profile 7.5, the optimal scale factor used to match the observed VLF perturbations for event B is (somewhat coincidentally) equal to 1. Therefore,

---

[2]See Figure 4.9 from *Lauben*, [1999].
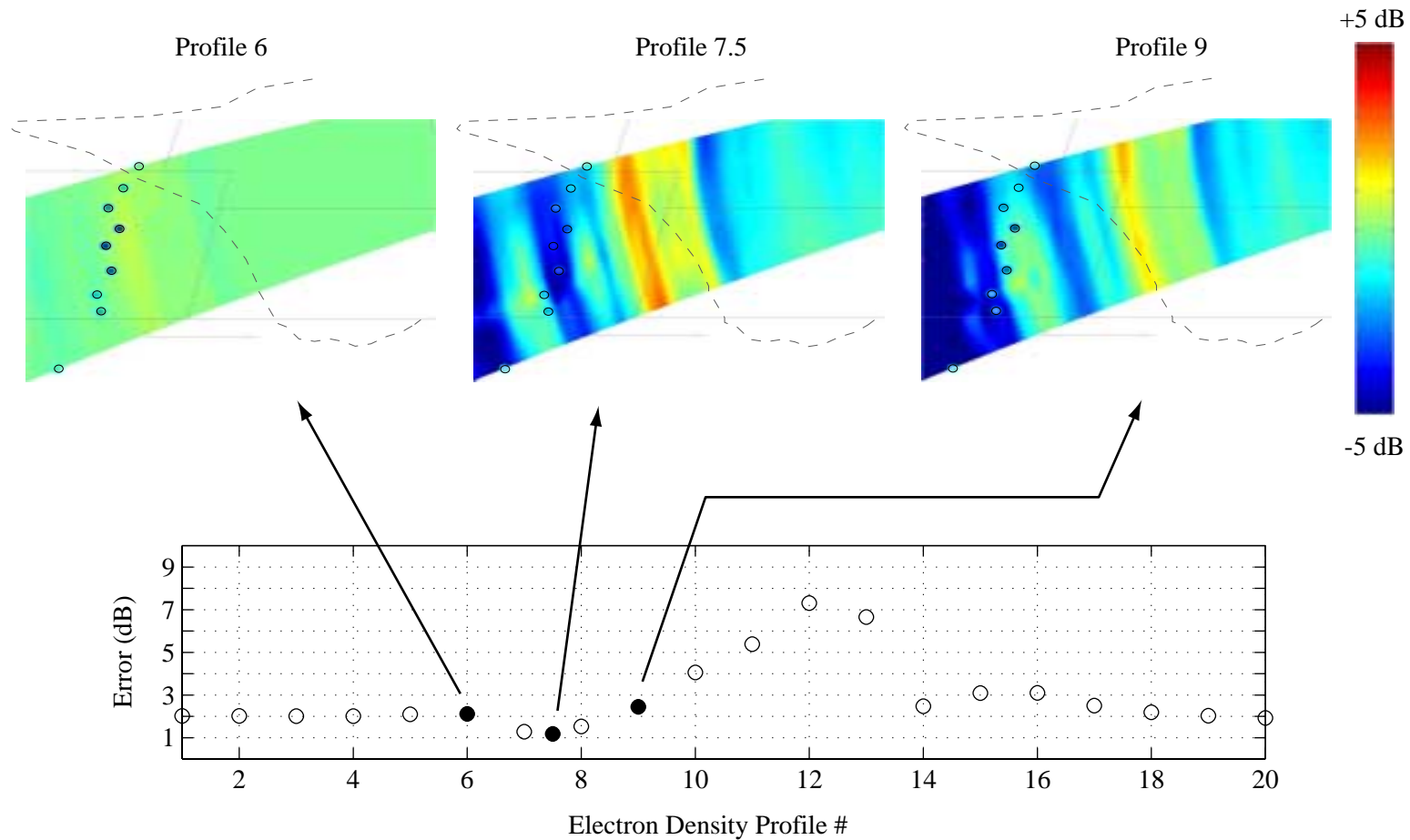
Figure 4.16: Amplitude disturbance map for profiles 6, 7.5, and 9. The bottom panel shows the average error (in dB) between the HAIL recorded amplitude perturbations and the modeled amplitude perturbations. The three colored maps represent the modeled amplitude perturbation along the NAA–HAIL paths. For Profile 6 and 9, the shape of the perturbation does not qualitatively match the observations (i.e., positive amplitude perturbations expected along the array for profile 6). Profile 7.5, however, does qualitatively match the observations in that the model predicts a band of destructive interference along the middle HAIL receivers.

it is our estimate that the predicted 1.2 MJ of energy did indeed precipitate as a result of the associated discharge. However, *Lauben et al.* [1999] assumed a peak current discharge of 33 kA while, in our case, the causative lightning discharge peak current was 15 kA. Therefore, we estimate that our lightning discharge precipitated 2.2 times the precipitation energy than would have been predicted by *Lauben et al.*, [1999] given our 15 kA discharge. This difference is likely due to the fact that one of the factors listed in Table 4.1 was different on 18 October 1998 than the values used by *Lauben et al.*, [1999]. For example, it is quite possible that the quantity of Φ_E, taken to be 10^8 el/cm^2/s/sr/keV at $E = 1$ keV by *Lauben et al.*, [1999], may have been larger, or that the distribution function may fall off in energy slower than the v^{-6} form assumed, allowing for a higher number of particles at the >100 keV energies of interest.

In addition, as our assumption for the ambient profile was limited to the range between profile 7 and profile 8 (recall that profile 6 and 9 model results indicated a qualitatively different perturbation signature across the array), the 30% variability in electron density at 85 km corresponds to a 30% uncertainty for the scale factor.

4.5   LEP VLF Event Occurrence Properties

In this section, we present a case study of the association of LEP VLF events with lightning discharges and document occurrence properties of LEP VLF events based on the analysis of a fifteen-month long data set. The case study is based on data recorded on 4 September 1997, showing that LEP events are correlated with lightning primarily from one of several active lightning storms around the continental United States, and that furthermore only ∼40% of discharges in that storm with peak currents greater than 70 kA are associated with events. The 4 September 1997 case discussed is in fact unusually active, with the enhanced event activity being likely due to the fact that this period was in the recovery stage of a geomagnetic storm, when the magnetospheric energetic electron flux is generally increased. The
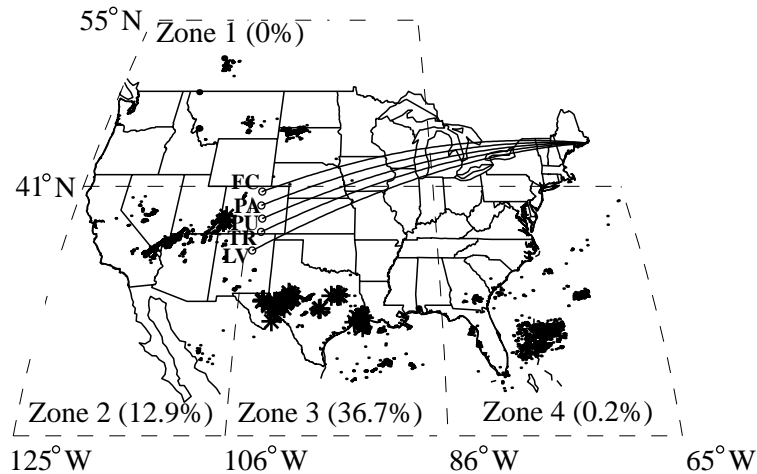
Figure 4.17: 4 September 1997 lightning map. HAIL map with lightning activity displayed from 04:00 to 10:00 UT. The area is divided into four separate zones containing the different storm centers. Lightning from Zone 3 is correlated with all but four of the LEP events observed on the NAA–HAIL paths. The percentages noted are the number of lightning flashes greater than 70kA which are correlated with a VLF event.

subsequently presented comprehensive fifteen-month survey of LEP event occurrence demonstrates that event activity is in fact highly correlated with periods of enhanced geomagnetic activity.

4.5.1   4 September 1997: LEP Association with Lightning

On 4 September 1997 several large thunderstorms occurred around the United States and ~100 well-defined LEP events were observed on the NAA signal between 04:00 and 10:00 UT. The map of the NAA–HAIL great circle paths is shown[3] in Figure 4.17 with the NLDN-recorded cloud-to-ground discharges which occurred during this time period. The storm areas were separated into four different geographic zones, labeled 1–4 in the figure. A half hour period of event activity as measured on the southern three NAA–HAIL signals is shown in Figure 4.18, along with those cloud-to-ground discharges which occurred within 1 s of an event. Nearly every LEP event was associated with a cloud-to-ground discharge, with the causative discharges being both positive and negative in polarity.

---

[3]In 1997, the HAIL array consisted of five observation sites.
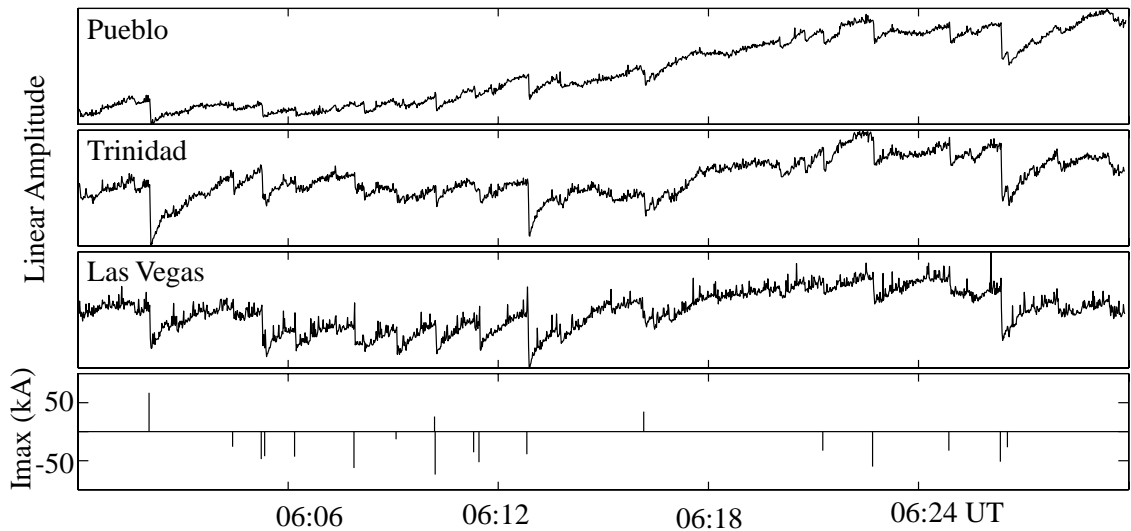
Figure 4.18: 4 September 1997 LEP events. Example LEP events from 4 Spetember 1997 as received by the Southern three HAIL stations from 06:00 to 06:30 UT. NLDN lightning current data is plotted in the bottom panel for those discharges which occur within 1 s of an event.

In Figure 4.17, the fraction of the lightning discharges with peak currents greater than 70 kA that occurred within one second of the onset of one of the hundred selected events is shown for each of the four zones. In Zone 1, none of the discharges greater than 70 kA was associated with events. None of the 100 events was associated with lightning on or nearby (within ± 50 km) the NAA–HAIL propagation paths. In Zone 4, 0.2% of the discharges were associated with an LEP event, but in those seconds discharges were also recorded in Zone 3. In Zone 2, four discharges located in southwest Colorado were associated with LEP events on the NAA–HAIL paths, and represented 12.9% of those greater than 70 kA magnitude. They led to large LEP events on the NLK–FC paths (shown in Figure 1.5), but produced relatively small events of less than 0.5 dB amplitude change on the southern three NAA–HAIL paths. This relatively small amount of precipitation, occurring almost directly to the east of the discharges, is at first thought to be contradictory with the notion of poleward displacement of the precipitating flux as discussed earlier (Section 4.3.2). However, for lightning discharges at this latitude, *Lauben et al.* [1999] in fact predicts less poleward displacement than for lightning occurring at lower latitude (such as the

earlier example from central Texas). At a source latitude of central Colorado, while the model predicts the maximum flux to precipitate some 5° higher in latitude, ∼10% of the maximum flux also precipitates at the same latitude as the discharge.

Of the 100 events, 96 were associated with lightning in Zone 3, with similar poleward displacement as in the case quantitatively interpreted in Section 4.3.2. It is interesting to note that ∼63% of lightning discharges in this area greater than 70 kA did not produce a measurable LEP event. Given that the magnetospheric conditions were favorable to enable measurable precipitation events during this six-hour episode, the variability of the lightning discharge remains as the sole variable factor of the many parameters that affect the precipitated flux which were discussed in Section 4.3.1.

4.5.2   4 September 1997: Variable Onset Delays

While the event onsets (Δt) and durations (t_d) during the 4 September case were not as well defined as those in the 18 October 1998 case, a differential onset delay is visible, and decreased throughout the period of observation. To remove bias from the relatively noisy onset delay time measurement, an algorithm was devised to make this measurement automatically. The events were all first normalized and then passed through a median filter to reduce effects of impulsive (sferic) noise, followed by a low pass filter to minimize fluctuations in the signal amplitude. An arbitrary threshold was chosen, and the time at which the filtered version of the event fell below the threshold was recorded. In our algorithm, we set the arbitrary threshold to be half of the normalized amplitude change (i.e., 50% point), to avoid a false onset. Thus, the time of the onset as identified corresponds to the peak of the LEP burst, rather than its onset. Although the chosen filter parameters still influenced the outcome of the onset delay measurement, they were iteratively set to give estimates similar to ones that would have been found by visual inspection in the case of well defined events.

The resulting onset delay times for eight well defined events spanning a three hour period of time are plotted in Figure 4.19, demonstrating a 100–200 ms increase in time
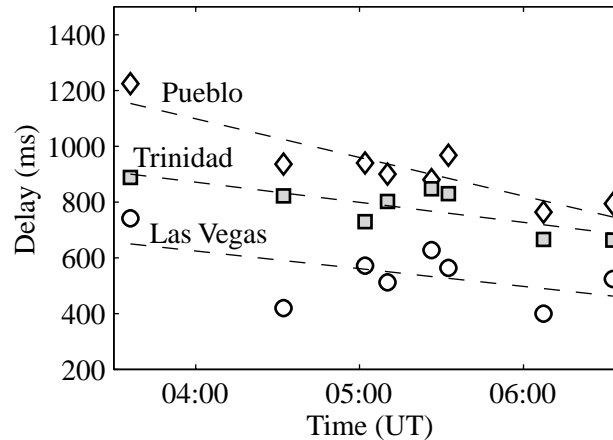
Figure 4.19: 4 September 1997 onset delay decrease. Onset times resulting from the median filter algorithm are shown for eight well defined events. The onset delay times for all three stations appear to increase with latitude as well as decrease with time.

associated with each increase in receiver latitude. The consistent observed difference in delay was initially thought to indicate the presence of three distinct disturbances, possibly corresponding to three magnetospheric ducts, each of which only produces a measurable perturbation on the VLF path to which it is closest. However, in light of the predictions of the oblique precipitation model, continuous onset delay increases due to one large precipitation region are expected, as in the 18 October 1998 case discussed in Sections 4.3 and 4.4. Nevertheless, in this case the onset time delays clearly decrease in time by ∼200 ms over the course of the three hour period. At least some of the magnetospheric parameters discussed in Section 4.3.1 thus appeared to vary with time, possibly due to nighttime drainage of magnetospheric plasma into the decaying ionosphere [e.g. *Tarcsai et al.*, 1988].

This variability may also be related to magnetospheric recovery from a medium-scale geomagnetic storm which had begun several hours before the beginning of the observation period (at ∼19:00 UT on 3 September). At maximum, Kp was 6 and Dst was -90 (see following section), decreasing to ∼3 and ∼ −60 during the event period, respectively. In the following section, we correlate geomagnetic activity with a fifteen-month survey of LEP event activity.

4.5.3   LEP Event Association with Geomagnetic Activity

As discussed in Section 4.3.1, the flux of precipitating electrons in an LEP event is proportional to the trapped magnetospheric flux of energetic particles. In this section, we discuss the occurrence properties of LEP events in relation to geomagnetic activity as measured by geomagnetic indices, and present a fifteen-month comparative survey of LEP event occurrence.

The Kp and Dst indices are both used to keep a record of solar storm activity and its influence on the magnetosphere [*Mayaud*, 1980; pp. 40, 115]. The Kp index, derived from 13 geomagnetic observatories, is designed to measure solar particle flux by its effects on the Earth's magnetic field. The Dst (Disturbance Storm Time) index is constructed by averaging the horizontal component of the geomagnetic field from mid-latitude and equatorial magnetograms, and is sensitive to differential gradient and curvature drifts of electrons and protons in the near-Earth region. The National Geophysical Data Center[4] has a record of these indices since 1957.

To further explore the relationship of oblique LEP VLF events with solar activity, we here use the LEP event occurrence from the fifteen-month automatic event finding survey introduced in Section 3.5. The resulting bar chart of event occurrence is shown in Figure 4.20. The correlation with the quantity of lighting found in early/fast VLF events during the summer of 1998 is clearly not evident for LEP events; few LEP event episodes are observed by HAIL in the summertime. Rather, LEP events appear to be most active during the September through November and the February through April periods, consistent with the previous finding that LEP events have been correlated with the equinoctial cycle [*Carpenter and LaBelle*, 1982]. Groups of LEP events seem to occur in several day episodes, consistent with typical magnetospheric enhancement lifetimes on the order of several days [*Walt*, 1964].

The nine most prominent periods of LEP event activity are labeled A–I in the upper panel of Figure 4.20. While these periods seem to be associated with increased Kp, there are many other periods of elevated Kp which are not. Association with

---

[4]http://ftp.ngdc.noaa.gov/seg/potfld/geomag.shtml
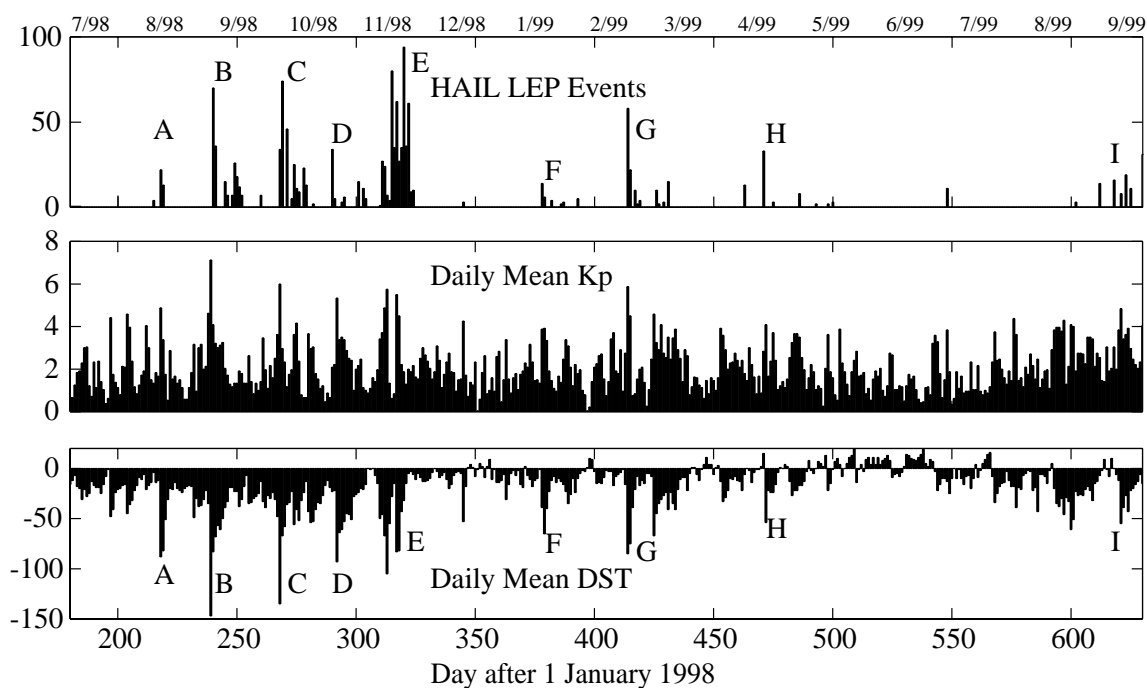
Figure 4.20: LEP VLF event occurrence. From July 1998 to September 1999, LEP VLF events received at the HAIL stations were counted and a histogram of their occurrence is plotted in black in the top panel. Two geomagnetic indices, Kp and Dst, are plotted below for this time period, showing a strong correlation between LEP event activity and geomagnetic disturbances, particularly for the Dst index which is a more appropriate indicator of increased energetic particle populations.

Dst, however, appears to be much more solid. Only the geomagnetic activity peaks following the storm "E" and before "I" are not associated with elevated LEP event activity. These two cases may be due to a variety of factors, most notably the lack of lightning. None of the cases of enhanced LEP activity occurred during a period of quiet Dst.

Carpenter and LaBelle [1982], in a six month survey of LEP event activity as measured at Palmer station, Antarctica, observed dramatic event occurrence rates in September and October of 1978. These periods of event occurrence coincided with the appearance of two major magnetic storms and continued for a number of days following these disturbances. In their paper, they provide a figure detailing the correlation between the Kp index and the event occurrence rate for that period of study.

A subsequent study by *Leyser et al.* [1984] provides data showing a correlation between Kp and LEP event activity at Palmer during the March and April period of 1983. However, in both cases the correlation was far less convincing than it is in Figure 4.20 (neither report provides the Dst index during the observation period, and both covered relatively short durations as compared with the present study). Nevertheless, the more definitive and extensive analysis provided here dictates that LEP event occurrence rates increase following periods of increased geomagnetic activity.

Chapter 5

Summary and Suggestions for Future Research

5.1 Summary and Conclusions

We have presented a set of VLF signatures of lightning-induced ionospheric distur-
bances measured with a unique system of nine VLF receivers known as the Holo-
graphic Array for Ionospheric/Lightning research. Through two years of continuous
operation, data from the HAIL array indicates that lightning discharges routinely
disturb both the distant and overhead ionospheric regions in a complex manner of
ways, both directly and by precipitating bursts of energetic radiation belt particles.

In Chapter 3, several studies of "early/fast" VLF events were presented. These
signal perturbations, so called because they occur immediately after a lightning dis-
charge (<20 ms, i.e., "early") and exhibit a rapid onset (<20 ms, i.e., "fast"), were
previously shown to be associated with ionospheric disturbances located within 50
km of the great circle path of propagation [*Inan et al.*, 1996a, and references therein].
In order to determine the size and shape of individual early/fast disturbances, HAIL
array receivers were deployed with strategic spacing [*Chen et al.*, 1996]. Hundreds
of periods of early/fast event sequences have now been simultaneously observed at
multiple receiver locations. Three typical examples presented in Section 3.1 were
shown to exhibit narrow scattering patterns in the forward direction, having a 15 dB

98

beamwidth with an angular width of $\leq\sim30°$. These event episodes appear to consistently have similar scattering patterns[1]. Two of the typical events were compared with a three-dimensional VLF propagation and scattering code to determine that the ionospheric region within which the conductivity changes occur is 90 ± 30 km across (i.e., about six wavelengths at the 24.0 kHz NAA carrier frequency). A fifteen-month event survey showed the prevalence of early/fast VLF event activity during summer months of intense midwestern thunderstorm activity, during which time 0.43% of all lightning discharges positioned to produce events detectable on the HAIL paths were associated with events.

Our results from Sections 3.3 and 3.4 indicate that ionospheric disturbances that are detected as early/fast VLF events are exclusively produced by lightning episodes which include a large intracloud cluster. This exclusive association was missed in most past work due to the fact that "causative" sferics were observed at locations distant from source discharges and in narrowband channels tuned to VLF transmitter frequencies. Sferic clusters lasting ~1 s and exhibiting properties very similar to those shown here were observed in association with VLF perturbation events in one previous study involving broadband measurements at ~500 km from the active storm center [*Rodriguez et al.*, 1992]. However, in that paper the authors did not recognize the clusters as a property of the causative lightning events and the exclusive nature of their association with early/fast events. This more general result constitutes our first insight into the specific nature of lightning discharges that lead to enhanced electrodynamic coupling between cloud tops and the lower ionosphere.

In Chapter 4, a case study of LEP VLF events and an event occurrence survey were presented. These signal perturbations have been known to differ from early/fast events because they occur with a several hundred millisecond delay and onset duration with respect to a lightning discharge, and are indirectly associated with lightning through a process of magnetopsheric wave-particle interaction and precipitation [*Inan et al.*, 1989, and references therein]. As with the case of early/fast events, the

---

[1]In fact, the author has not yet seen a contradictory case of an early/fast event with a broad scattering pattern in his viewing data from 1998 and 1999.

simultaneous recording of VLF perturbations at the HAIL receivers enabled the determination of the lateral extent of the ionospheric disturbance. LEP VLF events, however, typically disturb an area on the order of a megameter in lateral extent, as evidenced by perturbations of a majority of the HAIL paths. With the HAIL array, these massive regions were found to be activated with a continuum of onset delays and durations, increasing with latitude, and in general poleward-displaced with respect to the causative lightning discharge. In the case from 18 October 1998, with particularly well defined events, the precipitation characteristics inferred from the observed VLF perturbations were shown to be quantitatively consistent with a model of electron precipitation by obliquely propagating (nonducted) whistler waves [*Lauben et al.*, 1999]. The modeled precipitation size, intensity, and spectral content were used to generate a corresponding three dimensional ionospheric enhancement using a recently developed Monte Carlo Model [*Lehtinen*, 2000]. A two-dimensional VLF propagation model was then used to identify an associated ambient and disturbed D region electron density profile, leading to the estimation that a single 15 kA peak current lightning discharge precipitated electrons with a total energy of 1.8 MJ. The variable lightning discharge properties and magnetospheric conditions discussed in Section 4.3.1 lead to considerable variability in the magnitude of the precipitating flux. In a single storm from 4 September 1997, only 40% of lightning discharges with peak currents greater than 70 kA were found to be associated with LEP events, suggesting the importance of other discharge characteristics. The fifteen-month survey of event activity showed that LEP event activity was exclusively associated with elevated levels of solar activity as evidenced by an increase in the geomagnetic Dst index. Our results suggest that the lightning-induced electron precipitation process is likely to be an important contributor to the loss of radiation-belt electrons on a global scale, since oblique whistler waves are naturally excited under all magnetospheric conditions, and fill large regions of the magnetosphere without the need for the presence of field-aligned "ducts" of enhanced ionization.

5.2 Suggestions for Future Research

To date, some ∼100 GB of HAIL data have been recorded. The low resolution data has been archived on the HAIL website. Over the course of this work, those involved in the HAIL program have given more than 50 talks to high school students, and presented several conference papers on educational outreach. The website was developed to be a resource of information about HAIL research, and several high school students have undertaken significant science fair projects under our guidance. Much research remains to be done with the archived data; my first suggestion for future research is that the outreach effort continue and perhaps be a source for original findings by the potential army of enthusiastic young volunteers. Additional suggestions follow.

5.2.1 Expansion of the HAIL Array in the U. S.

The expansion of Internet infrastructure into nearly 100% of the nation's high schools significantly helped facilitate the deployment and operation of the HAIL array. The stations now run autonomously under normal conditions — starting and stopping acquisitions, transferring data to the Stanford server and deleting it after a month, and rebooting when necessary. As system operations continue to become even more robust, additional stations can be added with similar overall maintenance resources.

Example array enhancements are shown in Figure 5.1. Several additional receivers are shown deployed at higher latitudes, extending into central Montana. Data from these locations could be used to investigate the occurrence of oblique precipitation beyond L of 3, as would have been useful in observing the October 18, 1998 event. Precipitation at such high latitudes would be influenced by the location of the plasmapause, which may concentrate wave energy along its inside boundary and lead to especially high precipitation intensities [*Lauben et al.*, 1999].

With the addition of the new VLF transmitter in North Dakota, appropriately located ionospheric disturbances could be imaged from the north by additional receivers oriented longitudinally to an east/west array. With this configuration, an early/fast
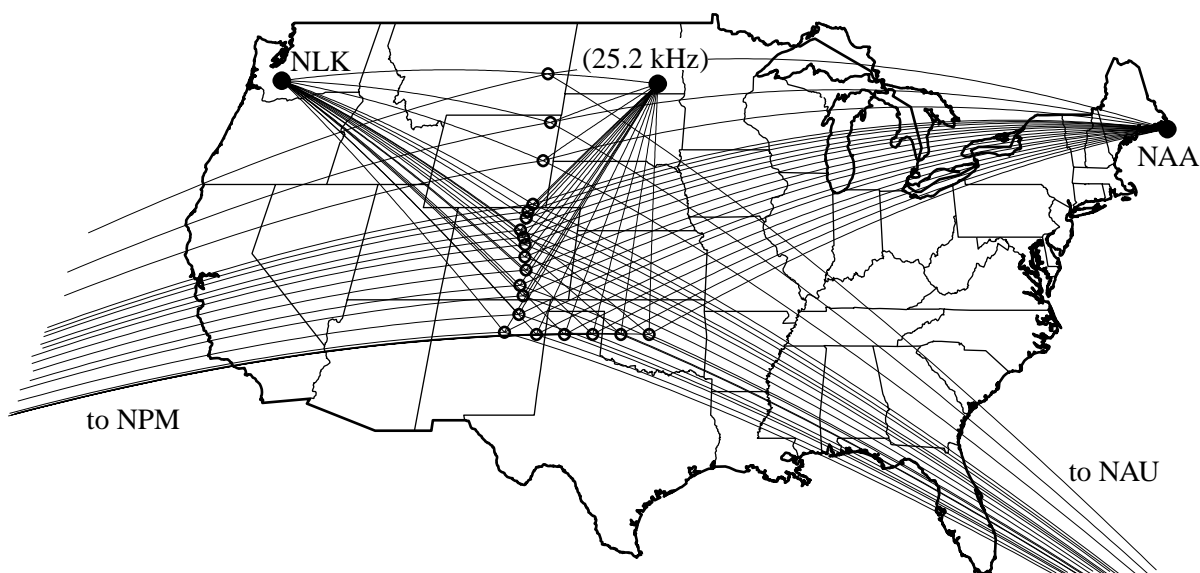
Figure 5.1: Possible HAIL expansion. GCPs are plotted from five VLF transmitters to an expanded version of the current 9 HAIL receivers. The transmitter shown that was not used in this work was recently added at 25.2 kHz in La Moure, North Dakota.

event in the southeast corner of Colorado would be imaged by four directions, allowing future modeling efforts to explore the assumption of rotational symmetry.

By adding receivers interspersed into the current array, two of which are shown below Fort Collins in Figure 5.1, additional information about the lateral variation of early/fast disturbances may be found. While the measurements and modeling technique presented in Chapter 3 clearly pin down the lateral extent of early/fast disturbances as being $\sim$90$\pm$30 km, the assumed Gaussian shape was not varied in this work. Other shapes [*Poulsen et.al*, 1993b] were analytically modeled for the single mode case, each having a characteristic scattering pattern. Because most of the early/fast events were observed only at two or three HAIL receivers, the spatial resolution does not allow us to distinguish between different shapes.

5.2.2   Ambient Ionospheric Profile Estimation

With a more robust calibration at each of the receiver sites, a nightly determination of the ambient ionosphere could be performed with methods similar to those used in

Section 4.4.2. Particularly with the addition of the new VLF transmitter in North Dakota, and the possible expansion of the HAIL array, GCPs to HAIL receivers will cross large portions of the United States. A program could run at Stanford, calculating hourly averages of the received amplitude at all the HAIL sites and from each of the VLF transmitters. If the ionosphere is assumed to be homogeneous over the range of paths, the absolute value of the signal strengths would give an indication of how tenuous the density profile was, and the relative strength at the receivers could further pin down the profile details. This could either be done with an optimization routine iterating two dimensional propagation calculations, such as that used by *Demirkol* [1999], or perhaps also by a table lookup from a matrix of precomputed expected values.

5.2.3   Atmospheric Gravity Wave Studies

Atmospheric gravity waves are generated in the troposphere due to pressure varia- tions in the stratified neutral density. They propagate upward, gaining momentum, until they break in the mesopause region and deposit their energy and momentum [*Garcia and Soloman*, 1985]. This deposited energy at the VLF reflection height disturbs the ambient electron density profile enough to be observed with the VLF technique. An example is shown in Figure 5.2, with clear coherent wave structure evident at the HAIL stations. The amplitude and phase of the received signals can in principle be inverted to yield information about the large scale structure of the waves. Additionally, a simple program could sort through the nightly data to record the spectral structure for possible correlation with tropospheric activity.

5.2.4   Magnetospheric Remote Sensing

As discussed in Section 4.3.1, the energetic particle distribution, $f(v, \alpha)$, contains three variable factors which are individually known with an order of magnitude ap- proximation. Future measurements of $f(v, \alpha)$ by satellite experiments, when co- ordinated with HAIL observed LEP event activity, may be used to eliminate this
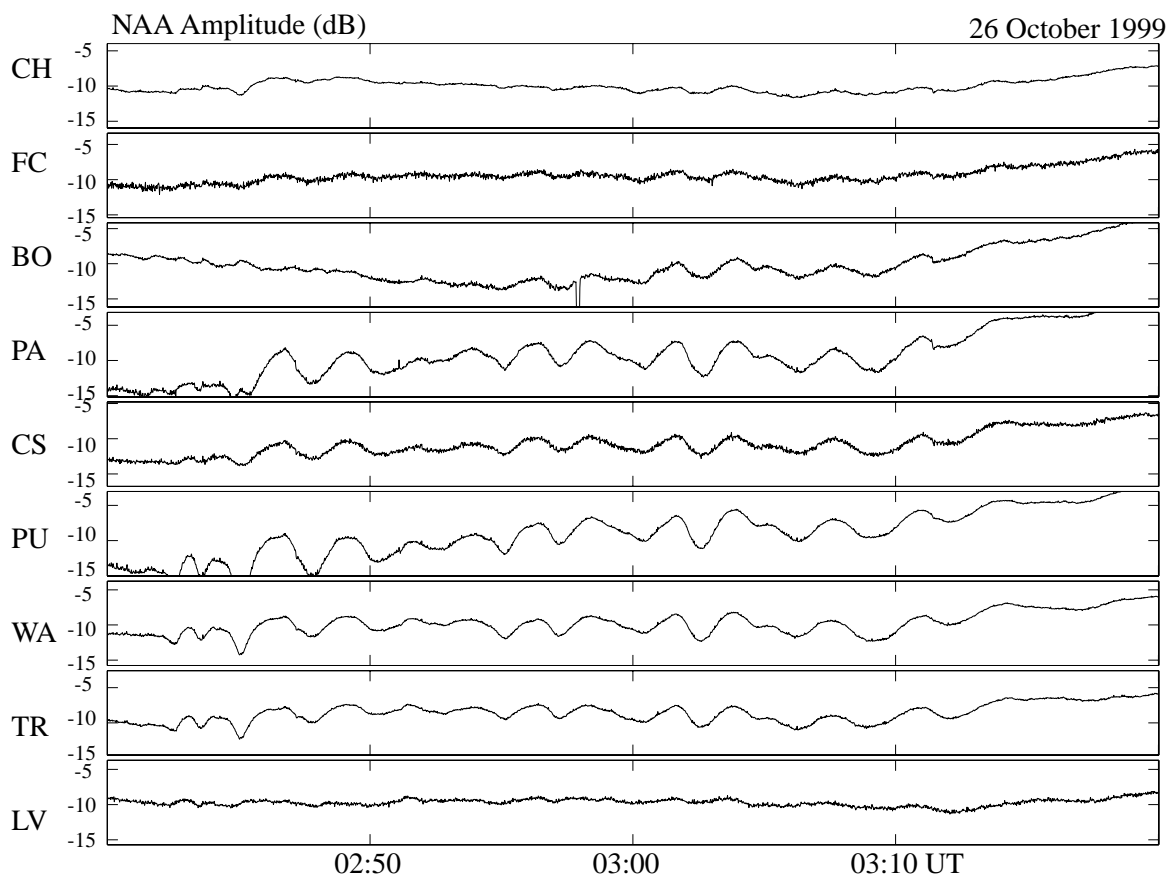
Figure 5.2: Gravity waves observed as HAIL amplitude perturbations.
Atmospheric gravity waves which propagate up to nighttime VLF reflection altitudes are shown here to produce greater than 5 dB changes in received amplitude.

uncertainty. In addition, more detailed examination of particular causative lightning discharges should be possible, for example to determine their spatial and spectral distribution. With a number of these uncertainties known, LEP events may be used in the future as a reliable proxy for certain magnetospheric and global lightning conditions.

5.2.5 Global Deployment

Highly integrated computer systems now exist with enough processesing capability to do the real time amplitude and phase demodulation with only a few watts of power consumption. Such a small and highly mobile system could be deployed in a remote

area and battery powered for months. In some more populated areas, wireless internet connections could be integrated for daily transfer of data back to Stanford (at least for the low resolution data, while high resolution data could be archived locally). Such systems would have to incorporate a smaller version of the current A/D card and the GPS receiver, but these changes may significantly lower the digital receiver cost. These small portable units could be deployed in a low noise location, and eliminate the need for the preamplifier and line receiver.

With such low cost portable units, a large number could be deployed in a short time. Such systems could be used and reused for campaigns to study related ionospheric effects in other regions of the globe. For example, equatorial regions have the most lightning on the planet, yet it it not known if this lightning causes early/fast direct coupling disturbances with the same 0.43% United States occurrence rate discussed in Chapter 3.

Bibliography

[*Angerami and Thomas*, 1964] Angerami, J. J., and J. O. Thomas, Studies of planetary atmospheres 1. The distribution of electrons and ions in the Earth's exosphere, *Journal of Geophysical Research*, 69, 4537, 1964.

[*Angerami*, 1970] Angerami, J. J., Whistler duct properties deduced from VLF observations made with the Ogo 3 satellite near the magnetic equator, *Journal of Geophysical Research*, 75, 6115-6135, 1970.

[*Armstrong*, 1983] Armstrong, W. C., Recent advances from studies of the Trimpi effect, *Antarctic Journal*, 18, 281, 1983.

[*Arnold and Pierce*, 1964] Arnold, H.R., and E.T. Pierce, Leader and junction processes in the lightning discharge as a source of VLF atmospherics, *Radio Science*, 68D, 1964.

[*Bell et al.*, 1998] Bell, T. F., S. C. Reising, and U. S. Inan, Intense Continuing Currents Following Positive Cloud-to-Ground Lightning Associated with Red Sprites, *Geophysical Research Letters*, 25, 1285, 1998.

[*Banks et al.*, 1974] Banks, P. M., C. R. Chappell, and A. F. Nagy, A new model for the interaction of auroral electrons with the atmosphere: spectral degradation, backscatter, optical emissions, and ionization, *Journal of Geophysical Research*, 79, 1459-1470, 1974.

[*Baumjohann and Treumann*, 1997] Baumjohann W., and R. A. Treumann, *Basic Space Plasma Physics*, Imperial College Press, London, 1997.

[*Bracewell and Straker*, 1949] Bracewell R. N. and T. W. Straker, The study of solar flares by means of very long radio waves, *Mon. Not. R. Astr. Soc.*, 109, 28-45, 1949.

[*Brooks*, 1925] Brooks, C. E. P., The distribution of thunderstorms over the globe, *Geophys. Mem. London, 13*, 147, 1925.

[*Budden*, 1961] Budden, K. G., *The Wave-Guide Mode Theory of Wave Propagation*, London: Logos Press, 1961.

[*Budden*, 1962] Budden, K. G., The influence of the Earth's magnetic field on radio propagation by waveguide modes, *Proceedings of the Royal Society A*, 265, 1962.

[*Budden*, 1985] Budden, K. G., *The Propagation of Radio Waves*, Cambridge: Cambridge University Press, 1985.

[*Burgess and Inan*, 1993] Burgess, W. C., and U. S. Inan, The role of ducted whistlers in the precipitation loss and equilibrium flux of radiation belt electrons, *Journal of Geophysical Research*, 98, 15,643, 1993.

[*Burke et al.*, 1991] Burke, W. J., Early Trimpi events from lightning-induced electric fields in the ionosphere: An alternative explanation, *Journal of Atmospheric and Terrestrial Physics*, 54, 205, 1991.

[*Bruce and Golde*, 1941] Bruce, C. E. R., and R. H. Golde, The lightning discharge, *JIEE*, 88, 487-505, 1941.

[*Carlson*, 1986] Carlson, A. B., *Communication Systems*, McGraw-Hill, New York, 1986.

[*Carpenter*, 1970] Carpenter, D. L.,Whistler evidence of the dynamic behavior of the duskside bulge in the plasmasphere, *Journal of Geophysical Research*, 75, 3837, 1970.

[*Carpenter and LaBelle*, 1982] Carpenter, D. L., and J. W. LaBelle, A study of whistlers correlated with bursts of electron precipitation near L=2, *Journal of Geophysical Research*, 84, 4427, 1982.

[*Carpenter and Anderson*, 1992] Carpenter, D. L., and R. R. Anderson, An ISEE/ whistler model of equatorial electron density in the magnetosphere, *Journal of Geophysical Research*, 97,1097-1108, 1992.

[*Chapman and Cowling*, 1970] Chapman, S., and T. G. and Cowling, *The Mathematical Theory of Non-Uniform Gases*, Third Edition, Cambridge University Press, Cambridge, 1970.

[*Chang and Inan*, 1985] Chang, H. C., and U. S. Inan, Lightning-induced electron precipitation from the magnetosphere, *Journal of Geophysical Research*, 90, 1531, 1985.

[*Chen et al.*, 1996] Chen, J., U. S. Inan, and T. F. Bell, VLF strip holographic imaging of lightning-associated ionospheric disturbances, *Radio Science*, 31, 335-348, 1996.

[*Chilton* 1961] Chilton C. J., VLF phase perturbation associated with meteor shower ionization, *Journal of Geophysical Research*, 66, 379-383, 1961.

[*Christian et al.*, 1996] Christian, H. J., R. J. Blakeslee, D. J. Boccipio, W. L. Boek, D. E. Buechler, K. T. Driscoll, S. J. Goodman, J. M. Hall, W. J. Koshak, D. M. Mach, and M. F. Stewart, Global frequency amd distribution of lightning as observed on the Optical Transient Dectector (OTD), *Preprints, 11th International Conference on Atmospheric Electricity*, ed. J. J. Christian, NASA/CP-1999-209261, Guntersville, AL, 726-729, 1999.

[*Cummer*, 1997] Cummer, S. A., Lightning and ionospheric remote sensing using VLF/ELF radio atmospherics, Doctoral Thesis, Stanford University, Stanford, California, 1997.

[*Cummer and Inan*, 1997] Cummer, S. A. and U. S. Inan. Measurement of charge transfer in sprite-producing lightning using ELF radio atmospherics, *Geophysical Research Letters*, 24, 1731, 1997.

[*Cummer et al.*, 1997] Cummer, S. A., T. F. Bell, U. S. Inan, and D. L. Chenette, VLF remote sensing of high energy auroral particle precipitation, *Journal of Geophysical Research*, v. 102, 7477, 1997.

[*Cummer et al.*, 1998] Cummer, S. A., U. S. Inan, and T. F. Bell, Ionospheric D region remote sensing using VLF radio atmospherics, *Radio Science*, 33, 1781-1792, 1998.

[*Cummer and Stanley*, 1999] Cummer, S. A., and M. Stanley, Submillisecond resolution lightning currents and sprite development: Observations and implications, *Geophysical Research Letters*, 26, 3205-08, 1999.

[*Crary*, 1961] Crary, J. H., The effects of the Earth-ionosphere waveguide on whistlers, Technical Report 9, Radioscience Laboratory, Stanford Electronic Laboratories, Stanford, CA, 1961.

[*Crombie*, 1964] Crombie, D. D., Periodic fading of VLF signals received over long paths during sunrise and sunset, *Radio Science*, 68D, 27, 1964.

[*Davies*, 1990] Davies, K., *Ionospheric Radio*, Peregrinus, London, 1990.

[*Dennis and Pierce*, 1964] Dennis, A. S., and E. T. Pierce, The return stroke of the lightning flash to Earth as a source of VLF atmospherics, *Radio Science*, 68D, 777-794, 1964.

[*Demirkol*, 1999] Demirkol, M. K., VLF Remote Sensing of the ambient and modified lower ionosphere, Doctoral Thesis, Stanford University, Stanford, California, 1999.

[*Doolittle*, 1982] Doolittle, J. H., *Modification of the Ionosphere by VLF Wave-Induced Electron Precipitation*, Stanford University Technical Report E4-21301318, 1982.

[*Dowden and Adams*, 1990] Dowden, R. L., and C. D. D. Adams, Location of lightning-induced electron precipitation from measurement of VLF phase and amplitude perturbations on two frequencies, *Journal of Geophysical Research*, 95, 4135-4145, 1990.

[*Dowden et al.*, 1996a] Dowden, R. L., Comment on "VLF signatures of ionospheric disturbances associated with sprites", *Geophysical Research Letters*, 23, 3421-3422, 1996a.

[*Dowden et al.*, 1996b] Dowden, R. L., J. B. Brundell, C. J. Roger, O. A. Molchanov, W. A. Lyons, and T. Nelson, The structure of red sprites determined by VLF scattering, *IEEE Antennas and Propagation*, 38, 7-15, 1996b.

[*Edgar*, 1976] Edgar, B. C., The upper and lower frequency cutoffs of magnetospherically reflected whistlers, *Journal of Geophysical Research*, 81, 205, 1976.

[*Ferguson and Snyder*, 1980] Ferguson, J. A., and F. P. Snyder, Approximate VLF/LF mode conversion model, *Technical Document 400*, Naval Ocean Systems Center, San Diego, California, 1989.

[*Ferguson and Snyder*, 1987] Ferguson, J. A., and F. P. Snyder, The segmented waveguide program for long wavelength propagation calculations, *Technical Document 1518*, Naval Ocean Systems Center, San Diego, California, 1987.

[*Ferguson et al.*, 1989] Ferguson, J. A., F. P. Snyder, D. G. Morfitt, and C. H. Shellman, Long wave propagation capability and documentation, *Technical Document 1518*, Naval Ocean Systems Center, San Diego, CA, 1989.

[*Garcia and Soloman*, 1985] Garcia, R.R. and S. Solomon, Effect of breaking gravity waves on the dynamics and chemical composition of the mesosphere and lower thermosphere, *Journal of Geophysical Research*, 90, 3850-3868, 1985.

[*Glukhov et al.*, 1992] Glukhov, V. S., V. P. Pasko, and U. S. Inan, Relaxation of transient lower ionospheric disturbances caused by lightning-whistler-induced electron precipitation bursts, *Journal of Geophysical Research*, 97, 971, 1992.

[*Gurnett and Inan*, 1988] Gurnett, D. A., and U. S. Inan, Plasma wave observations with the Dynamics Explorer 1 spacecraft, *Rev. Geophys.*, 26, 285, 1988.

[*Hedin*, 1991] A. E. Hedin, Extension of the MSIS Thermospheric Model into the Middle and Lower Atmosphere, *Journal of Geophysical Research*, 96, 1159, 1991.

[*Helliwell*, 1965] Helliwell, R. A., *Whistlers and Related Ionospheric Phenomena*, Stanford, CA: Stanford University Press, 1965.

[*Helliwell et al.*, 1973] Helliwell, R. A., J. P. Katsufrakis, and M. L. Trimpi, Whistler-induced amplitude perturbation in VLF propagation, *Journal of Geophysical Research*, 78, 4679-4688, 1973.

[*Inan et al.*, 1978] Inan, U. S., T. F. Bell, and Helliwell, R. A., Nonlinear pitch angle scattering of energetic electrons by coherent VLF waves in the magnetosphere, *Journal of Geophysical Research*, 83, 3235-53, 1978.

[*Inan et al.*, 1982] Inan, U. S., T. F. Bell, and H. C. Chang, Particle precipitation induced by short-duration VLF waves in the magnetosphere, *Journal of Geophysical Research*, 87, 6243, 1982.

[*Inan et al.*, 1984] Inan, U. S., H. C. Chang, and R. A. Helliwell, Electron precipitation zones around major ground-based VLF signal sources, *Journal of Geophysical Research*, 89, 2891, 1984.

[*Inan and Carpenter*, 1986] Inan, U. S., and D. L. Carpenter, On the correlation of whistlers and associated subionospheric VLF/LF perturbations, *Journal of Geophysical Research*, 91, 3106-16, 1986.

[*Inan and Carpenter*, 1987] Inan, U. S., and D. L. Carpenter, Lightning-induced electron precipitation events observed at L=2.4 as phase and amplitude perturbations on subionospheric VLF signals, *Journal of Geophysical Research*, 92, 3293, 1987.

[*Inan et al.*, 1989] Inan, U. S., M. Walt, H. D. Voss, and W. L. Imhof, Energy spectra and pitch angle distributions of lightning-induced electron precipitation: Analysis of an event observed on the S81-1 (SEEP) Satellite, *Journal of Geophysical Research*, 94, 1379, 1989.

[*Inan et al.*, 1990] Inan, U. S., F. A. Knifsend, and J. Oh, Subionospheric VLF "imaging" of lightning-induced electron precipitation from the magnetosphere, *Journal of Geophysical Research*, 95, 17,217-17,231, 1990.

[*Inan et al.*, 1991] Inan, U. S., T. F. Bell, and J. V. Rodriguez, Heating and ionization of the lower ionosphere by lightning, *Geophysical Research Letters*, 18, 705, 1991.

[*Inan et al.*, 1992] Inan, U. S., J. V. Rodriguez, S. Lev-Tov, and J. Oh, Subionospheric "imaging" of lightning-induced electron precipitation from the magnetosphere, *Geophysical Research Letters*, 18, 705, 1992.

[*Inan et al.*, 1993] Inan, U. S. and J. V. Rodriguez, VLF signatures of lightning-induced heating and ionization of the nighttime D region, *Geophysical Research Letters*, 20, 2355-2358, 1993.

[*Inan et al.*, 1995] Inan, U. S., T. F. Bell, V. P. Pasko, D. D. Sentman, E. M. Wescott, and W. A. Lyons, VLF signatures of ionospheric disturbances associated with sprites, *Geophysical Research Letters*, 22, 3461-64, 1995.

[*Inan et al.*, 1996a] Inan, U. S., A. Slingeland, and V. P. Pasko, VLF and LF signatures of mesospheric/lower ionospheric response to lightning discharges, *Journal of Geophysical Research*, 101, 5,219-5,238, 1996.

[*Inan et al.*, 1996b] Inan, U. S., V. P. Pasko, and T. F. Bell, Sustained heating of the ionosphere above thunderstorms as evidenced by "early/fast" VLF events, *Geophysical Research Letters*, 23, 1067-1070, 1996.

[*Inan et al.*, 1996c] Inan, U. S., T. F. Bell, and V. P Pasko, Reply, *Geophysical Research Letters*, 23, 3423-3424, 1996.

[*Inan and Inan*, 1999] Inan, U. S. and A. S. Inan, *Engineering Electromagnetics*, Addison Wesley Longman, 1999.

[*Inan et al.*, 1999] Inan, U. S., N. G. Lehtinen, S. J. Lev-Tov, M. P. Johnson, T. F. Bell, and K. Hurley, Ionization of the lower ionosphere by gamma rays from a magnetar: Detection of a low energy (3-10 keV) component, *Geophysical Research Letters*, 26, 3357-3360, 1999.

[*Inan and Inan*, 2000] Inan, U. S. and A. S. Inan, *Electromagnetic Waves*, Prentice Hall, 2000.

[*Jasna et al.*, 1992] Jasna D., U. S. Inan and T. F. Bell, Precipitation of suprathermal (100 keV) electrons by oblique whistler waves, *Geophysical Research Letters*, 19,1639-1642, 1992.

[*Johnson et al.*, 1999a] Johnson, M. P., U. S. Inan, S. J. Lev-Tov, and T. F. Bell, Scattering pattern of lightning-induced ionospheric disturbances associated with early/fast VLF events, *Geophysical Research Letters*, 26, 2363-2366, 1999.

[*Johnson et al.*, 1999b] Johnson, M. P., U. S. Inan and D. S. Lauben, Subionospheric VLF signatures of oblique (nonducted) whistler-induced precipitation, *Geophysical Research Letters*, 26, 3569-3572, 1999.

[*Johnson and Inan*, 2000] Johnson, M. P., and U. S. Inan, Sferic Clusters associated with early/fast VLF events, *Geophysical Research Letters*, 27, 1391-1394, 2000.

[*Jordan and Balmain*, 1968] Jordan, E. C. and K. G. Balmain, *Electromagnetic Waves and Radiating Systems*, 2nd ed., Prentice Hall, New Jersey, 1968.

[*Kaiser*, 1974] Kaiser, J.F., Nonrecursive digital filter design using the I_0-sinh window function, *Proceedings of the 1974 IEEE Symposium for Circuits and Systems*, April 1974, p. 20-23. (conference paper)

[*Kim and Muehldorf*, 1995] J. C. Kim and E. I. Muehldorf, *Naval Shipboard Communication Systems*, Prentice Hall, New Jersey, 1995.

[*Lauben et al.*, 1999] Lauben, D. S., U. S. Inan, and T. F. Bell, Poleward-displaced electron precipitation from lightning-generated oblique whistlers, *Geophysical Research Letters*, 26, 2633-36, 1999.

[*Lehtinen*, 2000] Lehtinen, N. G., Relativistic runaway electrons above thunderstorms, Doctoral Thesis, Stanford University, Stanford, California, 2000.

[*Lev-Tov et al.*, 1995] Lev-Tov, S. J., U. S. Inan, and T. F. Bell, Altitude profiles of localized D-region density disturbances produced in lightning-induced electron precipitation events, *Journal of Geophysical Research*, 100, 375, 1995.

[*Leyser et al.*, 1984] Leyser, T., U. S. Inan, D. L. Carpenter, M. L. Trimpi, Diurnal variation of burst precipitation effects on subionospheric VLF/LF signal propagation near L=2, *Journal of Geophysical Research*, 89, 9139, 1984.

[*Mayaud*, 1980] Mayaud, P.N., Derivation, meaning and use of geomagnetic indices, *Geophysical Monograph 22*, American Geophysical Union, 1980.

[*Morfitt and Shellman*, 1976] Morfitt, D. G., and C. H. Shellman, MODESRCH: An improved computer program for obtaining ELF/VLF/LF mode constants in an Earth-ionosphere waveguide, *Interim Report Number 77T*, Propagation Technology Division, Naval Ocean Systems Center, San Diego, California, 1976.

[*Orville et al.*, 1991] Orville, R.E., Calibration of a magnetic direction finding network using measured triggered lightning return stroke peak currents, *Journal of Geophysical Research*, 96, 17135-17142, 1991.

[*Orville*, 1994] Orville, R.E., Cloud-to-Ground Lightning discharge characteristics in the contiguous United States: 1989-1991, *Journal of Geophysical Research*, 99, 10833-41, 1994.

[*Papert and Ferguson*, 1986] Papert, R. A., and J. A. Ferguson, VLF/LF mode conversion model calculations for air to air transmission in the Earth-ionosphere waveguide, *RadioScience*, 21, 551, 1986.

[*Paschal*, 1988] *The Design of Broad-Band VLF Receivers with Air-Core Loop Antennas*, 2nd ed., Unpublished Stanford University VLF Group Document, 1988.

[*Pasko and Inan*, 1994] Pasko, V. P. and U. S. Inan, Recovery signatures of lightning-associated VLF perturbations as a meassure of the lower ionosphere, *Journal of Geophysical Research*, 99, 523, 1994.

[*Pasko et al.*, 1996] Pasko, V. P., U. S. Inan, and T. F. Bell, Sprites as luminous columns of ionization produced by quasi-electrostatic thundercloud fields, *Geophysical Research Letters*, 23, 649, 1996.

[*Pasko et al.*, 1998] Pasko, V. P., U. S. Inan, and T. F. Bell, Ionospheric effects due to electrostatic thundercloud fields, *Journal of Atmospheric and Solar-Terrestrial Physics*, 60, 863-870, 1998.

[*Poulsen et.al*, 1990] Poulsen, W. L., T. F. Bell, and U. S. Inan, Three-dimensional modeling of subionospheric VLF propagation in the presence of localized D region perturbations associated with lightning, *Journal of Geophysical Research*, 95, 2355, 1990.

[*Poulsen*, 1991] Poulsen, W. L., Modeling of very low frequency wave propagation and scattering within the Earth-ionosphere waveguide in the presence of lower ionospheric disturbances, Doctoral Thesis, Stanford University, Stanford, California, 1991.

[*Poulsen et al.*, 1993a] Poulsen W. L., U. S. Inan, and T. F. Bell A multiple-mode three dimensional model of VLF propagation in the earth-ionosphere waveguide in the presence of locaized *D* region Disturbances, *Journal of Geophysical Research*, 98, 1705-1717, 1993.

[*Poulsen et al.*, 1993b] Poulsen W. L., T. F. Bell and U. S. Inan, The scattering of VLF waves by localized ionospheric disturbances produced by lightning-induced electron precipitation, *Journal of Geophysical Research*, 98, 15,553-15,559, 1993.

[*Rawer et al.*, 1978] Rawer, K., D. Bilitza, and S. Ramakrishnan, Goals and status of the International Reference Ionosphere *Reviews of Geophysical Space Sciences*, 16, 177, 1978.

[*Rees*, 1963] Auroral ionization and excitation by incident energetic electrons, *Planetary Space Science*, 11, 1209-1218, 1963.

[*Reagan et al.*, 1981] Reagan, J. B., R. E. Meyerott, R. C. Gunton, W. L. Imhof, E. E. Gaines, and T. R. Larson, Modeling of the ambient and disturbed ionospheric media pertinent to ELF/VLF propagation, in *Medium, Long, and Very Long Wave Propagation (at Frequencies Less than 3000 kHz)*, edited by J. S. Belrose, pp. 33-1-33-10, AGARD Conference Proceedings No. 305, 1981.

[*Rishbeth and Garriott*, 1969] Rishbeth, H., and O. K. Garriott, *Introduction to Ionospheric Physics*, New York: Academic Press, 1969.

[*Rodriguez et al.*, 1992] Rodriguez, J. V., U. S. Inan, Y. Q. Li, R. H. Holzworth, A. J. Smith, R. E. Orville, and T. J. Rosenburg, A case study of lightning, whistlers, and associated ionospheric effects during a substorm particle injection event, *Journal of Geophysical Research*, 97, 65-75, 1992.

[*Rodriguez and Inan*, 1994] Rodriguez, J. V., and U. S. Inan, Electron density changes in the nighttime *D* region due to heating by very-low-frequency transmitters, *Geophysical Research Letters*, 21, 93-96, 1994.

[*Rodriguez*, 1994] Rodriguez, J. V., Modification of the Earth's ionosphere by very-low-frequency transmitters, Doctoral Thesis, Stanford University, Stanford, California, 1994.

[*Round et al.*, 1925] Round, H. J., J. L. Eckersley, K. Tremellen, and F. C. Lunnon, Report on measurements made on signal strength made a great distances during 1922 and 1923, *I.E.E.E.*, 63, 933.

[*Sampath et al.*, 2000] Sampath H. T., U. S. Inan, and M. P. Johnson, Occurrence properties and recovery signatures of lightning-associated subionospheric VLF perturbations, *Journal of Geophysical Research*, 105, 183-191, 2000.

[*Shafer*, 1994] Shafer, D. C., Spread-spectrum VLF remote sensing of the ionosphere, Doctoral Thesis, Stanford University, Stanford, California, 1994.

[*Shao and Krehbiel*, 1996] Shao, X. M. and P. R. Krehbiel, The spatial and temporal development of intracloud lightning, *Journal of Geophysical Research*, 101, 26641-68, 1996.

[*Schulz and Lanzerotti*, 1974] Schulz, M., Lanzerotti, L. J., *Physics and Chemistry in Space*, Springer-Verlag Berlin Heidelberg, New York, 1974.

[*Snyder* 1968] Snyder, F. P., Effect of magnetic dip-angle and azimuth-angle variations on mode numbering at VLF, *NOSC Technical note NELC TN 1394*, 1968.

[*Tarcsai et al.*, 1988] Tarcsai, G., P. Szemeredy, and L. Hegymegi, Average electron density profiles in the plasmasphere between L=1.4 and 3.2 deduced from whistlers, *Journal of Atmospheric and Terrestrial Physics* 50, 607-11, 1988.

[*Taranenko et al.*, 1993] Taranenko, Y. N., U. S. Inan and T. F. Bell, Interaction with the lower ionosphere of electromagnetic pulses from lightning: Heating, attachment, and ionization, *Geophysical Research Letters*, 20, 1539, 1993.

[*Tascione*, 1994] Tascione, T. F., *Introduction to the Space Environment*, Krieger Publishing Company, Malabar, Florida, 1994.

[*Uman*, 1987] Uman, M. A., *The Lightning Discharge*, International Geophysics Series Vol. 39, Academic Press, Orlando, 1987.

[*Van Allen*, 1983] James A. Van Allen, *Origins of Magnetospheric Physics*, Smithsonian Institution Press, Washington, DC, 1983.

[*Voss et al.*, 1998] Voss, H. D., M. Walt, W. L. Imhof, J. Mobilia, and U. S. Inan, Satellite observations of lightning-induced electron precipitation, *Journal of Geophysical Research*, 103, 11725-44, 1998.

[*Wait*, 1957] Wait, J. R., The attenuation vs. frequency characteristics of VLF waves, *Proceedings of the I.R.E.*, 45, 768-71, 1957.

[*Wait and Spies*, 1964] Wait, J. R., and K. P. Spies, Characteristics of the Earth-ionosphere waveguide for VLF radio waves, *Technical Note 300* , National Bureau of Standards, Boulder, CO, 1964.

[*Wait*, 1968] Wait, J. R., Mode conversion and refraction effects in the Earth-ionosphere waveguide for VLF radio waves, *Journal of Geophysical Research*, 73, 3537, 1968.

[*Walt*, 1964] Walt, M., The effects of atmospheric collisions on geomagnetically trapped electrons, *Journal of Geophysical Research*, 69, 3947, 1964.

[*Walt*, 1994] Walt, M., *Introduction to Geomagnetically Trapped Radiation*, Cambridge University Press, Cambridge, 1994.

[*Walt*, 1996] Walt, M., Source and Loss Processes for Radiation Belt Particles, *Radiation Belts: Models and Standards*, Geophysical Monograph 97, 1-13, 1996.

[*Watt*, 1967] Watt, A. D., *VLF Radio Engineering*, Pergamon Press, London, 1967.

[*Wescott et al.*, 1998] Wescott, E.M., D.D. Sentman, M.J. Heavner, D.L. Hampton, W.A. Lyons, T. Nelson, Observations of columniform sprites, *Journal of atmospheric and solar-terrestrial physics*, 60, 733-740, 1998.

[*Wolf*, 1990] Wolf, T. G., Remote sensing of ionospheric effects using very low frequency radio signals, Doctoral Thesis, Stanford University, Stanford, California, 1990.

[*Zmuda et al.*, 1963] Zmuda, A. J., B. W. Shaw, and C. R. Haave, VLF disturbances caused by the nuclear detonation of October 26, 1962, *Journal of Geophysical Research*, 68, 4105-4114, 1963.